

1

²A SEARCH FOR LONG-LIVED, CHARGED, SUPERSYMMETRIC PARTICLES
³USING IONIZATION WITH THE ATLAS DETECTOR

4

BRADLEY AXEN

5

September 2016 – Version 0.45

6



⁸ Bradley Axen: *A Search for Long-Lived, Charged, Supersymmetric Particles using*
⁹ *Ionization with the ATLAS Detector*, Subtitle, © September 2016

10

Usually a quotation.

11

Dedicated to.

₁₂ ABSTRACT

₁₃ How to write a good abstract:

₁₄ <https://plg.uwaterloo.ca/~migod/research/beck00PSLA.html>

₁₅ PUBLICATIONS

₁₆ Some ideas and figures have appeared previously in the following publications:

₁₇

₁₈ Put your publications from the thesis here. The packages `multibib` or `bibtopic`
₁₉ etc. can be used to handle multiple different bibliographies in your document.

²¹ ACKNOWLEDGEMENTS

²² Put your acknowledgements here.

²³

²⁴ And potentially a second round.

²⁵

26 CONTENTS

27	I	INTRODUCTION	1
28	1	INTRODUCTION	3
29	II	THEORETICAL CONTEXT	5
30	2	STANDARD MODEL	7
31	2.1	Particles	7
32	2.2	Interactions	8
33	2.3	Limitations	8
34	3	SUPERSYMMETRY	9
35	3.1	Motivation	9
36	3.2	Structure	9
37	3.3	Phenomenology	9
38	4	LONG-LIVED PARTICLES	11
39	4.1	Mechanisms	11
40	4.1.1	Examples in Supersymmetry	11
41	4.2	Phenomenology	11
42	4.2.1	Disimilarities to Prompt Decays	11
43	4.2.2	Characteristic Signatures	11
44	III	EXPERIMENTAL STRUCTURE AND RECONSTRUCTION	13
45	5	THE LARGE HADRON COLLIDER	15
46	5.1	Injection Chain	16
47	5.2	Design	17
48	5.2.1	Layout	17
49	5.2.2	Magnets	18
50	5.2.3	RF Cavities	19
51	5.2.4	Beam	21
52	5.3	Luminosity Parameters	21
53	5.4	Delivered Luminosity	23
54	6	THE ATLAS DETECTOR	25
55	6.1	Coordinate System	27
56	6.2	Magnetic Field	28
57	6.3	Inner Detector	30
58	6.3.1	Pixel Detector	33
59	6.3.2	Semiconductor Tracker	35
60	6.3.3	Transition Radiation Tracker	37
61	6.4	Calorimetry	38
62	6.4.1	Electromagnetic Calorimeter	40
63	6.4.2	Hadronic Calorimeters	41
64	6.5	Muon Spectrometer	43
65	6.5.1	Monitored Drift Tube	45

66	6.5.2	Resistive Plate Chamber	46
67	6.5.3	Cathode Strip Chamber	46
68	6.5.4	Thin Gap Chamber	46
69	6.6	Trigger	48
70	7	EVENT RECONSTRUCTION	53
71	7.1	Tracks and Vertices	53
72	7.1.1	Track Reconstruction	53
73	7.1.2	Vertex Reconstruction	53
74	7.2	Jets	53
75	7.2.1	Topological Clustering	53
76	7.2.2	Jet Energy Scale	53
77	7.2.3	Jet Energy Scale Uncertainties	53
78	7.2.4	Jet Energy Resolution	53
79	7.3	Electrons	53
80	7.3.1	Electron Identification	53
81	7.4	Muons	53
82	7.4.1	Muon Identification	53
83	7.5	Missing Transverse Energy	53
84	IV	CALORIMETER RESPONSE	55
85	8	RESPONSE MEASUREMENT WITH SINGLE HADRONS	57
86	8.1	Dataset and Simulation	58
87	8.1.1	Data Samples	58
88	8.1.2	Simulated Samples	58
89	8.1.3	Event Selection	58
90	8.2	Inclusive Hadron Response	59
91	8.2.1	E/p Distribution	59
92	8.2.2	Zero Fraction	60
93	8.2.3	Neutral Background Subtraction	61
94	8.2.4	Corrected Response	63
95	8.2.5	Additional Studies	65
96	8.3	Identified Particle Response	68
97	8.3.1	Decay Reconstruction	68
98	8.3.2	Identified Response	69
99	8.3.3	Additional Species in Simulation	71
100	8.4	Summary	72
101	9	JET ENERGY RESPONSE AND UNCERTAINTY	75
102	9.1	Motivation	75
103	9.2	Uncertainty Estimate	75
104	9.3	Summary	78
105	V	SEARCH FOR LONG-LIVED PARTICLES	81
106	10	LONG-LIVED PARTICLES IN ATLAS	83
107	10.1	Event Topology	83
108	10.1.1	Detector Interactions	84
109	10.1.2	Lifetime Dependence	85
110	10.2	Simulation	88

11	EVENT SELECTION	91
11.1	Trigger	92
11.2	Kinematics and Isolation	93
11.3	Particle Species Rejection	97
11.4	Ionization	100
11.4.1	Mass Estimation	101
11.5	Efficiency	102
12	BACKGROUND ESTIMATION	105
12.1	Background Sources	105
12.2	Prediction Method	106
12.3	Validation	107
12.3.1	Closure in Simulation	107
12.3.2	Validation Region in Data	108
13	SYSTEMATIC UNCERTAINTIES AND RESULTS	111
13.1	Systematic Uncertainties	111
13.1.1	Background Estimate	111
13.1.2	Signal Yield	112
13.2	Final Yields	118
13.3	Cross Sectional Limits	119
13.4	Mass Limits	121
13.5	Context for Long-Lived Searches	123
VI	CONCLUSIONS	127
14	SUMMARY AND OUTLOOK	129
14.1	Summary	129
14.2	Outlook	129
VII	APPENDIX	131
A	INELASTIC CROSS SECTION	133
B	EXPANDED R-HADRON YIELDS AND LIMITS	135
	BIBLIOGRAPHY	141

140 LIST OF FIGURES

141	Figure 1	The particle content of the Standard Model (SM).	8
142	Figure 2	The four collision points and corresponding experiments of the Large Hadron Collider (LHC). The image includes the location of the nearby city of Geneva as well as the border of France and Switzerland.	16
143			
144			
145			
146	Figure 3	The cumulative luminosity over time delivered to the A Toroidal LHC ApparatuS (ATLAS) experiment from high energy proton-proton collisions since 2011. The energies of the collisions are listed for each of the data-taking periods.	17
147			
148			
149			
150			
151	Figure 4	The accelerator complex that builds up to the full design energies at the LHC . The protons are passed in order to Linac 2, the PSB , the PS , the SPS and then the LHC	18
152			
153			
154			
155	Figure 5	A schematic of the layout of the LHC , not to scale. The arched and straight sections are illustrated at the bottom of the schematic, and all four crossing sites are indicated with their respective experiments.	19
156			
157			
158			
159	Figure 6	A cross section of the the cryodipole magnets which bend the flight path of protons around the circumference of the LHC . The diagram includes both the superconducting coils which produce the magnetic field and the structural elements which keep the magnets precisely aligned.	20
160			
161			
162			
163			
164			
165	Figure 7	The arrangement of four radiofrequency (RF) cavities within a cryomodule.	20
166			
167	Figure 8	The cumulative luminosity versus time delivered to ATLAS (green), recorded by ATLAS (yellow), and certified to be good quality data (blue) during stable beams for pp collisions at 13 TeV in 2015.	23
168			
169			
170			
171	Figure 9	The luminosity-weighted distribution of the mean number of interactions per crossing for the 2015 pp collision data at 13 TeV.	24
172			
173			
174	Figure 10	A cut-away schematic of the layout of the ATLAS detector. Each of the major subsystems is indicated.	26
175			
176	Figure 11	A cross-sectional slice of the ATLAS experiment which illustrates how the various SM particles interact with the detector systems.	26
177			
178			
179	Figure 12	The layout of the four superconducting magnets in the ATLAS detector.	29
180			

181	Figure 13	The arrangement of the subdetectors of the ATLAS inner detector. Each of the subdetectors is labelled in the cut-away view of the system.	31
182			
183			
184	Figure 14	A quarter section of the ATLAS inner detector which shows the layout of each of the subdetectors in detail. The lower panel shows an enlarged view of the pixel detector. Example trajectories for a particle with $\eta = 1.0, 1.5, 2.0, 2.5$ are shown. The Insertible B-Layer (IBL), which was added after the original detector commissioning, is not shown.	31
185			
186			
187			
188			
189			
190			
191	Figure 15	A computer generated three-dimensional view of the inner detector along the line of the beam axis. The subdetectors and their positions are labelled.	32
192			
193			
194	Figure 16	An alternative computer generated three-dimensional view of the inner detector transverse to the beam axis. The subdetectors and their positions are labelled.	32
195			
196			
197	Figure 17	The integrated radiation lengths traversed by a straight track at the exit of the ID envelope, including the services and thermal enclosures. The distribution is shown as a function of $ \eta $ and averaged over ϕ . The breakdown indicates the contributions of individual subdetectors, including services in their active volume.	33
198			
199			
200			
201			
202			
203	Figure 18	36
204	Figure 19	An image of the insertion of the IBL into the current pixel detector.	36
205			
206	Figure 20	A three-dimensional computer-generated image of the geometry of the IBL with a view (a) mostly transverse to the beam pipe (b) mostly parallel to the beam pipe.	37
207			
208			
209	Figure 21	An exploded view of the geometry of the silicon microstrip (SCT) double layers in the barrel region.	38
210			
211	Figure 22	39
212	Figure 23	The depth of (a) the electromagnetic barrel calorimeter in radiation lengths and (b) all calorimeters in interaction lengths as a function of pseudorapidity.	40
213			
214			
215	Figure 24	A schematic of the Liquid Argon (LAr) calorimeter in the barrel region, highlighting the accordion structure.	40
216			
217	Figure 25	A schematic of a hadronic tile module which shows the alternating layers of steel and plastic scintillator.	42
218			
219	Figure 26	The segmentation in depth and η of the tile-calorimeter modules in the central (left) and extended (right) barrels.	42
220			
221	Figure 27	A cut-away diagram of the muon systems on ATLAS	43
222	Figure 28	A quarter view of the muon spectrometer which highlights the layout of each of the detecting elements. The BOL, BML, BIL, EOL, EML, and EIL are all Monitored Drift Tube (MDT) elements, where the acronyms encode their positions.	44
223			
224			
225			
226			

227	Figure 29	A schematic of the cross-section of the muon spectrometer in the barrel region.	44
228			
229	Figure 30	A schematic of a single MDT chamber, which shows the multilayers of drift tubes as well as the alignment system.	45
230			
231			
232	Figure 31	A schematic of the Cathode Strip Chamber (CSC) endcap, showing the overlapping arrangement of the eight large and eight small chambers.	47
233			
234			
235	Figure 32	A schematic of the Thin Gap Chamber (TGC) doublet and triplet layers.	47
236			
237	Figure 33	The L1 Trigger rate broken down into the types of triggers as a function of the luminosity block for the 2015 data collection period.	49
238			
239			
240	Figure 34	The HLT Trigger rate broken down into the types of triggers as a function of the luminosity block for the 2015 data collection period.	51
241			
242			
243	Figure 35	An illustration (a) of the E/p variable used throughout this paper. The red energy deposits come from the charged particle targeted for measurement, while the blue energy deposits are from nearby neutral particles and must be subtracted. The same diagram (b) for the neutral-background selection, described in Section 8.2.3.	60
244			
245			
246			
247			
248			
249	Figure 36	The E/p distribution and ratio of simulation to data for isolated tracks with (a) $ \eta < 0.6$ and $1.2 < p/\text{GeV} < 1.8$ and (b) $ \eta < 0.6$ and $2.2 < p/\text{GeV} < 2.8$	60
250			
251			
252	Figure 37	The fraction of tracks as a function (a, b) of momentum, (c, d) of interaction lengths with $E \leq 0$ for tracks with positive (on the left) and negative (on the right) charge.	62
253			
254			
255			
256	Figure 38	$\langle E/p \rangle_{\text{BG}}$ as a function of the track momentum for tracks with (a) $ \eta < 0.6$, (b) $0.6 < \eta < 1.1$, and as a function of the track pseudorapidity for tracks with (c) $1.2 < p/\text{GeV} < 1.8$, (d) $1.8 < p/\text{GeV} < 2.2$	63
257			
258			
259			
260	Figure 39	$\langle E/p \rangle_{\text{COR}}$ as a function of track momentum, for tracks with (a) $ \eta < 0.6$, (b) $0.6 < \eta < 1.1$, (c) $1.8 < \eta < 1.9$, and (d) $1.9 < \eta < 2.3$	64
261			
262			
263	Figure 40	$\langle E/p \rangle_{\text{COR}}$ calculated using LCW-calibrated topological clusters as a function of track momentum for tracks with (a) zero or more associated topological clusters or (b) one or more associated topological clusters.	65
264			
265			
266			
267	Figure 41	Comparison of the $\langle E/p \rangle_{\text{COR}}$ for tracks with (a) less than and (b) greater than 20 hits in the TRT.	66
268			
269	Figure 42	Comparison of the $\langle E/p \rangle_{\text{COR}}$ for (a) positive and (b) negative tracks as a function of track momentum for tracks with $ \eta < 0.6$	66
270			
271			

272	Figure 43	Comparison of the E/p distributions for (a) positive and (b) negative tracks with $0.8 < p/\text{GeV} < 1.2$ and $ \eta < 0.6$, in simulation with the FTFP_BERT and QGSP_BERT physics lists.	67
273			
274			
275			
276	Figure 44	Comparison of the response of the hadronic calorimeter as a function of track momentum (a) at the EM-scale and (b) after the LCW calibration.	67
277			
278			
279	Figure 45	Comparison of the response of the EM calorimeter as a function of track momentum (a) at the EM-scale and (b) with the LCW calibration.	68
280			
281			
282	Figure 46	The reconstructed mass peaks of (a) K_S^0 , (b) Λ , and (c) $\bar{\Lambda}$ candidates.	69
283			
284	Figure 47	The E/p distribution for isolated (a) π^+ , (b) π^- , (c) proton, and (d) anti-proton tracks.	70
285			
286	Figure 48	The fraction of tracks with $E \leq 0$ for identified (a) π^+ and π^- , and (b) proton and anti-proton tracks	70
287			
288	Figure 49	The difference in $\langle E/p \rangle$ between (a) π^+ and π^- (b) p and π^+ , and (c) \bar{p} and π^-	71
289			
290	Figure 50	$\langle E/p \rangle_{\text{COR}}$ as a function of track momentum for (a) π^+ tracks and (b) π^- tracks.	72
291			
292	Figure 51	The ratio of the calorimeter response to single particles of various species to the calorimeter response to π^+ with the physics list FTFP_BERT.	72
293			
294			
295	Figure 52	The spectra of true particles inside anti- k_t , $R = 0.4$ jets with (a) $90 < p_T/\text{GeV} < 100$, (b) $400 < p_T/\text{GeV} < 500$, and (c) $1800 < p_T/\text{GeV} < 2300$	76
296			
297			
298	Figure 53	The jet energy scale (<a>JES) uncertainty contributions, as well as the total <a>JES uncertainty, as a function of jet p_T for (a) $ \eta < 0.6$ and (b) $0.6 < \eta < 1.1$	78
299			
300			
301	Figure 54	The <a>JES correlations as a function of jet p_T and $ \eta $ for jets in the central region of the detector.	79
302			
303	Figure 55	A schematic diagram of an R-Hadron event with a lifetime around 0.01 ns. The diagram includes one charged R-Hadron (solid blue), one neutral R-Hadron (dashed blue), Lightest Supersymmetric Particles (<a>LSPs) (dashed green) and charged hadrons (solid orange). The pixel detector, calorimeters, and muon system are illustrated but not to scale.	85
304			
305			
306			
307			
308			
309			
310	Figure 56	A schematic diagram of an R-Hadron event with a lifetime around 4 ns. The diagram includes one charged R-Hadron (solid blue), one neutral R-Hadron (dashed blue), <a>LSPs (dashed green) and a charged hadron (solid orange). The pixel detector, calorimeters, and muon system are illustrated but not to scale.	86
311			
312			
313			
314			
315			

316	Figure 57	A schematic diagram of an R-Hadron event with a life-time around 5 ns. The diagram includes one charged R-Hadron (solid blue), one neutral R-Hadron (dashed blue), LSPs (dashed green) and charged hadrons (solid orange). The pixel detector, calorimeters, and muon system are illustrated but not to scale.	87
317			
318			
319			
320			
321			
322	Figure 58	A schematic diagram of an R-Hadron event with a life-time around 20 ns. The diagram includes one charged R-Hadron (solid blue), one neutral R-Hadron (dashed blue), LSPs (dashed green) and charged hadrons (solid orange). The pixel detector, calorimeters, and muon system are illustrated but not to scale.	87
323			
324			
325			
326			
327			
328	Figure 59	A schematic diagram of an R-Hadron event with a life-time around 20 ns. The diagram includes one charged R-Hadron (solid blue) and one neutral R-Hadron (dashed blue). The pixel detector, calorimeters, and muon system are illustrated but not to scale.	88
329			
330			
331			
332			
333	Figure 60	The distribution of (a) E_T^{miss} and (b) Calorimeter E_T^{miss} for simulated signal events before the trigger requirement.	92
334			
335			
336	Figure 61	The distribution of E_T^{miss} for data and simulated signal events, after the trigger requirement.	94
337			
338	Figure 62	The trigger efficiency for the HLT_xe70 trigger requirement as a function of (a) E_T^{miss} and (b) Calorimeter E_T^{miss} for simulated signal events.	95
339			
340			
341	Figure 63	The dependence of dE/dx on N_{split} in data after basic track hit requirements have been applied.	96
342			
343	Figure 64	The distribution of dE/dx with various selections applied in data and simulated signal events.	96
344			
345	Figure 65	The distribution of track momentum for data and simulated signal events, after previous selection requirements have been applied.	97
346			
347			
348	Figure 66	The distribution of M_T for data and simulated signal events, after previous selection requirements have been applied.	98
349			
350			
351	Figure 67	The distribution of summed tracked momentum within a cone of $\Delta R < 0.25$ around the candidate track for data and simulated signal events, after previous selection requirements have been applied.	99
352			
353			
354			
355	Figure 68	The normalized, two-dimensional distribution of E/p and f_{EM} for simulated (a) $Z \rightarrow ee$, (b) $Z \rightarrow \tau\tau$, (c) 1200 GeV Stable R-Hadron events, and (d) 1200 GeV, 10 ns R-Hadron events.	100
356			
357			
358			

359	Figure 69	Two-dimensional distribution of dE/dx versus charge signed momentum (qp) for minimum-bias tracks. The fitted distributions of the most probable values for pions, kaons and protons are superimposed.	101
360			
361			
362			
363	Figure 70	The distribution of mass estimated using dE/dx for simulated stable R-Hadrons with masses between 1000 and 1600 GeV.	102
364			
365			
366	Figure 71	The acceptance \times efficiency as a function of R-Hadron (a) mass and (b) lifetime. (a) shows all of the combinations of mass and lifetime considered in this search, and (b) highlights the lifetime dependence for 1000 GeV and 1600 GeV R-Hadrons.	104
367			
368			
369			
370			
371	Figure 72	The distribution of (a) dE/dx and (b) momentum for tracks in data and simulated signal after requiring the event level selection and the track selection on p_T , hits, and N_{split} . Each sub-figure shows the normalized distributions for tracks classified as hadrons, electrons, and muons in data and R-Hadrons in the simulated signal.	106
372			
373			
374			
375			
376			
377			
378	Figure 73	The distribution of $M_{dE/dx}$ (a) before and (b) after the ionization requirement for tracks in simulated W boson decays and for the randomly generated background estimate.	108
379			
380			
381			
382	Figure 74	The distribution of $M_{dE/dx}$ (a) before and (b) after the ionization requirement for tracks in the validation region and for the randomly generated background estimate.	109
383			
384			
385			
386	Figure 75	The trigger efficiency for the HLT_xe70 trigger requirement as a function of Calorimeter E_T^{miss} for simulated data events with a W boson selection. Simulated signal events and simulated W boson events are also included.	114
387			
388			
389			
390			
391	Figure 76	The efficiency of the muon veto for R-hadrons of two different masses, as a function of $\frac{1}{\beta}$ for simulated R-Hadron tracks.	116
392			
393			
394	Figure 77	The average reconstructed MDT β distribution for $Z \rightarrow \mu\mu$ events in which one of the muons is reconstructed as a slow muon, for both data and simulation. A gaussian fit is superimposed.	117
395			
396			
397			
398	Figure 78	The observed mass distribution of events in data and the generated background distribution in (a) the stable and (b) the metastable signal region. A few example simulated signal distributions are superimposed.	118
399			
400			
401			

402	Figure 79	The observed and expected cross section limits as a function of mass for the stable simulated signal. The predicted cross section values for the corresponding signals are included.	121
403			
404			
405			
406	Figure 80	The observed and expected cross section limits as a function of mass for each generated lifetime. The predicted cross section values for the corresponding signals are included.	122
407			
408			
409			
410	Figure 81	The excluded range of masses as a function of gluino lifetime. The expected lower limit (LL), with its experimental $\pm 1\sigma$ band, is given with respect to the nominal theoretical cross-section. The observed 95% LL obtained at $\sqrt{s} = 8$ TeV [63] is also shown for comparison.	124
411			
412			
413			
414			
415	Figure 82	The constraints on the gluino mass as a function of lifetime for a split-supersymmetry model with the gluino R-Hadrons decaying into a gluon or light quarks and a neutralino with mass of 100 GeV. The solid lines indicate the observed limits, while the dashed lines indicate the expected limits. The area below the curves is excluded. The dots represent results for which the particle is assumed to be prompt or stable.	125
416			
417			
418			
419			
420			
421			
422			

423 LIST OF TABLES

424 Table 1	The design parameters of the LHC beam that determines the energy of collisions and the luminosity, for both the injection of protons and at the nominal circulation.	22
425		
426		
427		
428 Table 2	The performance goals for each of the subsystems of the ATLAS detector. The $ \eta $ coverage specifies the range where the subsystem needs to be able to provide measurements with the specified resolution. The resolutions include a p_T or E dependence that is added in quadrature with a p_T/E independent piece.	27
429		
430		
431		
432		
433		
434 Table 3	A summary of the parameters of the inner detector and each of the subdetectors [3].	34
435		
436 Table 4	A summary of the expected performance of the combined inner detector [8]. Included are the reconstruction efficiencies for multiple particle types as well as the momentum and impact parameter (IP) resolution for various momenta.	35
437		
438		
439		
440		
441 Table 5	The trigger menu for the 2015 data collection with $L = 5 \times 10^{33} \text{ cm}^{-2} \text{ s}^{-1}$. Both the L1 and HLT! (HLT!) selection requirements and their trigger rates are shown measured at the specified luminosity are shown. The typical offline selections represent a typical set of offline requirements imposed after the trigger in an analysis.	50
442		
443		
444		
445		
446		
447		
448 Table 6	The dominant sources of corrections and systematic uncertainties in the JES estimation technique, including typical values for the correcting shift (Δ) and the associated uncertainty (σ).	77
449		
450		
451		
452 Table 7	The expected number of events at each level of the selection for metastable 1600 GeV, 10 ns R-Hadrons, along with the number of events observed in data, for 3.2 fb^{-1} . The simulated yields are shown with statistical uncertainties only. The total efficiency \times acceptance is also shown for the signal.	103
453		
454		
455		
456		
457		
458 Table 8	A summary of the sources of systematic uncertainty for the data-driven background in the signal region. If the uncertainty depends on the mass, the maximum values are reported.	111
459		
460		
461		

462	Table 9	A summary of the sources of systematic uncertainty for the simulated signal yield. The uncertainty depends on the mass and lifetime, and the maximum negative and positive values are reported in the table.	113
463			
464			
465			
466	Table 10	Example of the contributing systematic variations to the total systematic for the E_T^{miss} Scale, as measured in a 1200 GeV, Stable R-Hadron signal sample.	115
467			
468			
469	Table 11	The estimated number of background events and the number of observed events in data for the specified selection regions prior to the requirement on mass. The background estimates show statistical and systematic uncertainties.	118
470			
471			
472			
473			
474	Table 12	The left and right extremum of the mass window for each generated mass point with a 10 ns lifetime.	119
475			
476	Table 13	The left and right extremum of the mass window used for each generated stable mass point.	119
477			
478	Table 14	The expected number of signal events, the expected number of background events, and the observed number of events in data with their respective statistical errors within the respective mass window for each generated stable mass point.	120
479			
480			
481			
482			
483	Table 15	The expected number of signal events, the expected number of background events, and the observed number of events in data with their respective statistical errors within the respective mass window for each generated mass point with a lifetime of 10 ns.	120
484			
485			
486			
487			
488	Table 16	The observed and expected 95% CL lower limit on mass for gluino R-Hadrons for each considered lifetime.	123
489			
490	Table 17	The left and right extremum of the mass window for each generated mass point with a 50 ns lifetime.	135
491			
492	Table 18	The left and right extremum of the mass window for each generated mass point with a 30 ns lifetime.	135
493			
494	Table 19	The left and right extremum of the mass window for each generated mass point with a 10 ns lifetime.	136
495			
496	Table 20	The left and right extremum of the mass window used for each generated mass point with a lifetime of 3 ns.	136
497			
498	Table 21	The left and right extremum of the mass window used for each mass point with a lifetime of 1 ns.	136
499			
500	Table 22	The left and right extremum of the mass window for each generated mass point with a lifetime of 0.4 ns.	137
501			
502	Table 23	The left and right extremum of the mass window used for each generated stable mass point.	137
503			

504	Table 24	The expected number of signal events, the expected number of background events, and the observed number of events in data with their respective statistical errors within the respective mass window for each generated mass point with a lifetime of 50 ns.	137
505			
506			
507			
508			
509	Table 25	The expected number of signal events, the expected number of background events, and the observed number of events in data with their respective statistical errors within the respective mass window for each generated mass point with a lifetime of 30 ns.	138
510			
511			
512			
513			
514	Table 26	The expected number of signal events, the expected number of background events, and the observed number of events in data with their respective statistical errors within the respective mass window for each generated mass point with a lifetime of 10 ns.	138
515			
516			
517			
518			
519	Table 27	The expected number of signal events, the expected number of background events, and the observed number of events in data with their respective statistical errors within the respective mass window for each generated mass point with a lifetime of 3 ns.	139
520			
521			
522			
523			
524	Table 28	The expected number of signal events, the expected number of background events, and the observed number of events in data with their respective statistical errors within the respective mass window for each generated mass point with a lifetime of 1 ns.	139
525			
526			
527			
528			
529	Table 29	The expected number of signal events, the expected number of background events, and the observed number of events in data with their respective statistical errors within the respective mass window for each generated mass point with a lifetime of p4 ns.	140
530			
531			
532			
533			
534	Table 30	The expected number of signal events, the expected number of background events, and the observed number of events in data with their respective statistical errors within the respective mass window for each generated stable mass point	140
535			
536			
537			
538			

539 LISTINGS

540 ACRONYMS

- 541 SM Standard Model
542 CERN European Organization for Nuclear Research
543 SUSY Supersymmetry
544 LSP Lightest Supersymmetric Particle
545 LHC Large Hadron Collider
546 ATLAS A Toroidal LHC ApparatuS
547 CMS Compact Muon Solenoid
548 ALICE A Large Ion Collider Experiment
549 LHCb Large Hadron Collider beauty experiment
550 LEP the Large Electron Positron collider
551 PS Proton Synchrotron
552 PSB Proton Synchrotron Booster
553 SPS Super Proton Synchrotron
554 SCT silicon microstrip
555 TRT transition radiation tracker
556 LAr Liquid Argon
557 EM electromagnetic
558 RPC Resistive Plate Chamber
559 TGC Thin Gap Chamber
560 MDT Monitored Drift Tube
561 CSC Cathode Strip Chamber
562 ToT time over threshold
563 RoI Region of Interest
564 LCW local cluster weighted
565 MIP minimally ionizing particle
566 IP impact parameter

- 567 EPJC European Physical Journal C
568 JES jet energy scale
569 LLP Long-Lived Particle
570 CR Control Region
571 NLO next-to-leading order
572 NLL next-to-leading logarithmic
573 PDF parton distribution function
574 ISR initial state radiation
575 RMS root mean square
576 IBL Insertible B-Layer
577 CP Combined Performance
578 MDT Monitored Drift Tube
579 RF radiofrequency

580

PART I

581

INTRODUCTION

582

You can put some informational part preamble text here.

1

583

584 INTRODUCTION

585

PART II

586

THEORETICAL CONTEXT

587

You can put some informational part preamble text here.

2

588

589 STANDARD MODEL

590 The SM of particle physics seeks to explain the symmetries and interactions of
591 all currently discovered fundamental particles. It has been tested by several genera-
592 tions of experiments and has been remarkably successful, no significant de-
593 viations have been found. The SM provides predictions in particle physics for
594 interactions up to the Planck scale (10^{15} - 10^{19} GeV).

595 The theory itself is a quantum field theory grown from an underlying $SU(3) \times$
596 $SU(2) \times U(1)$ that requires the particle content and quantum numbers consist-
597 ent with experimental observations (see Section 2.1). Each postulated symme-
598 try is accompanied by an interaction between particles through gauge invari-
599 ance. These interactions are referred to as the Strong, Weak, and Electromag-
600 netic forces, which are discussed in Section 2.2.

601 Although this model has been very predictive, the theory is incomplete; for
602 example, it is not able to describe gravity or astronomically observed dark matter.
603 These limitations are discussed in more detail in Section 2.3.

604 21 PARTICLES

605 The most familiar matter in the universe is made up of protons, neutrons, and
606 electrons. Protons and neutrons are composite particles, however, and are made
607 up in turn by particles called quarks. Quarks carry both electric charge and color
608 charge, and are bound in color-neutral combinations called baryons. The elec-
609 tron is an example of a lepton, and carries only electric charge. Another type
610 of particle, the neutrino, does not form atomic structures in the same way that
611 quarks and leptons do because it carries no color or electric charge. Collectively,
612 these types of particles are known as fermions, the group of particles with half-
613 integer spin.

614 There are three generations of fermions, although familiar matter is formed
615 predominantly by the first generation. The generations are identical except for
616 their masses, which increase in each generation by convention. In addition, each
617 of these particles is accompanied by an antiparticle, with opposite-sign quantum
618 numbers but the same mass.

619 The fermions comprise what is typically considered matter, but there are
620 additional particles that are mediators of interactions between those fermions.
621 These mediators are known as the gauge bosons, gauge in that their existence
622 is required by gauge invariance (discussed further in Section 2.2) and bosons in
623 that they have integer spin. The boson which mediates the electromagnetic force
624 is the photon, the first boson to be discovered; it has no electric charge, no mass,
625 and a spin of 1. There are three spin-1 mediators of the weak force, the two
626 W bosons and the Z boson. The W bosons have electric charge of ± 1 and a
627 mass of 80.385 ± 0.015 GeV, while the Z boson is neutral and has a mass of

628 91.1876 \pm 0.0021 GeV. The strong force is mediated by eight particles called
 629 gluons, which are massless and electrically neutral but do carry color charge.

630 The final particle present in the SM is the Higgs boson, which was recently
 631 observed for the first time by experiments at CERN in 2012. It is electrically
 632 neutral, has a mass of 125.7 \pm 0.4 GeV, and is the only spin-0 particle yet to be
 633 observed. The Higgs boson is the gauge boson associated with the mechanism
 634 that gives a mass to the W and Z bosons.

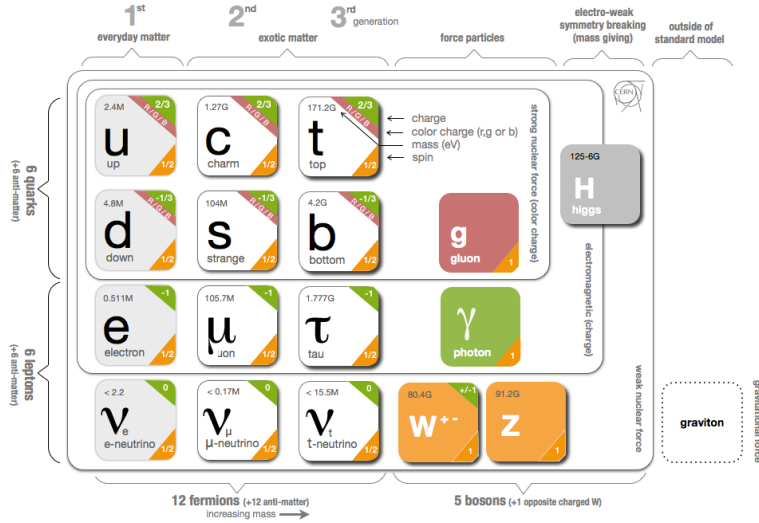


Figure 1: The particle content of the SM.

635 Together these particles form the entire content of the SM, and are summarized
 636 in Figure 1. These are the particles that constitute the observable universe
 637 and all the so-far-observed interactions within it.

638 2.2 INTERACTIONS

639 The interactions predicted and described by the SM are fundamentally tied to the
 640 particles within it, both in that they describe the way those particles can influence
 641 each other and also in that the existence of the interactions requires the existence
 642 of some particles (the gauge bosons).

643 2.3 LIMITATIONS

3

644

645 SUPERSYMMETRY

646 3.1 MOTIVATION

647 3.2 STRUCTURE

648 3.3 PHENOMENOLOGY

4

649

650 LONG-LIVED PARTICLES

651 4.1 MECHANISMS

652 4.1.1 EXAMPLES IN SUPERSYMMETRY

653 4.2 PHENOMENOLOGY

654 4.2.1 DISIMILARITIES TO PROMPT DECAYS

655 4.2.2 CHARACTERISTIC SIGNATURES

656

PART III

657

EXPERIMENTAL STRUCTURE AND RECONSTRUCTION

658

You can put some informational part preamble text here.

659

660 THE LARGE HADRON COLLIDER

661 The LHC, a two-ring superconducting hadron accelerator, provides high energy
662 proton-proton collisions for several large experiments at European Organization
663 for Nuclear Research (CERN) in Geneva, Switzerland [1, 2]. It is the largest,
664 highest-luminosity, and highest-energy proton collider ever built, and was con-
665 structed by a collaboration of more than 10,000 scientists from the more than
666 100 countries that contribute to CERN. The original design of the LHC focused on
667 providing collision energies of up to 14 TeV and generating enough collisions to
668 reveal physics beyond the SM which is predicted to exist at higher energy scales.

669 The LHC was installed in an existing 27 km tunnel at CERN which was origi-
670 nally designed to house the Large Electron Positron collider (LEP). This allows
671 the collider to use existing accelerators at the same complex to provide the initial
672 acceleration of protons up to 450 GeV before injecting into LHC. The injected
673 hadrons are accelerated up to as much as 14 TeV while being focused into two
674 beams traveling in opposite directions. During this process the protons circulate
675 around the tunnel millions of times, while the beams are intermittently crossed
676 at the four locations of the experiments to provide collisions. These collision
677 points correspond to the four major LHC experiments: ATLAS, Compact Muon
678 Solenoid (CMS), Large Hadron Collider beauty experiment (LHCb), and A Large
679 Ion Collider Experiment (ALICE), and Figure 2 shows the layout of the exper-
680 iments both on the surface and below. ATLAS and CMS are both general pur-
681 pose, high-luminosity detectors which search for a wide range of new types of
682 physics [3, 4]. LHCb studies the interactions of b-hadrons to explore the asymme-
683 try between matter and antimatter [5]. ALICE focuses on the collisions of lead
684 ions, which the LHC also provides, in order to study the properties of quark-
685 gluon plasma [6].

686 During the first five years of operation, after the LHC turned on in 2010, the
687 LHC has provided four major data collecting periods. In 2010 the LHC generated
688 collisions at several energies, starting at 900 GeV. It increased the energy from
689 900 GeV to 2.76 TeV and then subsequently to 7 TeV, with a peak luminos-
690 ity of $2 \times 10^{32} \text{ cm}^{-2}\text{s}^{-1}$, and a total delivered luminosity of 50 pb^{-1} . The next
691 run, during 2011, continued the operation at 7 TeV and provided an additional 5
692 fb^{-1} with a peak luminosity of $4 \times 10^{33} \text{ cm}^{-2}\text{s}^{-1}$. The energy was then increased
693 to 8 TeV for the data collection during 2012, which provided 23 fb^{-1} with a peak
694 luminosity of $7.7 \times 10^{33} \text{ cm}^{-2}\text{s}^{-1}$. After the first long shutdown for 2013 and
695 2014, the LHC resumed operation and increased the energy to 13 TeV in 2015,
696 where it delivered 4.2 fb^{-1} with a peak luminosity of $5.5 \times 10^{33} \text{ cm}^{-2}\text{s}^{-1}$. The
697 LHC is currently providing additional 13 TeV collisions in 2016 with higher lu-
698 minosities than during any previous data collection periods. These running peri-
699 ods are summarized in Figure 3, which shows the total delivered luminosity over

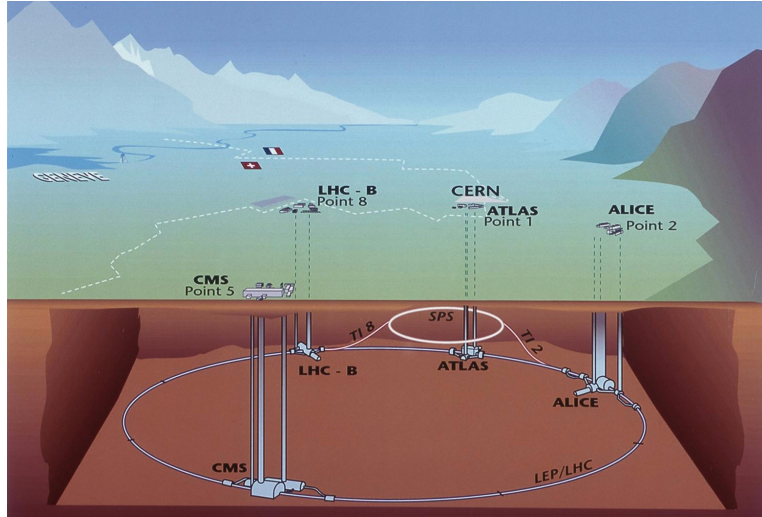


Figure 2: The four collision points and corresponding experiments of the [LHC](#). The image includes the location of the nearby city of Geneva as well as the border of France and Switzerland.

700 time for the [ATLAS](#) experiment during each of the four years of data collection
701 since 2011.

702 5.1 INJECTION CHAIN

703 The [LHC](#) takes advantage of the presence of previously built accelerators at [CERN](#)
704 to work up to the target energy in consecutive stages. The series of accelerators
705 that feed into the [LHC](#) are known collectively as the injection chain, and together
706 with the [LHC](#) form the accelerator complex. The full complex is illustrated in
707 Figure 4, which details the complex series required to reach collisions of 13 or
708 14 TeV.

709 Protons at the [LHC](#) begin as hydrogen atoms in the Linac 2, a linear accelerator
710 which replaced Linac 1 as the primary proton accelerator at CERN in 1978. In
711 Linac 2, the hydrogen atoms are stripped of their electrons by a strong magnetic
712 field, and the resulting protons are accelerated up to 50 MeV by cylindrical con-
713 ductors charged by radio frequency cavities. The protons are then transferred
714 to the Proton Synchrotron Booster ([PSB](#)), which uses a stack of four synchrotron
715 rings to accelerate the protons up to 1.4 GeV. Then the protons are injected
716 into the Proton Synchrotron ([PS](#)) which again uses synchrotron rings to bring
717 the energy up to 25 GeV. The intermediate step between Linac 2 and the [PS](#) is
718 not directly necessary, as the [PS](#) can accelerate protons starting from as low as
719 50 MeV. The inclusion of the [PSB](#) allows the [PS](#) to accept a higher intensity of
720 injection and so increases the deliverable luminosity in the [LHC](#). The penulti-
721 mate stage of acceleration is provided by the Super Proton Synchrotron ([SPS](#)), a
722 large synchrotron with a 7 km circumference that was commissioned at CERN
723 in 1976. During this step the protons increase in energy to 450 GeV, after which
724 they can be directly injected into the [LHC](#).

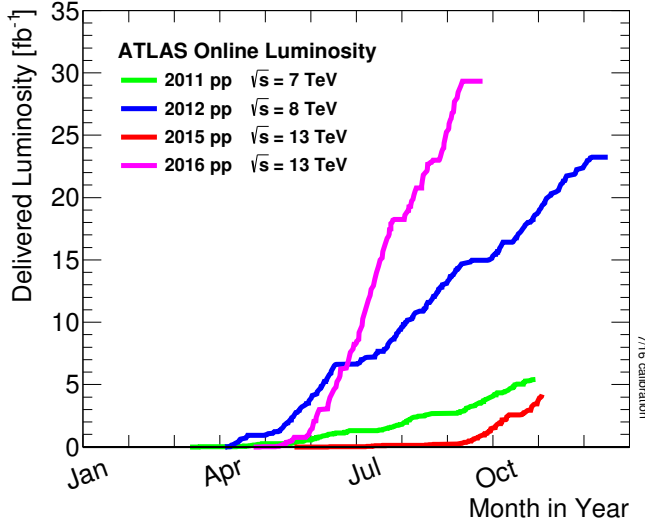


Figure 3: The cumulative luminosity over time delivered to the ATLAS experiment from high energy proton-proton collisions since 2011. The energies of the collisions are listed for each of the data-taking periods.

The final step is the LHC itself, which receives protons from the SPS into two separate beam pipes which circulate in opposite directions. The filling process at this steps takes approximately 4 minutes, and the subsequent acceleration to the final energy (6.5 TeV during 2015 and up to 7 TeV by design) takes approximately half an hour. At this point the protons circulate around the circumference tens of thousands of times a second and continue for up to two hours.

5.2 DESIGN

5.2.1 LAYOUT

Many of the aspects of the LHC design are driven by the use of the existing LEP tunnel. This tunnel slopes gradually, with a 1.4% decline, with 90% of its length built into molasse rock which is particularly well suited to the application. The circumference is composed of eight 2987 meter arcs and eight 528 meter straight sections which connect them; this configuration is illustrated in Figure 5. The tunnel diameter is 3.7 m throughout its length.

The design energy is directly limited by the size of this tunnel, with its radius of curvature of 2804 m. A significant magnetic field is required to curve the protons around that radius of curvature; the relationship is given by

$$p \simeq 0.3BR \quad (1)$$

where p is the momentum of the particle in GeV, B is the magnetic field in Tesla, and R is the radius of curvature in meters. From the target design energy of 14 TeV, or 7 TeV of momentum for protons in each beam, the required magnetic field is 8.33 Tesla. This is too large a field strength to be practical with

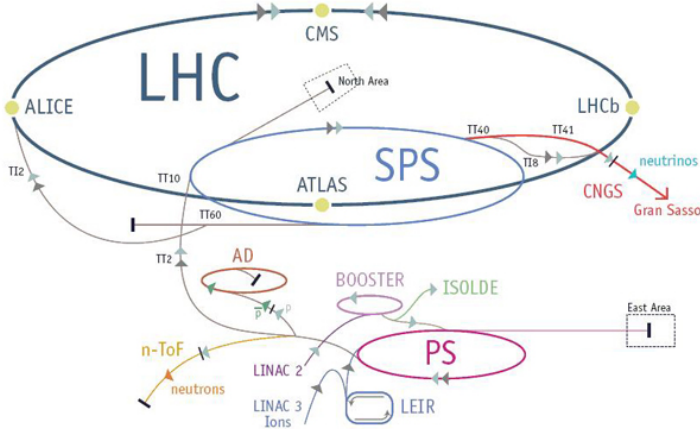


Figure 4: The accelerator complex that builds up to the full design energies at the [LHC](#). The protons are passed in order to Linac 2, the [PSB](#), the [PS](#), the [SPS](#) and then the [LHC](#).

iron electromagnets, because of the enormous power required and the resulting requirements for cooling. Because of these constraints, the [LHC](#) uses superconducting magnets which can maintain that field strength with significantly less power consumption.

5.2.2 MAGNETS

Specifically the magnets chosen were Niobium and Titanium (NbTi) which allow for field strengths as high as 10 Tesla when cooled down to 1.9 K. Reaching the target temperature of 1.9 K for all of the magnets requires superfluid helium and a large cryogenic system along the entire length of the tunnel. During normal operation, the [LHC](#) uses 120 tonnes of helium within the magnets, and the entire system is cooled by eight cryogenic helium refrigerators. The temperature increase that occurs during transit from the refrigerator along the beam necessitates that the refrigerators cool the helium down to 1.8 K. Any significant increase above this temperature range can remove the superconductive properties of the magnets, which in turn generates drastically larger heat losses from the current within the magnets and causes a rapid rise in temperature called a quench.

In all there are approximately 8000 superconducting magnets distributed around the [LHC](#). The 1232 bending magnets, which keep the protons curving along the length of the beam, are twin bore cryodipoles, which allow both proton beams to be accommodated by one magnet and all of the associated cooling structure. Figure 6 shows the cross section of the design for these dipoles. The magnets are very large, 16.5 m long with a diameter of 0.57 meters and a total weight of 28 tonnes. They are slightly curved, with an angle of 5.1 mrad, in order to carefully match the beam path. The twin bore accommodates both magnets inside the two 5 cm diameter holes which are surrounded by the superconducting coils. The coils require 12 kA of current in order to produce the required magnetic

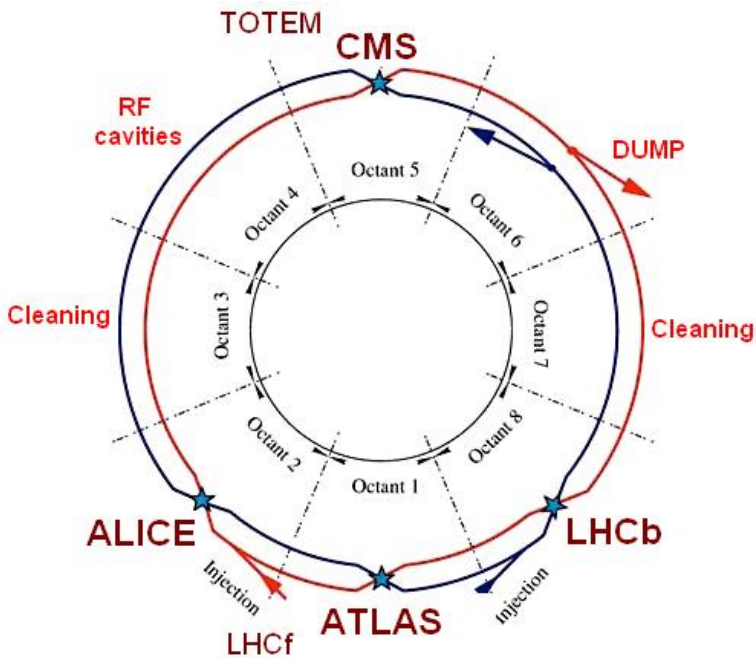


Figure 5: A schematic of the layout of the LHC, not to scale. The arched and straight sections are illustrated at the bottom of the schematic, and all four crossing sites are indicated with their respective experiments.

773 field. These coils are comprised of NbTi cable wound in two layers; the wire in
 774 the inner layer has a diameter of 1.065 mm while the wire in the outer layer has
 775 a diameter of 0.825 mm.

776 The large currents in the wires, along with the magnetic field produced, result
 777 in forces on the magnets which would tend to push them apart with over 10,000
 778 Newtons per meter. Constraining the magnets requires a significant amount of
 779 structure including non-magnetic stainless steel collars. Both the presence of
 780 these electromagnetic forces and the varying thermal contraction coefficient of
 781 the pieces of the magnet produce significant forces on the cold mass structure.
 782 The cold mass is carefully engineered to so that these stresses do not significantly
 783 alter the magnetic field shape, which must be maintained between magnets to a
 784 precision of approximately 10^{-4} for successful operation.

785 The remaining 6800 magnets are a variety of quadrupole, sextapole, octopole,
 786 and single bore dipole magnets. These are used to damp oscillations, correct
 787 beam trajectories, focus the beams during circulation, and to squeeze the beams
 788 before collisions.

789 5.2.3 RF CAVITIES

790 Sixteen RF cavities produce the actual acceleration of the proton beam up to the
 791 design energy. These RF cavities are tuned to operate at 400 MHz, and are pow-
 792 ered by high-powered electron beams modulated at the same frequency, called
 793 klystrons. The resonance within the cavity with the oscillating electric field
 794 establishes a voltage differential of 2 MV per cavity. The sixteen cavities are

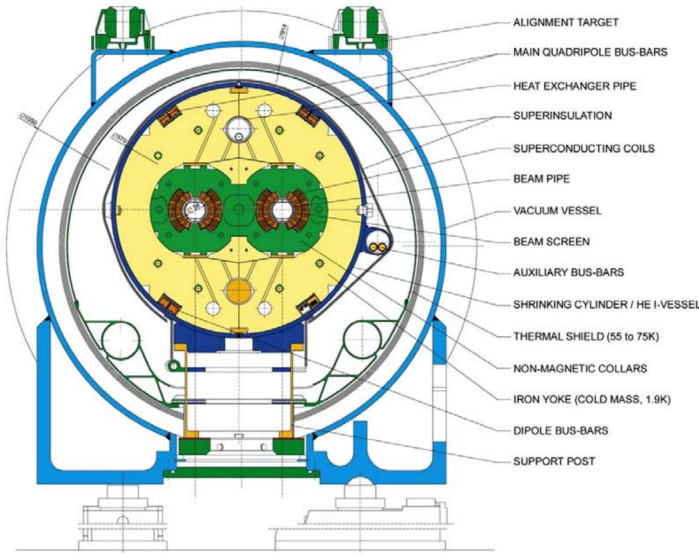


Figure 6: A cross section of the the cryodipole magnets which bend the flight path of protons around the circumference of the LHC. The diagram includes both the superconducting coils which produce the magnetic field and the structural elements which keep the magnets precisely aligned.

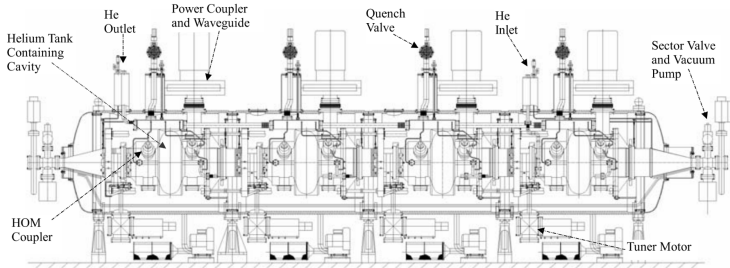


Figure 7: The arrangement of four RF cavities within a cryomodule.

795 split between the two beams, so combined the cavities provide 16 MV per beam,
 796 which accelerate the protons on each consecutive pass through the cavity. This
 797 acceleration is also necessary during circulation even after the target energy has
 798 been reach in order to compensate for losses from synchrotron radiation.

799 The cavities are arranged in cryomodules which contain four cavities, with
 800 two cryomodules per beam; this arrangement is illustrated in Figure 7. These
 801 cryomodules are necessary to maintain the superconducting state of the cavities,
 802 which are also constructed from niobium. The RF cavities use niobium along
 803 with copper to allow for low power losses in the superconductors. The copper
 804 provides a reduced susceptibility to quenching, as it rapidly conducts away heat
 805 generated by imperfections in the niobium, as well as natural shielding from the
 806 earth's magnetic field which can interfere with the RF system.

807 The nature of the radio frequency oscillations tends to group protons together
 808 into buckets. A proton traveling exactly in phase with the RF oscillations will not
 809 be displaced at all during a single circulation, and those slightly ahead or behind

810 of that phase will slightly decelerate or accelerate, respectively. This produces
 811 separate clusters of protons which arrive in phase to the cavities every 2.5 ns,
 812 corresponding to the 400 MHz frequency.

813 5.2.4 BEAM

814 The beams of protons circulate within 54 km of 5 cm diameter beam pipe. This
 815 entire structure is kept under vacuum at 1.9 K to prevent interactions between
 816 the beam pipe and the magnets as well as to prevent any interactions between the
 817 circulating protons and gas in the pipe. The vacuum within the pipe establishes
 818 a pressure as low as 10^{-9} mbar before the protons are introduced.

819 Because of the very high energies of the circulating protons, synchrotron ra-
 820 diation is not negligible in the bending regions. The protons are expected to
 821 radiate 3.9 kW per beam at 14 TeV, with 0.22 W/m, which is enough power to
 822 heat the liquid helium and cause a quench were it absorbed by the magnets. To
 823 prevent this, a copper screen is placed within the vacuum tube that absorb the
 824 emitted photons. This screen is kept between 5 and 20 K by the liquid helium
 825 cooling system.

826 5.3 LUMINOSITY PARAMETERS

827 In addition to the high energy of the collisions, the rate of collisions is extremely
 828 important to enabling the discovery of new physics. Many measurements and
 829 searches require a large number of events in order to be able to make statistically
 830 significant conclusions. The rate of collisions is measured using luminosity, the
 831 number of collisions per unit time and unit cross section for the proton-proton
 832 collisions. From the beam parameters, luminosity is given by

$$833 \quad \mathcal{L} = \frac{N_b^2 n_b f_{rev} \gamma}{4\pi \epsilon_n \beta^*} F \quad (2)$$

833 where N_b is the number of protons per bunch, n_b is the number of bunches per
 834 beam, f_{rev} is the frequency of revolution, γ is the Lorentz factor for the protons
 835 at the circulating energy, ϵ_n is the emittance, β^* is the amplitude function at the
 836 collision point, and F is a geometric factor that accounts for the crossing angle of
 837 the beams at the collision point. The emittance measures the average spread of
 838 particles in both position and momentum space, while the amplitude function
 839 is a beam parameter which measures how much the beam has been squeezed.
 840 Together ϵ_n and β^* give the size of the beam in the transverse direction, $\sigma = \sqrt{\epsilon \beta^*}$. β
 841 changes over the length of the beam as the accessory magnets shape the
 842 distribution of protons, but only the value at the point of collisions, β^* , affects
 843 the luminosity.

844 The luminosity is maximized to the extent possible by tuning the parameters
 845 in Equation 2. A number of these are constrained by the design decisions. The
 846 revolution frequency is determined entirely by the length of the tunnel, as the

Parameter	Unit	Injection	Nominal
Beam Energy	TeV	0.450	7
Peak Instantaneous Luminosity	$\text{cm}^{-2}\text{s}^{-1}$	-	10^{34}
Bunch Spacing	ns	25	25
Number of Filled Bunches	-	2808	2808
Normalized Transverse Emittance	μm	3.75	3.75
Frequency	MHz	400.789	400.790
RF Voltage/Beam	MV	8	16
Stored Energy	MJ	-	362
Magnetic Field	T	0.54	8.33
Operating Temperature	K	1.9	1.9

Table 1: The design parameters of the [LHC](#) beam that determines the energy of collisions and the luminosity, for both the injection of protons and at the nominal circulation.

847 protons travel at very close to the speed of light. The geometric factor F is de-
 848 termined by the crossing angle of the beams at the collision points, again a com-
 849 ponent of the tunnel design; this angle is already very small at $285 \mu\text{rad}$, which
 850 helps to maximize the geometric factor.

851 The major pieces that can be adjusted are the number of protons per bunch,
 852 N_b , the number of bunches in the beam, n_b , and the amplitude function β . In-
 853 creasing either N_b or n_b increases the amount of energy stored in the beam,
 854 which presents a danger if control of the beam is lost. At design specifications,
 855 the beam stores 362 MJ, which is enough energy to damage the detectors or ac-
 856 celerator if the beam were to wander out of the beam pipe. So, the luminosity
 857 is primarily controlled at the [LHC](#) by adjusting β^* , where lowering β^* increases
 858 the luminosity. β^* is tuned to provide the various values of luminosity used at
 859 the [LHC](#) which can be raised to as much as 10^{34} .

860 The nominal bunch structure consists of 3654 bunches, each holding 10^{11} pro-
 861 tons, which cross a collision point in 25 ns. These are further subdivided into the
 862 buckets mentioned in Section 5.2.3 by the clustering properties of the RF cavities.
 863 The bunches are further grouped into trains of 72 bunches which are separated
 864 by a gap which would otherwise hold 12 bunches. At nominal operation 2808
 865 of the bunches will actually be filled with protons, while the remainder are left
 866 empty to form an abort gap that can be used in case the beam needs to be dumped.

867 The various beam parameters are summarized in Table 1 for the designed op-
 868 eration. In practice the beam has operated at lower energies and lower luminosi-
 869 ties than the design values, but the [LHC](#) is expected to operate at the full design
 870 values during Run 2.

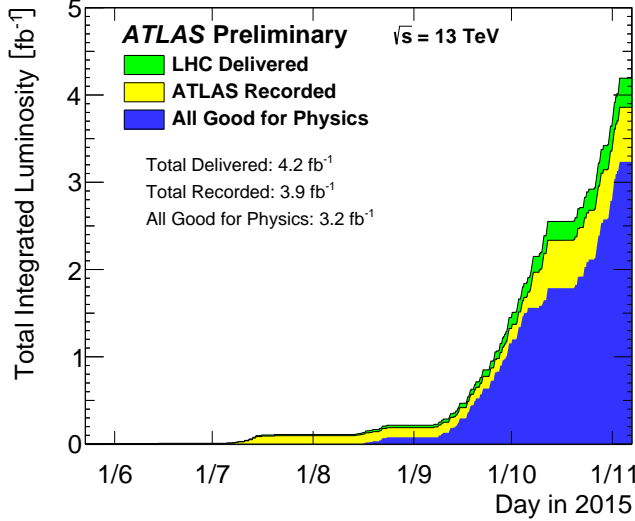


Figure 8: The cumulative luminosity versus time delivered to ATLAS (green), recorded by ATLAS (yellow), and certified to be good quality data (blue) during stable beams for pp collisions at 13 TeV in 2015.

5.4 DELIVERED LUMINOSITY

During the data collection of 2015, the [LHC](#) operated at luminosities as large as 5×10^{33} . It is convenient to refer to the integrated luminosity, the integral of the instantaneous luminosity, which corresponds directly to the number of delivered events for a given process.

$$N = \sigma \times \int \mathcal{L}(t) dt$$

where σ is the cross section for the process of interest. The integrated luminosity over time is shown in Figure 8. This includes the luminosity delivered by the [LHC](#) as well as the luminosity that was recorded by [ATLAS](#). Some of the delivered luminosity is not recorded because [ATLAS](#) is placed in standby until the [LHC](#) reports that the beam conditions are stable, and only then does [ATLAS](#) begin recording. The figure also includes the amount of luminosity marked as good for physics, which includes additional requirements on the operation of the detector during data collection that are necessary for precise measurements.

In addition to the instantaneous luminosity, the beam conditions also influence the number of collisions that occur within a single bunch crossing. The multiple interactions at each crossing are referred to as pileup, often denoted μ , and each of these interactions are present in a single measured event. Figure 9 shows the luminosity-weighted distribution of the mean number of interactions for events collected in 2015. The presence of as many as 20 events in a single collision provides a significant challenge in reconstructing events and isolating the targeted physical processes.

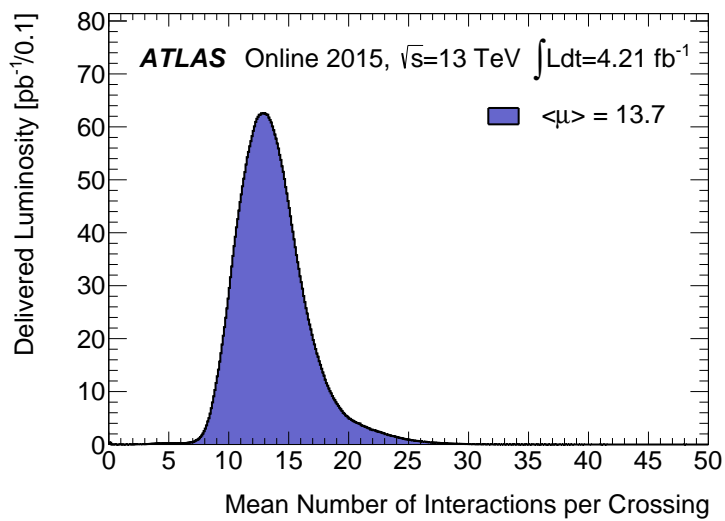


Figure 9: The luminosity-weighted distribution of the mean number of interactions per crossing for the 2015 pp collision data at 13 TeV.

889 THE ATLAS DETECTOR

890 The four major LHC experiments at CERN seek to use the never before matched
891 energies and luminosities of the new collider to explore the boundaries of par-
892 ticle physics and to gain insight into the fundamental forces of nature. Two of
893 these experiments, ATLAS and CMS, are general purpose detectors that seek to
894 measure a variety of processes in the up to 14 TeV proton-proton collisions that
895 occur as much as 40 million times per second at the LHC at the design luminosity
896 of $10^{34} \text{ cm}^{-2}\text{s}^{-1}$. ATLAS employs a hermetic detector design, one which encloses
897 the particle collisions as completely as possible with detecting elements, that al-
898 lows it to study a wide range of physics from SM and Higgs measurements to
899 searches for new physics in models like Supersymmetry [3].

900 Accomodating this wide variety of goals is a challenge for the design of the
901 detector. The wide range of energies involved requires high measurement preci-
902 sion over several orders of magnitude and the ability to measure a variety of par-
903 ticle types. At the time of the construction of ATLAS, the Higgs boson had yet to be
904 discovered, but the diphoton decay mode was (correctly) expected to be impor-
905 tant and necessitated a high resolution photon measurement. The potential for
906 decays of new heavy gauge bosons, W' and Z', required a similarly high momen-
907 tum resolution for leptons with momentum up to several TeV. Hadronic decay
908 modes of several possible new high energy particles could result in very energetic
909 jets, again up to several TeV, and reconstructing the decay resonances would
910 again require good energy resolution. Several models, such as Supersymmetry
911 (SUSY) or Extra Dimensions, predict the existence of particles which would not
912 interact with traditional detecting elements. However these particles can still be
913 observed in a hermetic detector by accurately measuring the remaining event
914 constituents to observe an imbalance in energy called missing energy or E_T^{miss} .
915 Measuring E_T^{miss} implicitly requires a good resolution on all SM particles that can
916 be produced. And at the lower end of the energy spectrum, precision SM mea-
917 surements would require good resolution of a variety of particle types at energies
918 as low as a few GeV, so the design needs to accomodate roughly three orders of
919 magnitude.

920 This broad spectrum of measurements requires a variety of detector systems
921 working together to form a cohesive picture of each collision. Two large magnet
922 systems provide magnetic fields that provide a curvature to the propagation of
923 charged particles and allows for precision momentum measurements by other
924 systems. The inner detector uses a combination of tracking technologies to re-
925 construct particle trajectories and vertexes for charged particles. A variety of
926 calorimeters measure the energies of hadrons, electrons, and photons over a
927 large solid angle. A large muon spectrometer identifies muons and uses the sec-
928 ond magnet system to provide an independent measurement of their momentum

929 from the inner detector and improve the resolution. The layout of all of these
 930 systems is shown in Figure 10.

931 The performance goals needed to achieve the various targeted measurements
 932 and searches discussed above can be summarized as resolution and coverage re-
 933 quirements on each of these systems. Those requirements are listed in Table 2.

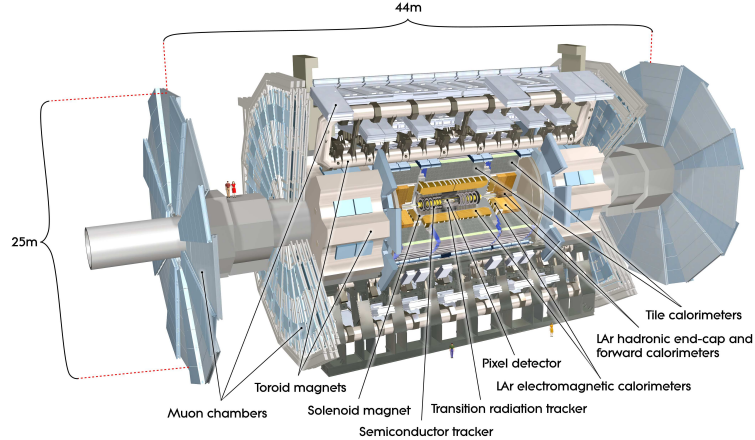


Figure 10: A cut-away schematic of the layout of the [ATLAS](#) detector. Each of the major subsystems is indicated.

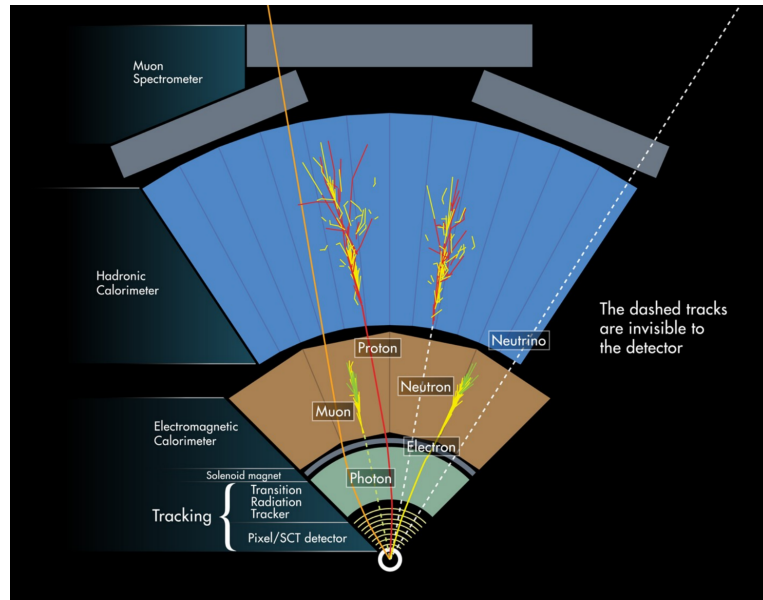


Figure 11: A cross-sectional slice of the [ATLAS](#) experiment which illustrates how the various SM particles interact with the detector systems.

934 Incorporating these various pieces into a single detector is a significant tech-
 935 nical challenge. The resulting detector has a diameter of 22 m, is 46 m long,
 936 and weighs 7,000 tons; it is the largest volume particle detector ever constructed.
 937 The various detector elements need to be constructed and assembled with preci-
 938 sions as low as micrometers. These systems all need to function well even after
 939 exposure to the significant radiation dose from the collisions. Designing, con-

Detector Component	Required Resolution	$ \eta $ Coverage	
		Measurement	Trigger
Tracking	$\sigma_{p_T}/p_T = 0.05\% p_T + 1\%$	2.5	-
EM Calorimetry	$\sigma_E/E = 10\%/\sqrt{E} + 0.7\%$	3.2	2.5
Hadronic Calorimetry			
Barrel and Endcap	$\sigma_E/E = 50\%/\sqrt{E} + 3\%$	3.2	3.2
Forward	$\sigma_E/E = 100\%/\sqrt{E} + 10\%$	3.1 – 4.9	3.1 – 4.9
Muon Spectrometer	$\sigma_{p_T}/p_T = 10\% \text{ at } p_T = 1 \text{ TeV}$	2.7	2.4

Table 2: The performance goals for each of the subsystems of the [ATLAS](#) detector. The $|\eta|$ coverage specifies the range where the subsystem needs to be able to provide measurements with the specified resolution. The resolutions include a p_T or E dependence that is added in quadrature with a p_T/E independent piece.

940 structing, and installing the detector took the combined effort of more than 3000
 941 scientists from 38 countries over almost two decades.

942 6.1 COORDINATE SYSTEM

943 The coordinate system defined for the [ATLAS](#) detector is used throughout all of
 944 the sections of this thesis. The choice of coordinate system reflects the cylind-
 945 rical symmetry of the [ATLAS](#) detector, and is oriented by the direction of the
 946 beamline which defines the z -direction. The positive z side of the detector is
 947 commonly referred to as the A -side, and the negative z side is referred to as
 948 the C -side. The $x - y$ plane is then the plane transverse to the beam direction,
 949 with the x direction defined as pointing from the interaction point to the center
 950 of the [LHC](#) ring and the y direction defined as pointing upwards. The nominal
 951 interaction point is the origin of this system.

952 It is more convenient in practice to use a cylindrical coordinate system. The
 953 angle from the z -axis is θ . The azimuthal angle uses the usual definition, with ϕ
 954 running around the z -axis and $\phi = 0$ corresponding to the x -axis. Many aspects
 955 of the detector are independent of the this coordinate to first order. The re-
 956 maining direction is typically specified using rapidity or pseudorapidity, where
 957 rapidity is defined as

$$y = \frac{1}{2} \ln \frac{E + p_z}{E - p_z} \quad (3)$$

958 Rapidity is particularly useful to indicate the component along the z direction
 959 because differences in rapidity are invariant to boosts along the z -direction. A
 960 similar quantity which depends only the θ is pseudorapidity,

$$\eta = -\ln \tan \frac{\theta}{2} \quad (4)$$

961 which is the same as rapidity when the particle is massless and in the limit where
 962 the energy is much larger than the particle's mass. It is often useful to refer to
 963 differences in solid angle using the pseudorapidity and the azimuthal angle:

$$\Delta R = \sqrt{\Delta\phi^2 + \Delta\eta^2} \quad (5)$$

964 The pseudorapidity is also invariant to boosts along the z -axis for high mo-
 965 mentum particles, and is preferable to rapidity because it does not depend on
 966 the specific choice of particle. Pseudorapidity is also preferable to θ because
 967 of the aforementioned boost-invariance and also because particle production is
 968 roughly uniform in equal-width intervals of η up to about $\eta = 5.0$. A particle
 969 travelling along the beampipe has $\eta = \text{inf}$ and a particle travelling perpendicular
 970 to the beampipe has $\eta = 0$. The extent of the tracker, $|\eta| < 2.5$, corresponds
 971 to approximately $0.05\pi < \theta[\text{rad}] < 0.95\pi$ and the extent of the calorimeters,
 972 $|\eta| < 4.9$ corresponds to approximately $0.005\pi < \theta[\text{rad}] < 0.995\pi$. Many de-
 973 tector components are broken into multiple subsystems to provide coverage at
 974 greater $|\eta|$. The lower $|\eta|$ region is referred to as the barrel, typically with $|\eta| \lesssim 2$,
 975 and the greater $|\eta|$ region is often referred to as the endcap.

976 The initial energy and momentum of a proton-proton collision along the z di-
 977 rection is unknown in hadron colliders because different energies and momen-
 978 tums can be carried by the partons. Along the transverse plane, however, the
 979 vector sum of momentum will be zero. For this reason, many physical quantities
 980 are quantified in terms of their projection onto the transverse plan, such as p_T
 981 or E_T . In addition, p_T alone determines the amount of curvature in the mag-
 982 netic field, and can be measured independently by measuring the curvature of a
 983 particle's propagation.

984 6.2 MAGNETIC FIELD

985 The magnet system used in [ATLAS](#) is designed to provide a substantial magnetic
 986 field in the two regions where the trajectory of particles is measured, the inner
 987 detector and the muon spectrometer. The magnetic field provides a curvature
 988 to the trajectory of charged particles and allows the precision tracking measure-
 989 ments to make high resolutions measurements of p_T . To provide a magnetic field
 990 in these regions, [ATLAS](#) uses a hybrid system with four separate, superconduct-
 991 ing magnets. A single solenoid provides a 2 T axial magnetic field for the inner
 992 detector, while a barrel toroid and two endcap toroids produce a magnetic field
 993 of 0.5 and 1 T, respectively, for the muon detectors. This geometry is illustrated
 994 in Figure 12, and the parameters of the three magnet systems are summarized in
 995 Table ??.

996 The central solenoid uses a single-layer coil with a current of 7.730 kA to gen-
 997 erate the 2 T axial field at the center of the magnet. The single-layer coil design
 998 enables a minimal amount of material to be used in the solenoid's construction,
 999 which is important because the solenoid is placed between the inner detector
 1000 and the calorimeters. At normal incidence the magnet has only 0.66 radiation
 1001 lengths worth of material, where one radiation length is the mean distance over

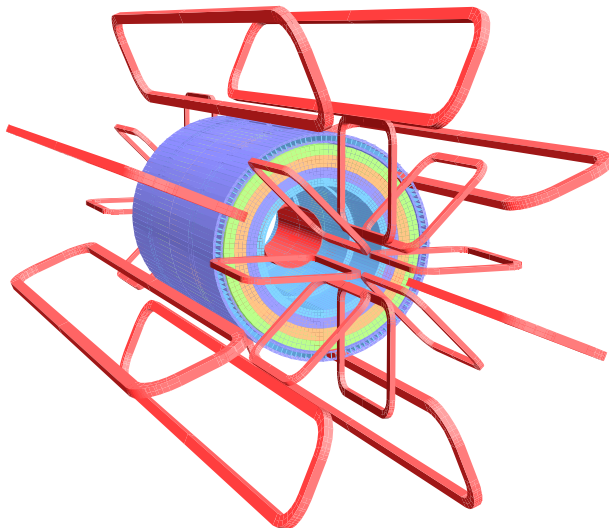


Figure 12: The layout of the four superconducting magnets in the [ATLAS](#) detector.

Parameter	Unit	Solenoid	Barrel Toroid	Endcap Toroids
Inner Diameter	m	2.4	9.4	1.7
Outer Diameter	m	2.6	20.1	10.7
Axial Length	m	5.3	25.3	5.0
Weight	tons	5.7	830	239
Conductor Size	mm ²	30×4.25	57×12	41×4.25
Peak Field	T	2.6	3.9	4.1
Heat Load	W	130	990	330
Current	kA	7.7	20.5	20.0
Stored Energy	MJ	38	1080	206

1002 which a high-energy electron loses all but $1/e$ of its energy through material in-
 1003 teractions [7]. The coil is made of a high-strength aluminum stabilized NbTi
 1004 superconductor which was optimized to achieve a high field with minimal thick-
 1005 ness. The axial magnetic field produced by the solenoid bends charged particles
 1006 in the ϕ direction.

1007 The barrel toroid consists of eight coils which generate a 0.5 T magnetic field
 1008 in the cylindrical region around the calorimeters with an approximately 20 kA
 1009 current. The coils are separated only by air to reduce the scattering of muons as
 1010 they propagate through the region. The coils are made of an aluminum stabilized
 1011 NbTiCu superconductor and each is separately housed in a vacuum and cold
 1012 chamber. This magnetic configuration produces a field in the ϕ and so curves
 1013 muons traversing the volume primarily in the η direction.

1014 The endcap toroids follow a similar design to the barrel toroid, with eight
 1015 separate NbTiCu coils, but in this case all eight are housed within a single cold
 1016 mass. This extra structure is necessary to withstand the Lorentz forces exerted
 1017 by the magnets. These magnets are rotated 22.5% relative to the barrel toroid to
 1018 provide a uniform field in the transition between the two systems. The endcap
 1019 toroids also produce a field in the ϕ direction and curve muons primarily in the
 1020 η direction.

1021 6.3 INNER DETECTOR

1022 The [ATLAS](#) inner detector provides excellent momentum resolution as well as
 1023 accurate primary and secondary vertex measurements through robust pattern
 1024 recognition that identifies tracks left by charged particles. These tracks fulfill a
 1025 number of important roles in the [ATLAS](#) measurement system: they measure the
 1026 momentum of charged particles including electrons and muons, they can iden-
 1027 tify electrons or photon conversions, they assign various particles and jets to
 1028 different vertices, and they provide a correction to E_T^{miss} measurements from
 1029 low energy particles. The system has to be accurate enough to separate tracks
 1030 from dozens of vertices and to resolve each vertex individually, as well as accu-
 1031 rate enough to measure the p_T of very high momentum tracks which curve very
 1032 little even in the large magnetic field. This is accomplished by several indepen-
 1033 dent layers of tracking systems. Closest to the interaction point is the very high
 1034 granularity Pixel detector, which is followed by the [SCT](#) layers. These subdetec-
 1035 tors both use discrete space-points to reconstruct track patterns. The final layer,
 1036 the transition radiation tracker ([TRT](#)), uses many layers of straw tube elements
 1037 interleaved with transition radiation material to provide continuous tracking.
 1038 The arrangement of these subdetectors is shown in Figure 13. To provide the
 1039 desired hermetic coverage, the subdetectors are divided into barrel and endcap
 1040 geometries. Figure 14 shows the layout of the subdetectors in more detail, and
 1041 illustrates how tracks at various pseudorapidities can traverse the subdetectors;
 1042 tracks with $\eta > 1.1$ begin to traverse the endcap subdetectors rather than those
 1043 in the barrel, and tracks with $\eta > 1.7$ use primarily endcap elements. The [IBL](#)
 1044 was not present during the original commissioning of the inner detector and is
 1045 not shown in this figure.

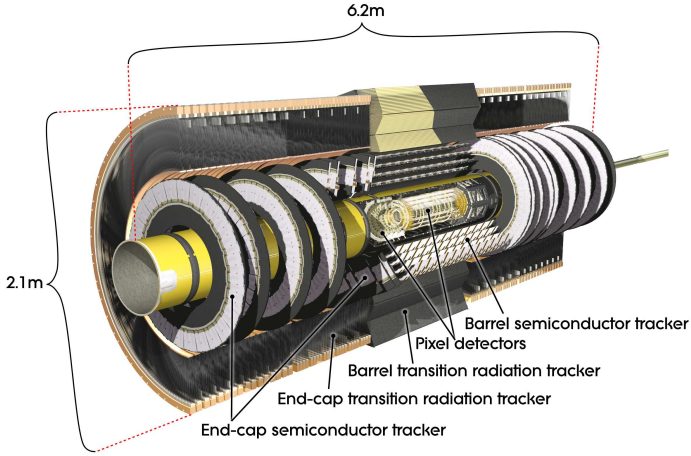


Figure 13: The arrangement of the subdetectors of the ATLAS inner detector. Each of the subdetectors is labelled in the cut-away view of the system.

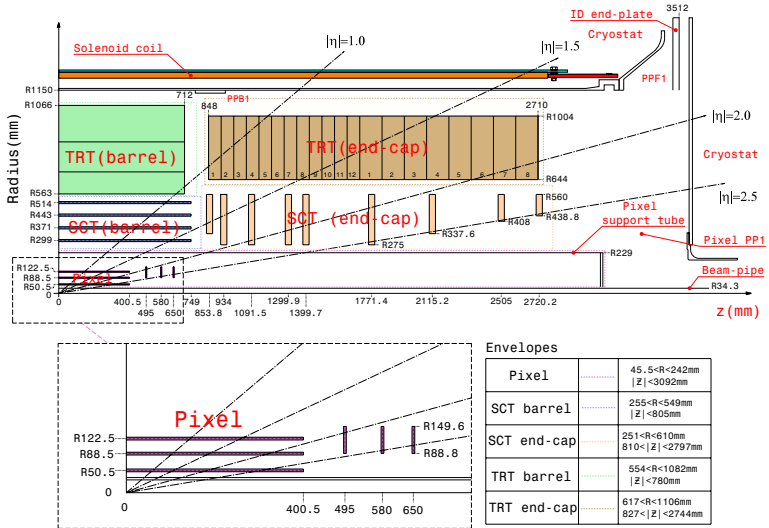


Figure 14: A quarter section of the ATLAS inner detector which shows the layout of each of the subdetectors in detail. The lower panel shows an enlarged view of the pixel detector. Example trajectories for a particle with $\eta = 1.0, 1.5, 2.0, 2.5$ are shown. The IBL, which was added after the original detector commissioning, is not shown.

1046 Figure 15 shows a computer generated three-dimensional view of the inner
 1047 detector along the beam axis, which emphasizes the straw tube structure of the
 1048 **TRT** as well as the overlapping geometry of the **SCT**. This figure also includes
 1049 the **IBL**, which was added during the long shutdown and provides an additional
 1050 measurement layer in the Pixel detector as of the beginning of Run 2. Figure 16
 1051 shows an alternative computer generated three-dimensional view transverse to
 1052 the beam axis which emphasizes the endcap structures of the **SCT** and **TRT**.

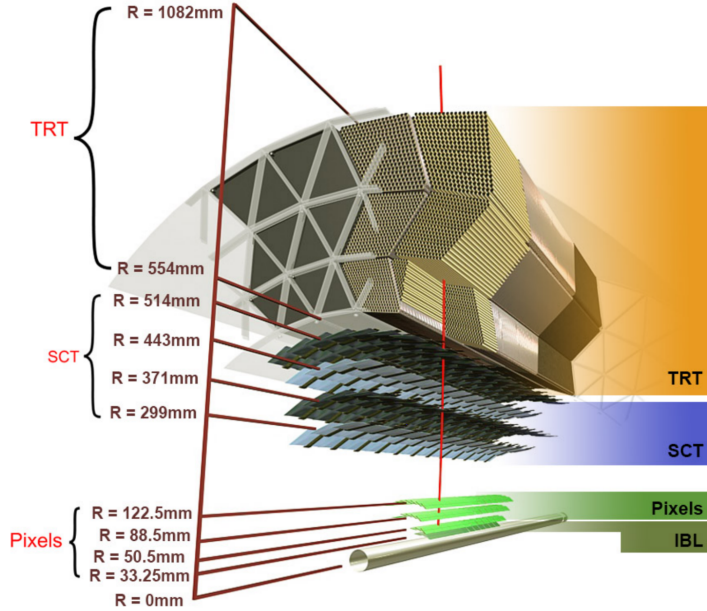


Figure 15: A computer generated three-dimensional view of the inner detector along the line of the beam axis. The subdetectors and their positions are labelled.

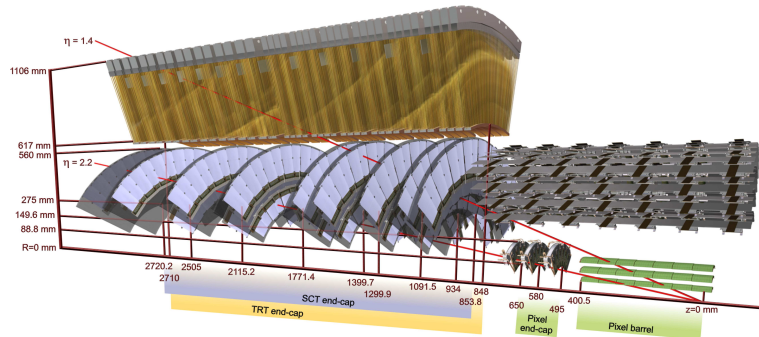


Figure 16: An alternative computer generated three-dimensional view of the inner detector transverse to the beam axis. The subdetectors and their positions are labelled.

1053 As the closest system to the interaction point, it is crucial for the inner de-
 1054 tector to use as little material as possible to avoid scattering of charged parti-
 1055 cles or photon conversions before they reach the remaining subdetectors. The
 1056 various components, including the readout electronics, cooling infrastructure,
 1057 gas volumes, and support structures, were designed to use as little material as

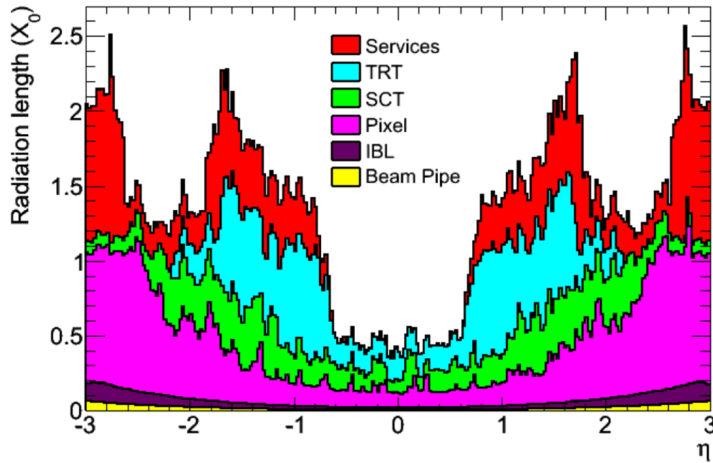


Figure 17: The integrated radiation lengths traversed by a straight track at the exit of the ID envelope, including the services and thermal enclosures. The distribution is shown as a function of $|\eta|$ and averaged over ϕ . The breakdown indicates the contributions of individual sub-detectors, including services in their active volume.

possible. Even with these optimizations, the combination of stringent performance requirements and the harsh radiation environment in the inner detector requires a significant amount of material. This material causes many electrons to lose most of their energy before reaching the electromagnetic calorimeter and approximately 40% of photons convert into an electron-positron pair while traversing the inner detector. Figure 17 shows the integrated radiation lengths traversed by a straight track in the inner detector as a function of η , grouped by subdetector. There is a large increase in the amount of material for support structures around $|\eta| = 1.7$, where the inner detector transitions from barrel to endcap.

The inner detector is designed to work as a cohesive unit to provide complete tracking information for charged particulars, and the subdetectors are complementary. Table ?? summarizes the parameters of each of the subdetectors as well as the parameters of the combined inner detector. Table ?? summarizes the expected performance that can be achieved by the inner detector as a whole.

6.3.1 PIXEL DETECTOR

The Pixel detector is the closest detector to the interaction point and therefore is designed to provide extremely high granularity while simultaneously handling a very large dose of radiation from collisions. It consists of four layers of silicon pixel modules, each of which provides a precision measurement on the trajectory of any charged particle. In the barrel region, the four layers are located at radial distances of 31 mm, 51 mm, 89 mm, and 123 mm. The three outer layers also include endcap elements, illustrated in Figure 14, which are located at 495 mm, 580 mm, and 650 mm away from the interaction point.

Parameter	Inner Detector	Pixel	SCT	TRT
Inner Radius	3.1 cm	3.1 cm	30 cm	56 cm
$ \eta $ Coverage	-	2.5	2.5	2.0
Cell Width	-	50 μm	80 μm	4 mm
Cell Length	-	400 μm	12 cm	70 cm
Material at $ \eta = 0.0$	$0.3 X/X_0$			
Material at $ \eta = 1.7$	$1.2 X/X_0$			
Material at $ \eta = 2.5$	$0.5 X/X_0$			
Number of Hits	48	4	8	36
Channels	99 M	92 M	6.3 M	350 k

Table 3: A summary of the parameters of the inner detector and each of the subdetectors [3].

1082 The pixel sensor technology uses a p-n junction of n-type bulk that contains
 1083 both p⁺ and n⁺ impurities. This combination is crucial in maintaining perfor-
 1084 mance after a significant radiation dose, as the n⁺ implants allow the sensor to
 1085 continue function after the n-type bulk has been converted to a p-type bulk by
 1086 the accumulation of radiation.

1087 The size of the pixels in the original three layers are 50 $\mu\text{m} \times$ 400 μm in the
 1088 $r - \phi$ and z directions, respectively. Those pixels are bump-bonded to front-end
 1089 readout chips, the FE-I3, which contains a total of 2880 pixels per chip. In the
 1090 three original pixel layers, the chips are grouped into modules composed of 16
 1091 chips each with 46,080 pixels per module and a total size of 20 mm x 60 mm
 1092 x 250 μm . The modules are further arranged into long rectangular structures
 1093 that run parallel to the beamline called staves. By tiling several staves with an
 1094 offset of 20°, the stave geometry provides full azimuthal coverage in the barrel
 1095 region while accomodating the readout and cable systems. The endcap regions
 1096 are instead arranged into petals and then into wheels. This arrangement can
 1097 be seen in Figure 18 which shows a computer-generated, cut-away image of the
 1098 outer three layers of the pixel detector. Together these three layers contain 1744
 1099 modules between the barrel and two endcap sections.

1100 The innermost layer, the IBL, was added during the long shutdown before Run
 1101 2, and provides the fourth track measurement. It was inserted directly into the
 1102 existing pixel detector by removing the existing beam pipe and replacing it with
 1103 a significantly smaller version. This insertion can be seen in action in Figure 19,
 1104 which emphasizes the extreme precision required to place the the 70 cm long
 1105 layer with only 2 mm of clearance. The IBL was commissioned to provide con-
 1106 tinued tracking robustness and high precision in the higher luminosity environ-
 1107 ment of Run 2 [9]. The proximity of this layer to the collisions necessitated an
 1108 even higher granularity and better radiation hardness than the other pixel lay-
 1109 ers. And the strict space requirements to add an active sensing layer so close to
 1110 the interaction point required a sensor chip with a much higher active area and
 1111 a larger overall area per chip. These requirements led to the development of a

Parameter	Particle	Value
Reconstruction Efficiency	Muon, $p_T = 1 \text{ GeV}$	96.8%
	Pion, $p_T = 1 \text{ GeV}$	84.0%
	Electron, $p_T = 5 \text{ GeV}$	90.0%
Momentum Resolution	$p_T = 1 \text{ GeV}, \eta \approx 0$	1.3%
	$p_T = 1 \text{ GeV}, \eta \approx 2.5$	2.0%
	$p_T = 100 \text{ GeV}, \eta \approx 0$	3.8%
	$p_T = 100 \text{ GeV}, \eta \approx 2.5$	11%
Transverse IP Resolution	$p_T = 1 \text{ GeV}, \eta \approx 0$	$75 \mu\text{m}\%$
	$p_T = 1 \text{ GeV}, \eta \approx 2.5$	$200 \mu\text{m}$
	$p_T = 1000 \text{ GeV}, \eta \approx 0$	$11 \mu\text{m}$
	$p_T = 1000 \text{ GeV}, \eta \approx 2.5$	$11 \mu\text{m}$
Longitudinal IP Resolution	$p_T = 1 \text{ GeV}, \eta \approx 0$	$150 \mu\text{m}\%$
	$p_T = 1 \text{ GeV}, \eta \approx 2.5$	$900 \mu\text{m}$
	$p_T = 1000 \text{ GeV}, \eta \approx 0$	$90 \mu\text{m}$
	$p_T = 1000 \text{ GeV}, \eta \approx 2.5$	$190 \mu\text{m}$

Table 4: A summary of the expected performance of the combined inner detector [8]. Included are the reconstruction efficiencies for multiple particle types as well as the momentum and IP resolution for various momenta.

new chip type, the FE-I4 (compared to the FE-I3 chips used in the original pixel detector) with improved radiation hardness and a larger active footprint of 90%. The IBL is comprised of 448 of these individual chips arranged in 14 staves, with 26,880 pixels per chip and a chip size of 18.5 mm x 41.3 mm x 200 μm . The staves, like in the other layers of the pixel detector, are offset by 14° to provide full azimuthal coverage. This arrangement can be seen in Figure 20, which shows two computer-generated images of the IBL geometry and includes the some of the remaining pixel layers.

6.3.2 SEMICONDUCTOR TRACKER

The SCT, the subdetector which immediately surrounds the Pixel detector, provides additional discrete measurements of the trajectory of a charged particle. Because the SCT is further away from the interaction point, the spatial resolution does not need to be as high as in the pixel detector, and so the SCT uses micro-strips instead of pixels. Although pixels provide a more accurate measurement, the number of pixels and readout channels required to cover the cylindrical area at the radius of the SCT layers would be prohibitively complicated and expensive.

Each individual silicon strip sensor contains 768 individual readout strips with a total area of 6.36 cm x 6.40 cm and a pitch of 80 μm . Pairs of these sensors are then bonded together to form a combined strip with a length of 12.8 cm. Two of these combined strips are then placed back to back with a relative tilt

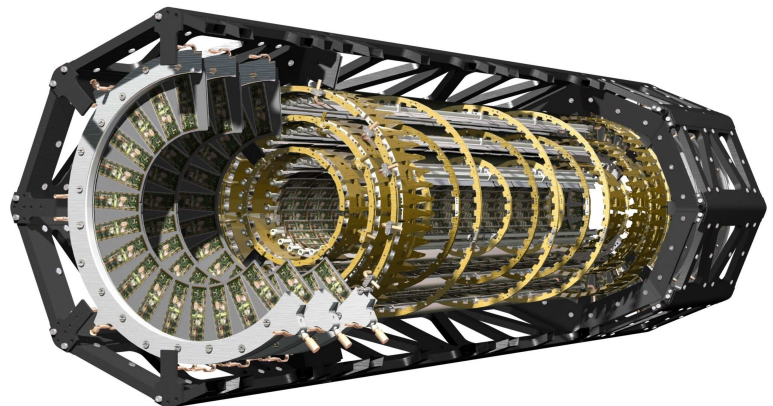


Figure 18

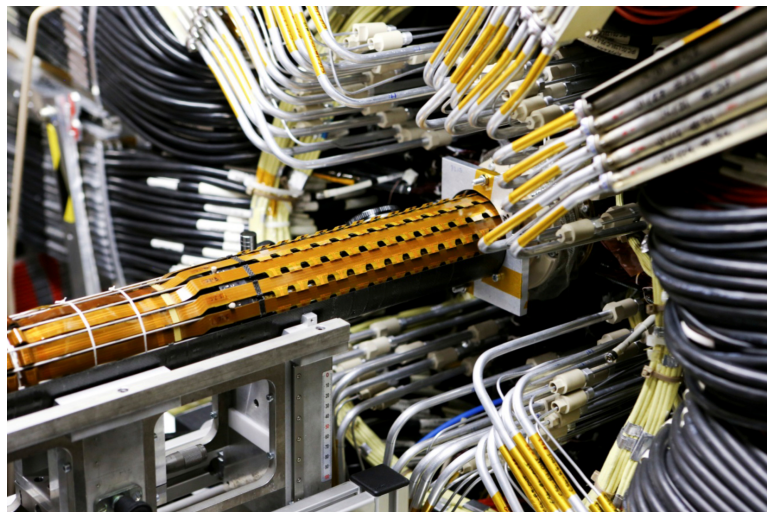


Figure 19: An image of the insertion of the [IBL](#) into the current pixel detector.

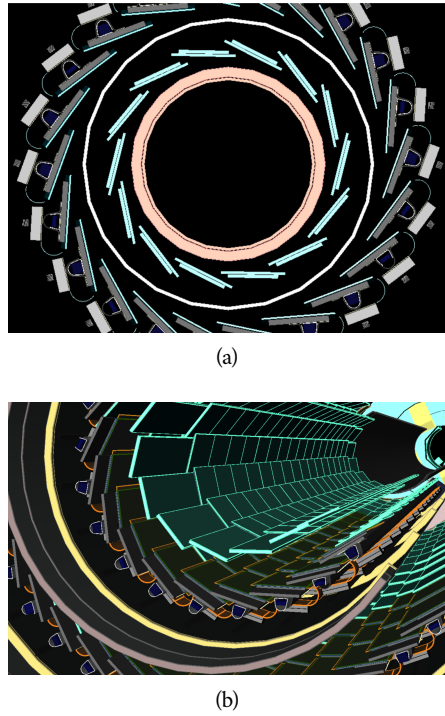


Figure 20: A three-dimensional computer-generated image of the geometry of the [IBL](#) with a view (a) mostly transverse to the beam pipe (b) mostly parallel to the beam pipe.

of 40 mrad. This geometry is illustrated in an exploded-out view in Figure 21. The purpose of angular offset of the consecutive layers is to allow the strip sensor areas to more accurately measure the position of a particle by comparing the overlap of the two strips which were traversed by a track.

Four of these double layers are placed in the barrel region, with radii of 284 mm, 355 mm, 427 mm, and 498 mm. Together these layers provide eight additional measurements for each track that traverses the central $|\eta|$ region. In the endcap region, the layers are arranged in wheels, with the double layers similarly offset to provide improved resolution. With these configurations, the [SCT](#) achieves a spatial resolution of $17 \mu\text{m}$ in the $r - \phi$ direction and $580 \mu\text{m}$ in the z direction.

6.3.3 TRANSITION RADIATION TRACKER

The final component of the inner detector, the [TRT](#), provides continuous tracking using straw drift tubes. The tubes are made of Kapton and aluminum with a diameter of 4 mm and are filled with a gas mixture of 70% Xe, 27% CO₂, and 3% O₂. At the center of each tube is a gold-plated anode tungsten wire $30 \mu\text{m}$ in diameter. When a charged particle passes through these tubes, it ionizes the gas within. The ions produced drift in the electric field established between the wire and the tube wall, and the large electric field near the wire produces avalanche multiplication and results in an electric current on the wire that is read out by the electronics and provides a track measurement. The time it takes the ioniza-

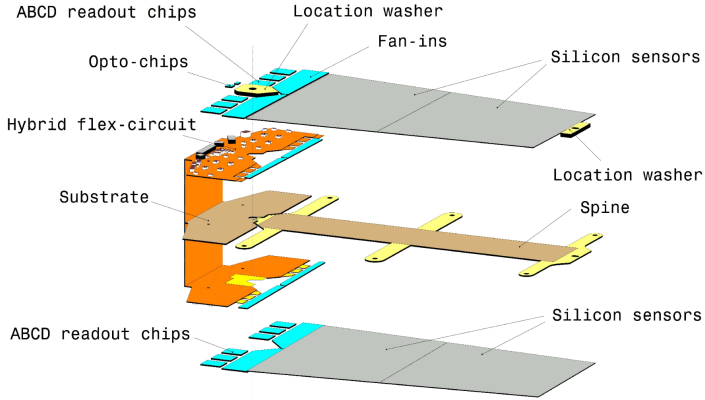


Figure 21: An exploded view of the geometry of the [SCT](#) double layers in the barrel region.

tion to drift to the wire can be used to estimate the distance from the wire that the particle passed through the tube; this gives a resolution on the distance of approximately $130\mu\text{m}$. Combining several such measurements between consecutive hits in the [TRT](#) tubes allows the trajectory of the particle to be reconstructed.

In addition to the continuous tracking, the detector can use transition radiation produced when a particle passes between the layers to distinguish between electrons and heavier charged particles. The space between the tubes is filled with CO_2 , and so has a different dielectric constant than the gas within the tubes which contains Xe. At the transition between those media, a relativistic particle emits radiation proportional to γ , so inversely proportional to mass at a fixed momentum. The photons produced in this transition then produces an ionization cascade which is significantly larger than the signal for the minimally-ionizing charged particles. To distinguish between these two cases, the [TRT](#) defines two signal thresholds, a low threshold for the typical signal produced by a minimally ionizing particle ([MIP](#)) and a high threshold for the the signal produced by transition radiation. A high momentum electron is expected to produce approximately 7 to 10 high threshold hits as it traverses the [TRT](#), and thus these hits provide a way to distinguish electrons from other charged particles.

The [TRT](#) contains 351,000 tubes in total, divided between the barrel and endcap regions. In the barrel region, the tubes are 144 cm long and arranged in 73 layers parallel to the beampipe. In the endcap region, the tubes are 37 cm long and arranged in 160 layers transverse to the beampipe. These configurations can be seen in Figure 15 and Figure 16. With this geometry the [TRT](#) achieves a resolution of $130\mu\text{m}$ in the $r - \phi$ direction.

6.4 CALORIMETRY

The combination of calorimeter systems used in [ATLAS](#) can measure the energy of electrons, photons, hadrons, and hadronic jets with complete coverage up to $|\eta| < 4.9$ and across ϕ . Unlike the inner detector, the calorimeters are capable of measuring neutral particles. To accomplish precision measurements of these

1182 particle types, the [ATLAS](#) calorimeter system uses four individual calorimeters,
 1183 a [LAr](#) electromagnetic calorimeter in the barrel region, a tile hadronic calorime-
 1184 ter in the barrel region, a [LAr](#) hadronic endcap calorimeter, and a [LAr](#) forward
 1185 calorimeter. Together these provide hermetic coverage for the [ATLAS](#) detector.
 1186 The configuration of these calorimeters is illustrated in Figure 22. **Note: I could**
 1187 **make this section much longer. It might be nice to include a more com-**
 1188 **plete description of showers for example. I will extend this section if their**
 1189 **is space at the end.**

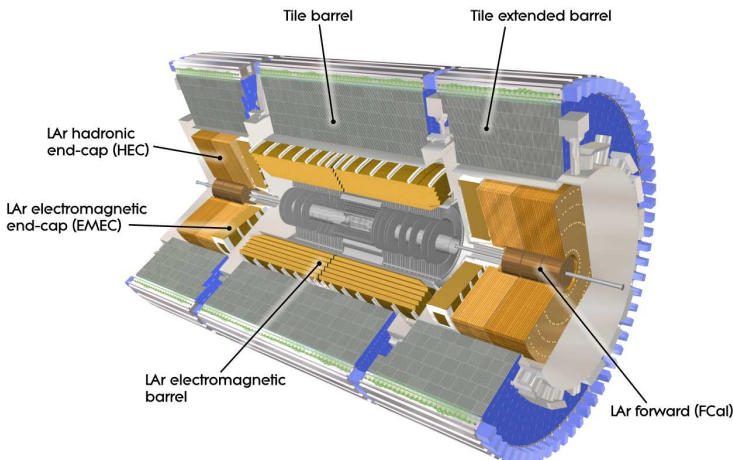


Figure 22

1190 The calorimeters are designed to absorb and measure the energy carried by
 1191 a particle, and completely stop the particle's propagation in the process. This
 1192 requires a significant amount of material to provide interactions. These interac-
 1193 tions then produce secondary particles, which can produce secondary particles
 1194 in turn, and thus form a cascade of particles called an electromagnetic ([EM](#)) or
 1195 hadronic shower, depending on the governing mechanism. Electromagnetic and
 1196 hadronic showers have very different properties and require different technolo-
 1197 gies to measure them accurately. All of the calorimeters in the [ATLAS](#) calorimeter
 1198 system are sampling calorimeters, that is they use alternating layers of absorbing
 1199 and active material. The dense absorbing layers initiate the showers while the ac-
 1200 tive layers measure the energy of the produced particles. A fraction of the energy
 1201 is lost in the inactive layers, so the energy measurement from the active layers
 1202 has to be corrected to estimate the actual energy of the particle.

1203 The [EM](#) calorimeter provides around 20 radiation lengths (X_0) while the hadronic
 1204 calorimeter provides around 10 interaction lengths (λ_0). As mentioned previ-
 1205 ously, radiation lengths measure the distance over which an electromagnetically
 1206 interacting particle loses a characteristic fraction of its energy. Interaction lengths,
 1207 on the other hand, measure the mean distance travelled by a hadronic particle be-
 1208 fore undergoing a nuclear interaction [7]. Figure 23 show the radiation lengths
 1209 in the layers of the [EM](#) calorimeter in the barrel region as well as the interaction
 1210 lengths for all calorimeters.

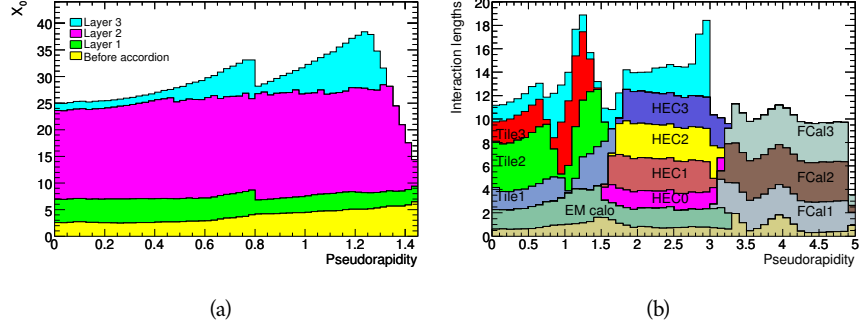


Figure 23: The depth of (a) the electromagnetic barrel calorimeter in radiation lengths and (b) all calorimeters in interaction lengths as a function of pseudorapidity.

1211 6.4.1 ELECTROMAGNETIC CALORIMETER

1212 The electromagnetic calorimeters use alternating layers of Liquid Argon
 1213 and lead in an accordion shape. The accordion shape allows a construction that pro-
 1214 vides complete coverage in the ϕ direction while also providing many alterna-
 1215 ting layers for the a particle to pass through. The configuration is detailed in
 1216 Figure 24. When an electron or photon passes through the lead, it produces an
 1217 electromagnetic shower. The particles produced in those showers then pass into
 1218 and ionize the Liquid Argon; the ions produced can then be collected by an elec-
 1219 trode in the Liquid Argon layer to provide the actual energy measurement.

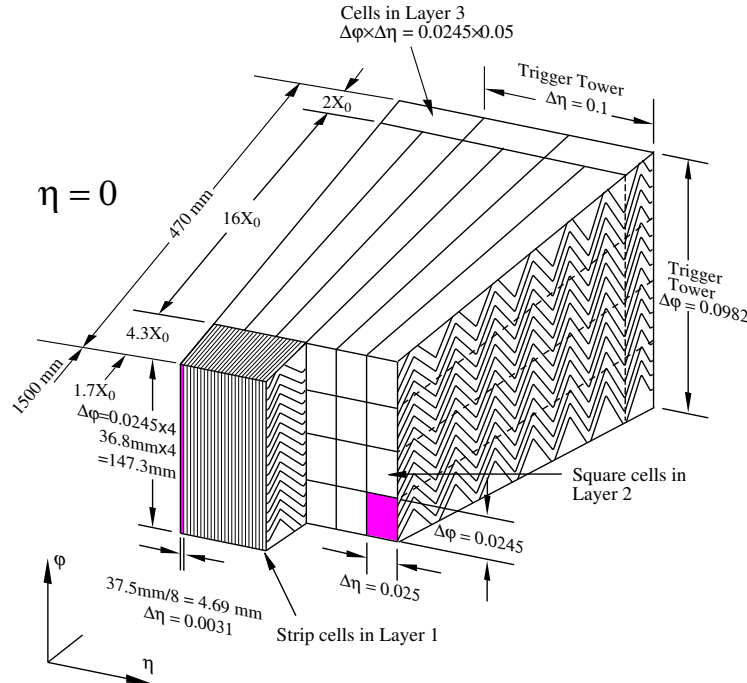


Figure 24: A schematic of the LAr calorimeter in the barrel region, highlighting the ac-
 cordion structure.

The barrel region is covered by a presampler and three separate sampling layers with decreasing segmentation. The presampler is just a thin layer of Liquid Argon which measures the energy of any electromagnetic showers which are initiated before the particle reaches the calorimeter due to interactions with the detector material. The first layer is the strip layer, which has fine segmentation in η to enhance the identification of shower shapes and to provide a precise η measurement for reconstructing photons and electrons. The strip layer has only 4 radiation lengths worth of material, and has a segmentation of $\Delta\eta = 0.003$ and $\Delta\phi = 0.1$. The second layer is also finely segmented, with a segmentation of $\Delta\eta = 0.025$ and $\Delta\phi = 0.025$, and a thickness of $16 X_0$. This layer is designed to contain an electromagnetic shower and to measure the majority of the energy for photons and electrons. The third layer is only $2 X_0$ thick and measures the energy of electromagnetic showers which leak out of the second layer, and helps to separate electromagnetic showers from hadronic showers. The structure of the LAr endcap calorimeter is similar except that the layers are arranged parallel to the beampipe to measure energy deposits from high η particles.

6.4.2 HADRONIC CALORIMETERS

The hadronic calorimeters use a few different technologies to satisfy the resolution demands in the different areas of the detector, and together they cover the region $|\eta| < 2.7$. In the barrel region, for $|\eta| < 1.7$, the hadronic calorimeters are constructed of alternating tiles of steel and plastic scintillator. Like in the electromagnetic calorimeter, the dense layer initiates a shower (in this case the dense layer is the steel and the shower is hadronic) of particles which pass into and ionize the following layer. The ionization in the plastic scintillator instead produces a light signal proportional to the amount of ionization produced by the shower, and this signal is measured using photomultipliers and provides the actual energy measurement. The construction of a tile in the calorimeter is shown Figure ??, which highlights the alternating layers of steel and scintillator.

This tile calorimeter, as well as the remaining hadronic calorimeters, have a much coarser granularity than the electromagnetic calorimeters. The high granularity is not needed for an accurate energy measurement, and the hadronic calorimeters are not designed to distinguish particle types like the electromagnetic calorimeters. The tile granularity is approximately $\Delta\eta = 0.1$ and $\Delta\phi = 0.1$, and the segmentation in depth and η is shown in Figure 26.

The remaining hadronic calorimeters all use the same alternating, sampling structure but with different active and inactive materials. The hadronic endcap calorimeter covers the range of $1.5 < |\eta| < 3.2$ and uses an inactive layer of copper and an active layer of **liquid argon!**. The forward calorimeter covers the range of $3.1 < |\eta| < 4.9$ and uses a dense matrix of copper and tungsten filled with Liquid Argon.

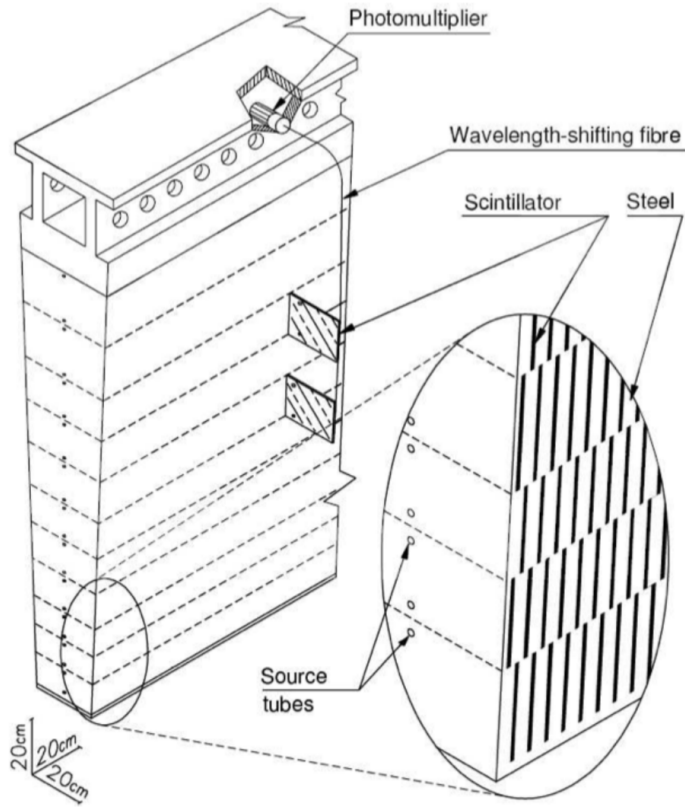


Figure 25: A schematic of a hadronic tile module which shows the alternating layers of steel and plastic scintillator.

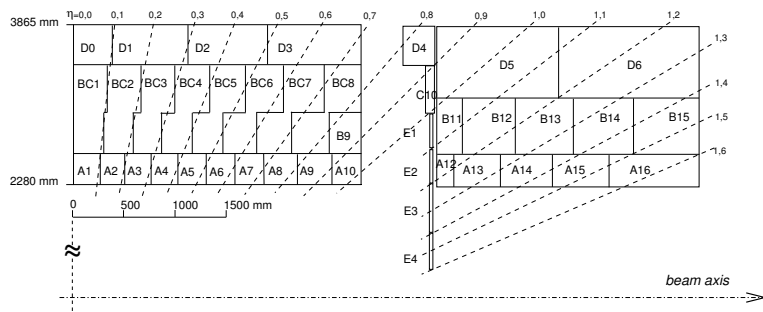


Figure 26: The segmentation in depth and η of the tile-calorimeter modules in the central (left) and extended (right) barrels.

1260 6.5 MUON SPECTROMETER

1261 Among SM particles, only muons and neutrinos consistently pass through the
 1262 calorimeters. Because the neutrinos are also electrically neutral, there is no fea-
 1263 sible option to measure them directly in ATLAS. The muons, on the other hand,
 1264 are charged and are thus already measured as a track in the inner detector. The
 1265 muon spectrometer provides a way to consistently identify muon tracks and also
 1266 a way to provide an additional measurement of their momentum.

1267 The muon spectrometer contains four subdetectors that cover the barrel and
 1268 endcap regions. In the barrel region, the muon spectrometer uses a combina-
 1269 tion of RCP!s (RCP!s) and MDTs to provide both a coarse, fast measurement for
 1270 triggering and a precise momentum measurement for offline event reconstruc-
 1271 tion. Similarly, in the endcap region, the TGCs, MDTs, and CSCs allow for both
 1272 triggering and precise measurements. The CSCs are used only in the innermost
 1273 layer of the endcap region between $2.0 < |\eta| < 2.7$ where the particle flux is too
 1274 large for the MDTs to provide accurate measurements. The overall layout of the
 1275 muon systems are shown in the cut-away diagram in Figure 27, and Figure 28
 1276 shows a precise schematic of the layout of each of the detecting elements. The ge-
 1277 ometric arrangement shown provides consistent coverage for muons produced
 1278 up to $|\eta| < 2.7$, and takes full advantage of the bending of the muons in the
 1279 toroidal magnetic field, described in Section 6.2, to measure their momentum.
 1280 Figure 29 shows a cross-section of the arrangement of the muon spectrometer
 1281 in the barrel; the layers are divided into eight small and eight large chambers that
 1282 are overlapped to provide complete coverage in ϕ .

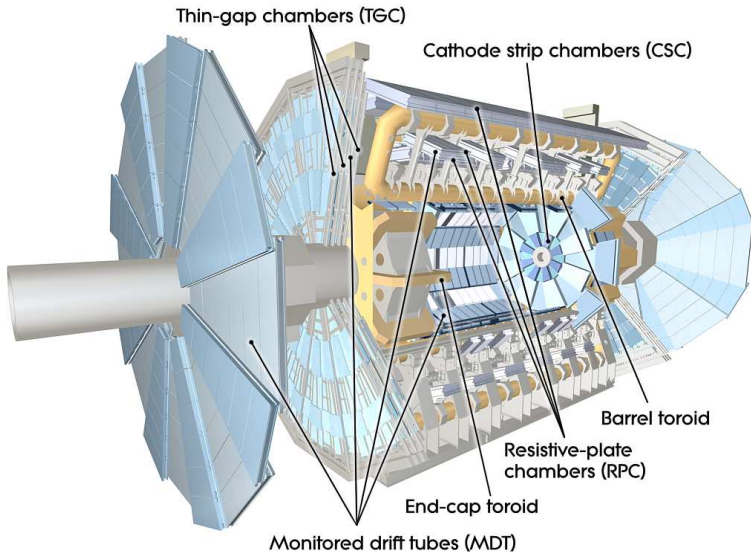


Figure 27: A cut-away diagram of the muon systems on ATLAS.

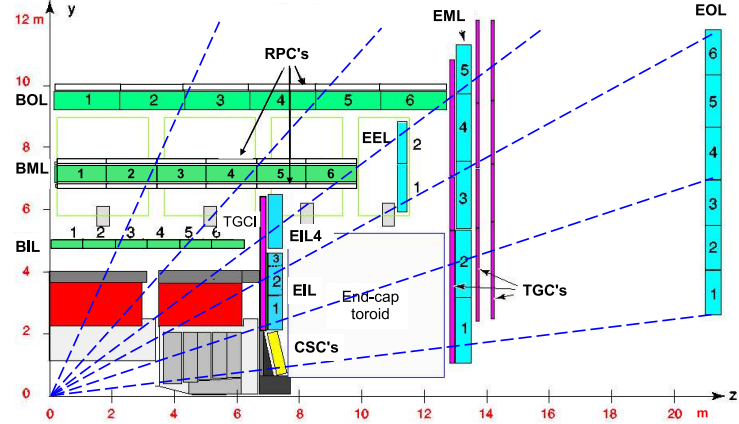


Figure 28: A quarter view of the muon spectrometer which highlights the layout of each of the detecting elements. The BOL, BML, BIL, EOL, EML, and EIL are all MDT elements, where the acronyms encode their positions.

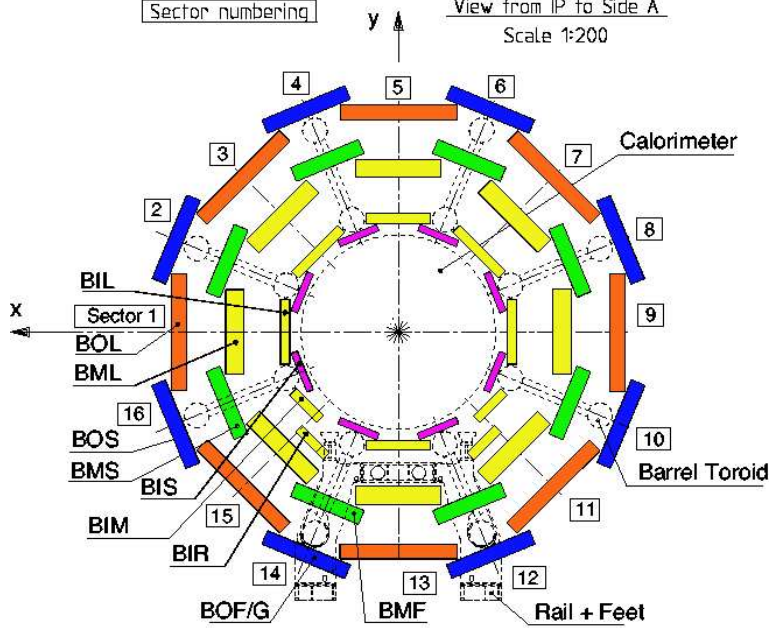


Figure 29: A schematic of the cross-section of the muon spectrometer in the barrel region.

1283 6.5.1 MONITORED DRIFT TUBE

1284 The momentum measurements in the barrel region are provided by three con-
 1285 secutive layers of MDT elements, located at approximately 5 m, 7 m, and 9 m from
 1286 the interaction point. Each of these layers is a composite of two multilayers of
 1287 drift tubes: two layers of three to four layers of tubes, as shown in Figure 30.
 1288 These aluminum tubes are 3 cm in diameter, with lengths between 0.9 and 6.2 m,
 1289 and are filled with a mixture of ArCO₂ kept at 3 bar absolute pressure. A central
 1290 tungsten-rhenium wire with a diameter of 50 μm runs along the length of the
 1291 tube, and is kept at a potential of 3080 V.

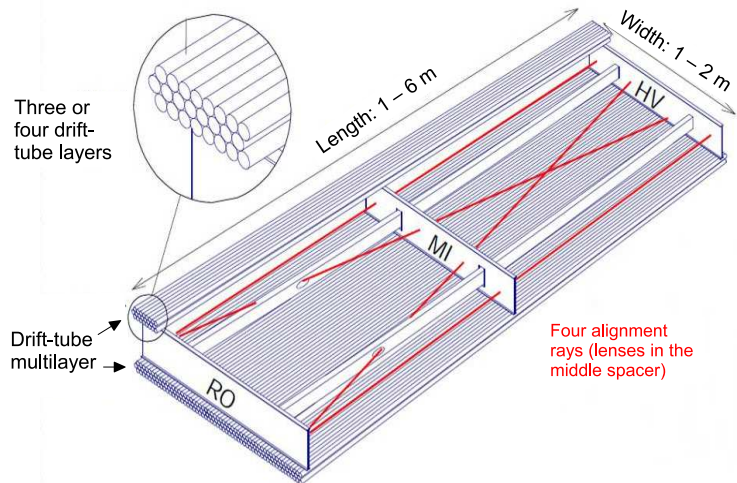


Figure 30: A schematic of a single MDT chamber, which shows the multilayers of drift tubes as well as the alignment system.

1292 A muon traversing these tubes ionizes the gas, and the ionization electrons
 1293 then drift in the electric field toward the central wire. Close to the wire, the
 1294 electric field is strong enough to cause the original ionization electrons to ion-
 1295 ize additional electrons, producing an avalanche that can be measured as a cur-
 1296 rent along the wire. The time of arrival of that current depends on how far the
 1297 muon entered from the wire, and can be used to achieve a position resolution of
 1298 80 μm in an individual tube. The combination of the measurements in the con-
 1299 secutive layers of tubes improves this position resolution to 35 μm .

1300 To achieve a good resolution over the entire length of a muon track, the rel-
 1301 ative positions of the tubes of the muon spectrometer must be known to an ac-
 1302 curacy of 30 μm . This is achieved by an optical laser alignment system placed in
 1303 each of the individual chambers and throughout the cavern. These monitor any
 1304 changes in position or alignment due to effects like gravitational sag, tempera-
 1305 ture shifts, and the magnetic field. The configuration of the alignment system
 1306 within an individual chamber is also shown in Figure ??.

1307 6.5.2 RESISTIVE PLATE CHAMBER

1308 The Resistive Plate Chamber ([RPC](#)) is the outermost detecting layer in the muon
 1309 spectrometer in the barrel region, and provides a fast measurement of the ϕ po-
 1310 sition of muons for triggering. The speed of the measurement, with a time res-
 1311 olution of just a few nanoseconds, requires a poor spatial resolution of approxi-
 1312 mately 1 cm. There are three [RPCs](#) layers in the muon spectrometer, two located
 1313 on either side of the central [MDT](#) layer and one located outside the final [MDT](#)
 1314 layer, as shown in Figure 28. The [RPCs](#) consist of two layers of parallel plates
 1315 filled with a gas mixture of $C_2H_2F_4$. A muon passing through these systems ion-
 1316 izes the gas, like in the [MDT](#), which causes an avalanche of ionization electrons
 1317 in the electric field maintained between the plates. Metal strips on the outside
 1318 of the chamber capacitively couple to the accumulated charge, and are read out
 1319 to measure the η and ϕ positions of the muon track.

1320 6.5.3 CATHODE STRIP CHAMBER

1321 The majority of the momentum measurements in the endcap region are provided
 1322 by the [MDTs](#). In the most forward region of the muon spectrometer, between
 1323 $2.0 < \eta < 2.7$, the particle flux is very high due to contributions from low energy
 1324 photons and neutrons. The [MDT](#) can only sustain a hit rate of approximately 150
 1325 Hz/cm² because of limitations in the drift times of the gas and the capacity of
 1326 the readout electronics. The [CSCs](#) were designed to handle higher hit rates, up to
 1327 1000 Hz/cm², and provide the necessary coverage in that high flux region.

1328 The [CSC](#) consists of several multiwire proportional chambers, where the wires
 1329 are oriented in the radial direction out from the beampipe. There are eight large
 1330 and eight small chambers, arranged to partially overlap in the ϕ direction, as
 1331 shown in Figure ???. Like in the [MDT](#), a muon traversing the system produces
 1332 ionization in the gas; here, however, the ionization is collected on a number of
 1333 wires. These wires couple to cathodes on the chambers which are segmented
 1334 into strips in two directions. The relative amount of charge on each of the neigh-
 1335 boring strips can be used to interpolate to the position of the muon in both η
 1336 and ϕ .

1337 6.5.4 THIN GAP CHAMBER

1338 Like in the barrel region, a separate, fast detector is required to provide position
 1339 measurements of muons for trigger in the endcap region. This is provided by
 1340 the [TGC](#) which consists of seven layers in the middle station of the endcap, two
 1341 doublet layers and one triplet layer, and a single doublet layer in the inner endcap
 1342 station. Figure 32 shows the arrangement of the triple and doublet layers of the
 1343 [TGCs](#).

1344 Like the [CSCss](#), the [TGCs](#) are multiwire proportional chambers with a wire-to-
 1345 cathode distance of 1.4 mm and a wire-to-wire distance of 1.8 mm. Readout
 1346 strips on the outside of the chambers run perpendicular to the wires, and couple
 1347 to the charge collected on the wires to provide a position measurement in the η

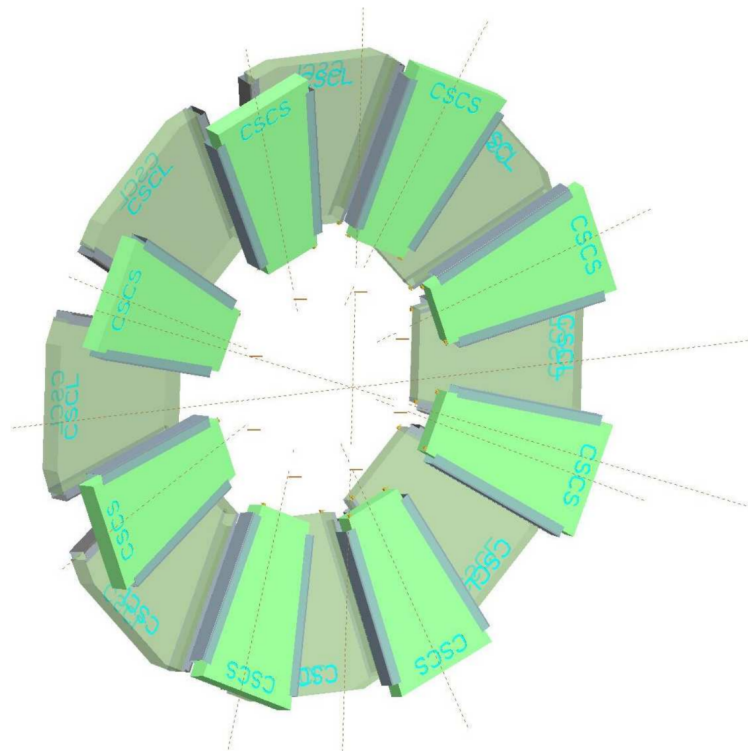


Figure 31: A schematic of the **CSC** endcap, showing the overlapping arrangement of the eight large and eight small chambers.

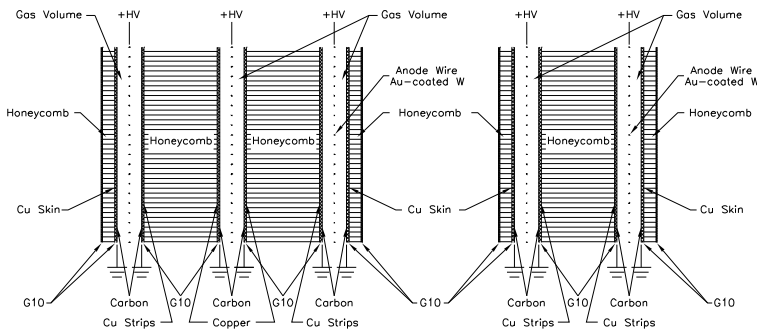


Figure 32: A schematic of the **TGC** doublet and triplet layers.

1348 direction. The current induced on the wires is also readout to provide a position
 1349 measurement in the ϕ direction. The high electric field and small wire-to-wire
 1350 distance give it the required good time resolution to be used for triggering events.

1351 6.6 TRIGGER

1352 It is not possible for the detector and the associated computing systems to record
 1353 the terabytes of data that the 40 MHz of proton-proton collisions produce every
 1354 second. Instead, a small fraction of these events are selected by the trigger sys-
 1355 tem to be recorded and later analyzed. Selecting interesting events at such a high
 1356 rate poses a significant challenge for both the detector design and the imple-
 1357 mentation of a trigger decision and data acquisition system. The trigger must
 1358 balance the time needed to decide to keep an event, to avoid losing information,
 1359 with the filtering accuracy to consistently select a full menu of physics events
 1360 that can be used for the wide array of searches and measurements targeted by
 1361 **ATLAS!** (**ATALS!**).

1362 The [ATLAS](#) trigger system, as of Run 2, consists of two levels of decision mak-
 1363 ing. The first level, referred to as L1, is hardware based and uses inputs from
 1364 a subset of the detector elements to narrow the considered event rate from the
 1365 original 40 MHz down to 100 kHz. The 100 kHz rate is the maximal rate that
 1366 the event information can be transferred from the detector. The second level,
 1367 referred to as the [HLT!](#), makes the final decisions on which events to keep for
 1368 analysis and selects a rate of around 1 kHz. The collection of selection criteria
 1369 used to make the L1 decisions feed into subsequent selection criteria in the [HLT!](#),
 1370 and the set of these combinations of L1 and [HLT!](#) criteria from the trigger menu
 1371 which defines exactly what events are recorded on [ATLAS](#). The entirety of the
 1372 trigger menu used for 2015 data collection is shown in Table 5, which summa-
 1373 rizes the selection requirements at both levels and additionally shows the peak
 1374 measured rates contributed by each.

1375 At L1, the trigger system uses information primarily from the calorimeters
 1376 and muon spectrometer to select high p_T jets, electrons, photons, and muons.
 1377 The electromagnetic calorimeter uses reduced granularity energy measurements
 1378 as well as isolation requirements to select electrons and photons. The hadronic
 1379 calorimeter also uses a combination of reduced granularity energy measurements
 1380 and isolation to select high momentum jets and hadronically decaying tau lept-
 1381 ons. The calorimeters are also used to provide triggers based on missing energy:
 1382 the coarse granularity energy measurements are used to calculate a directional
 1383 sum of energies and to trigger on a significant imbalance. Only the [RPCs](#) and [TGCs](#)
 1384 muon subdetectors contribute to the decision at L1, and are used to identify high
 1385 momentum muons. The contributions to the triggering rate of the various types
 1386 of L1 triggers are shown in Figure 34. The total rate is indicated in black and
 1387 is lower than the sum of individual rates because there is significant overlap be-
 1388 between different trigger channels. The majority of the rate comes from lepton
 1389 and photon triggers.

1390 After an event is chosen by the L1 trigger, the detector measurements from the
 1391 bunch crossing which fired the trigger is read out from the front-end electronics

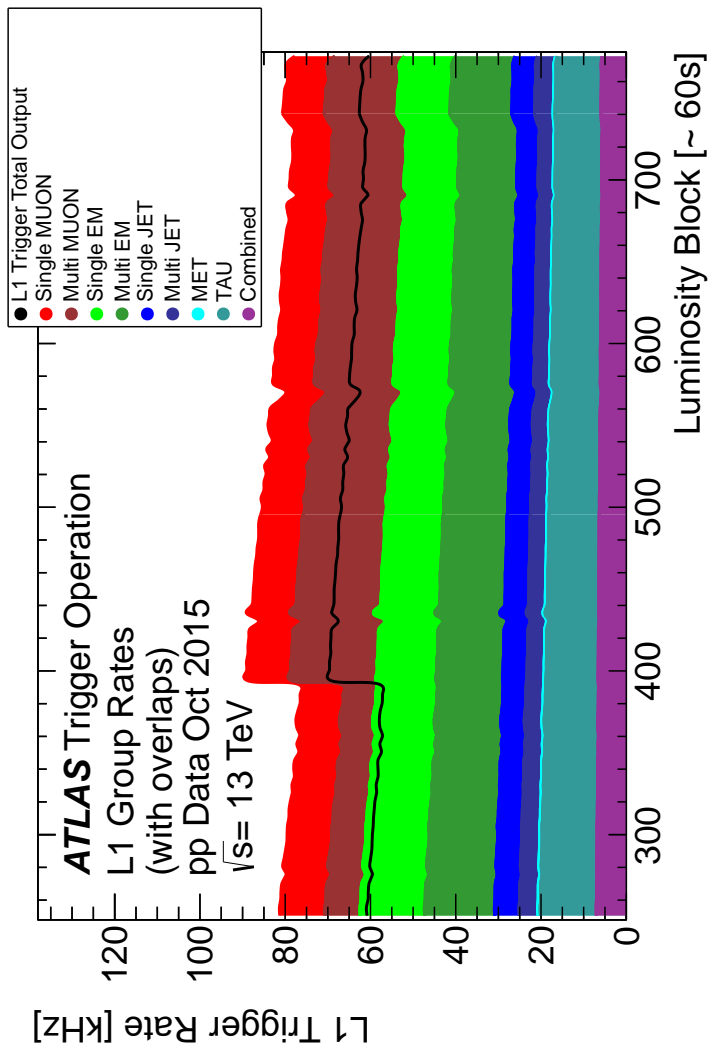


Figure 33: The L1 Trigger rate broken down into the types of triggers as a function of the luminosity block for the 2015 data collection period.

Trigger	Typical offline selection	Trigger Selection		Level-1 Peak Rate (kHz)	HLT Peak Rate (Hz)
		Level-1 (GeV)	HLT (GeV)	$L = 5 \times 10^{33} \text{ cm}^{-2}\text{s}^{-1}$	
Single leptons	Single iso μ , $p_T > 21 \text{ GeV}$	15	20	7	130
	Single e , $p_T > 25 \text{ GeV}$	20	24	18	139
	Single μ , $p_T > 42 \text{ GeV}$	20	40	5	33
	Single τ , $p_T > 90 \text{ GeV}$	60	80	2	41
Two leptons	Two μ 's, each $p_T > 11 \text{ GeV}$	2×10	2×10	0.8	19
	Two μ 's, $p_T > 19, 10 \text{ GeV}$	15	18, 8	7	18
	Two loose e 's, each $p_T > 15 \text{ GeV}$	2×10	2×12	10	5
	One e & one μ , $p_T > 10, 26 \text{ GeV}$	$20 (\mu)$	7, 24	5	1
	One loose e & one μ , $p_T > 19, 15 \text{ GeV}$	15, 10	17, 14	0.4	2
	Two τ 's, $p_T > 40, 30 \text{ GeV}$	20, 12	35, 25	2	22
	One τ , one μ , $p_T > 30, 15 \text{ GeV}$	12, 10 (+jets)	25, 14	0.5	10
	One τ , one e , $p_T > 30, 19 \text{ GeV}$	12, 15 (+jets)	25, 17	1	3.9
	Three loose e 's, $p_T > 19, 11, 11 \text{ GeV}$	15, 2 \times 7	17, 2 \times 9	3	< 0.1
Three leptons	Three μ 's, each $p_T > 8 \text{ GeV}$	3 \times 6	3 \times 6	< 0.1	4
	Three μ 's, $p_T > 19, 2 \times 6 \text{ GeV}$	15	18, 2 \times 4	7	2
	Two μ 's & one e , $p_T > 2 \times 11, 14 \text{ GeV}$	$2 \times 10 (\mu\text{'s})$	$2 \times 10, 12$	0.8	0.2
	Two loose e 's & one μ , $p_T > 2 \times 11, 11 \text{ GeV}$	2 \times 8, 10	2 \times 12, 10	0.3	< 0.1
One photon	one γ , $p_T > 125 \text{ GeV}$	22	120	8	20
Two photons	Two loose γ 's, $p_T > 40, 30 \text{ GeV}$	2×15	35, 25	1.5	12
	Two tight γ 's, $p_T > 25, 25 \text{ GeV}$	2×15	2×20	1.5	7
Single jet	Jet ($R = 0.4$), $p_T > 400 \text{ GeV}$	100	360	0.9	18
	Jet ($R = 1.0$), $p_T > 400 \text{ GeV}$	100	360	0.9	23
E_T^{miss}	$E_T^{\text{miss}} > 180 \text{ GeV}$	50	70	0.7	55
Multi-jets	Four jets, each $p_T > 95 \text{ GeV}$	3 \times 40	4 \times 85	0.3	20
	Five jets, each $p_T > 70 \text{ GeV}$	4 \times 20	5 \times 60	0.4	15
	Six jets, each $p_T > 55 \text{ GeV}$	4 \times 15	6 \times 45	1.0	12
b -jets	One loose b , $p_T > 235 \text{ GeV}$	100	225	0.9	35
	Two medium b 's, $p_T > 160, 60 \text{ GeV}$	100	150, 50	0.9	9
	One b & three jets, each $p_T > 75 \text{ GeV}$	3 \times 25	4 \times 65	0.9	11
	Two b & two jets, each $p_T > 45 \text{ GeV}$	3 \times 25	4 \times 35	0.9	9
b -physics	Two μ 's, $p_T > 6, 4 \text{ GeV}$ plus dedicated b -physics selections	6, 4	6, 4	8	52
Total				70	1400

Table 5: The trigger menu for the 2015 data collection with $L = 5 \times 10^{33} \text{ cm}^{-2}\text{s}^{-1}$. Both the L1 and HLT! selection requirements and their trigger rates are shown measured at the specified luminosity are shown. The typical offline selections represent a typical set of offline requirements imposed after the trigger in an analysis.

and stored on read-out boards. This inclusive information is necessary to make more the more precise event selections than is possible with the reduced information at L1. The HLT! then uses this information with software algorithms to decide whether or not to permanently record the event. The L1 trigger also forwards which decision was made and Region of Interests (RoIs) to the HLT!, which allows the HLT! to focus on particular algorithms and particular sections of the detector to greatly improve the algorithmic selection speed. The additional information available to the HLT! allows it to implement additional trigger targets, such as identified jets from the decays of b -hadrons. The contributions to the triggering rate of the various types of HLT! triggers are shown in Figure 34.

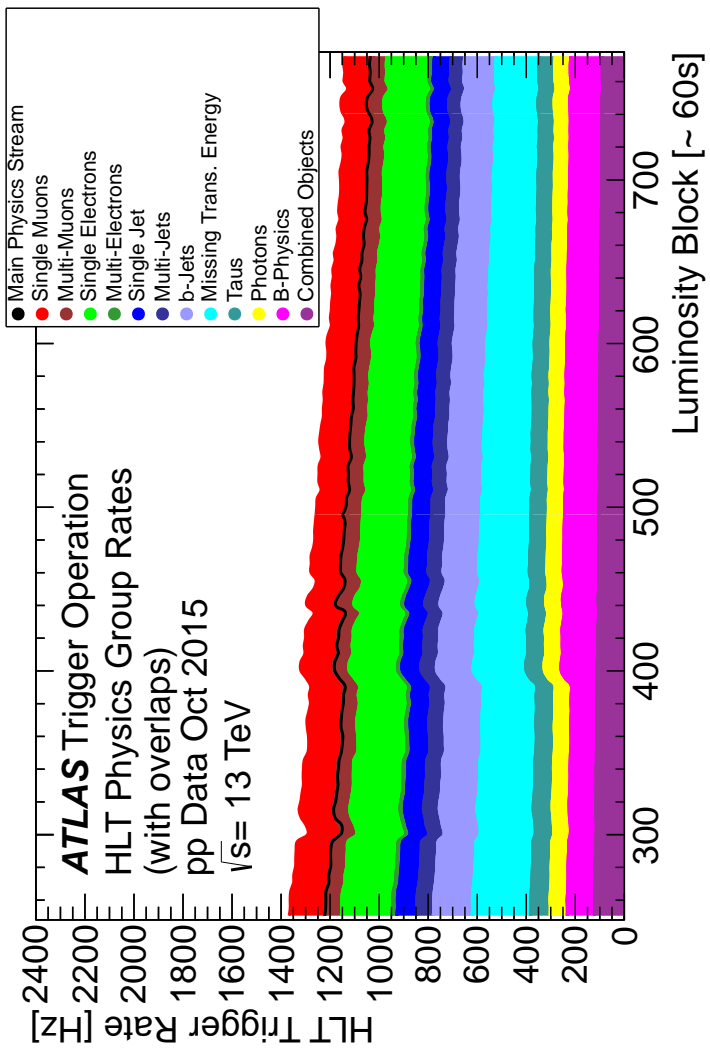


Figure 34: The HLT Trigger rate broken down into the types of triggers as a function of the luminosity block for the 2015 data collection period.

7

1402

1403 EVENT RECONSTRUCTION

1404 The ATLAS experiment combines measurements in the subdetectors to form a
1405 cohesive picture of each physics event.

1406 7.1 TRACKS AND VERTICES

1407 7.1.1 TRACK RECONSTRUCTION

1408 7.1.1.1 NEURAL NETWORK

1409 7.1.1.2 PIXEL DE/DX

1410 7.1.2 VERTEX RECONSTRUCTION

1411 7.2 JETS

1412 7.2.1 TOPOLOGICAL CLUSTERING

1413 7.2.2 JET ENERGY SCALE

1414 7.2.3 JET ENERGY SCALE UNCERTAINTIES

1415 7.2.4 JET ENERGY RESOLUTION

1416 7.3 ELECTRONS

1417 7.3.1 ELECTRON IDENTIFICATION

1418 7.4 MUONS

1419 7.4.1 MUON IDENTIFICATION

1420 7.5 MISSING TRANSVERSE ENERGY

1421

PART IV

1422

CALORIMETER RESPONSE

1423

You can put some informational part preamble text here.

8

1424

1425 RESPONSE MEASUREMENT WITH SINGLE HADRONS

1426 As discussed in Section 7.2, colored particles produced in collisions hadronize
1427 into jets of multiple hadrons. One approach to understanding jet energy mea-
1428 surements in the ATLAS calorimeters is to evaluate the calorimeter response to
1429 those individual hadrons; measurements of individual hadrons can be used to
1430 build up an understanding of the jets that they form. The redundancy of the
1431 momentum provided by the tracking system and the energy provided by the
1432 calorimeter provides an opportunity to study calorimeter response using real
1433 collisions, as described further in Section 8.2.

1434 Calorimeter response includes a number of physical effects that can be ex-
1435 tracted to provide insight into many aspects of jet modeling. First, many charged
1436 hadrons interact with the material of the detector prior to reaching the calorime-
1437 ters and thus do not deposit any energy. Comparing this effect in data and simu-
1438 lation is a powerful tool in validating the interactions of particles with the mate-
1439 rial of the detector and the model of the detector geometry in simulation, see Sec-
1440 tion 8.2.2. The particles which do reach the calorimeter deposit their energy into
1441 several adjacent cells, which are then clustered together. The energy of the clus-
1442 ter is then the total energy deposited by that particle. Comparing the response of
1443 hadrons in data to that of simulated hadrons provides a direct evaluation of the
1444 showering of hadronic particles and the energy deposited by particles in matter
1445 (Section 8.2.4).

1446 The above studies all use an inclusive selection of charged particles, which are
1447 comprised predominantly of pions, kaons, and (anti)protons. It is also possible to
1448 measure the response to various identified particle types separately to evaluate
1449 the simulated interactions of each particle, particularly at low energies where
1450 differences between species are very relevant. Pions and (anti)protons can be
1451 identified through decays of long-lived particles, in particular Λ , $\bar{\Lambda}$, and K_S^0 , and
1452 then used to measure response as described above. This is discussed in detail in
1453 Section 8.3.

1454 The results in this chapter use data collected at 7 and 8 TeV collected in 2010
1455 and 2012, respectively. Both are included as the calorimeter was repaired and
1456 recalibrated between those two data-taking periods. Both sets of data are com-
1457 pared to an updated simulation that includes new physics models provided by
1458 Geant4 [10] and improvements in the detector description [11, 12]. The present
1459 results are published in European Physical Journal C (EPJC) [13] and can be com-
1460 pared to a similar measurement performed in 2009 and 2010 [14], which used
1461 the previous version of the simulation framework [15].

1462 8.1 DATASET AND SIMULATION

1463 8.1.1 DATA SAMPLES

1464 The two datasets used in this chapter are taken from dedicated low-pileup runs
 1465 where the fraction of events with multiple interactions was negligible. These
 1466 datasets are used rather than those containing full-pileup events to facilitate mea-
 1467 surement of isolated hadrons. The 2012 dataset at $\sqrt{s} = 8$ TeV contains 8 mil-
 1468 lion events and corresponds to an integrated luminosity of 0.1 nb^{-1} . The 2010
 1469 dataset at $\sqrt{s} = 7$ TeV contains 3 million events and corresponds to an inte-
 1470 grated luminosity of 3.2 nb^{-1} . The latter dataset was also used for the 2010 re-
 1471 sults [14], but it has since been reanalyzed with an updated reconstruction in-
 1472 cluding the final, best understanding of the detector description for the material
 1473 and alignment from Run 1.

1474 8.1.2 SIMULATED SAMPLES

1475 The two datasets above are compared to simulated single-, double-, and non-
 1476 diffractive events generated with Pythia8 [16] using the A2 configuration of
 1477 hadronization [17] and the MSTW 2008 parton-distribution function set [18,
 1478 19]. The admixture of the single-, double-, and non-diffractive events uses the
 1479 default relative contributions from Pythia8. The conditions and energies for
 1480 the two simulations are chosen so that they match those of the corresponding
 1481 dataset.

1482 To evaluate the interaction of hadrons with detector material, the simulation
 1483 uses two different collections of hadronic physics models, called physics lists, in
 1484 Geant4 9.4 [20]. The first, QGSP_BERT, combines the Bertini intra-nuclear
 1485 cascade [21–23] below 9.9 GeV, a parametrized proton inelastic model from 9.5
 1486 to 25 GeV [24], and a quark-gluon string model above 12 GeV [25–29]. The
 1487 second, FTFP_BERT, combines the Bertini intra-nuclear cascade [21–23] below
 1488 5 GeV and the Fritiof model [30–33] above 4 GeV. In either list, Geant4 en-
 1489 forces a smooth transition between models where multiple models overlap.

1490 8.1.3 EVENT SELECTION

1491 The event selection for this study is minimal, as the only requirement is selecting
 1492 good-quality events with an isolated track. Such events are triggered by requir-
 1493 ing at least two hits in the minimum-bias trigger scintillators. After trigger, each
 1494 event is required to have exactly one reconstructed vertex, and that vertex is re-
 1495 quired to have four or more associated tracks.

1496 The particles which are selected for the response measurements are first iden-
 1497 tified as tracks in the inner detector. The tracks are required to have at least 500
 1498 MeV of transverse momentum. To ensure a reliable momentum measurement,
 1499 these tracks are required to have at least one hit in the pixel detector, six hits in
 1500 the SCT, and small longitudinal and transverse impact parameters with respect
 1501 to the primary vertex [14]. For the majority of the measurements in this chapter,

1502 the track is additionally required to have 20 hits in the TRT, which significantly
 1503 reduces the contribution from tracks which undergo nuclear interactions. This
 1504 requirement and its effect is discussed in more detail in Section 8.2.5. In addition,
 1505 tracks are rejected if there is any other reconstructed track which extrapolates
 1506 to the calorimeter within a cone of $\Delta R = \sqrt{(\Delta\phi)^2 + (\Delta\eta)^2} < 0.4$. This require-
 1507 ment guarantees that the contamination of energy from nearby charged particles
 1508 is negligible [14].

1509 8.2 INCLUSIVE HADRON RESPONSE

1510 The calorimeter response is more precisely defined as the ratio of the measured
 1511 calorimeter energy to the true energy carried by the particle, although this true
 1512 energy is unknown. For charged particles, however, the inner detector provides
 1513 a very precise measurement of momentum (with uncertainty less than 1%) that
 1514 can be used as a proxy for true energy. The ratio of the energy deposited by
 1515 the charged particle in the calorimeter, E , to its momentum measured in the
 1516 inner detector p , forms the calorimeter response measure called E/p . Though
 1517 the distribution of E/p contains a number of physical features, this study focuses
 1518 on the trends in two aggregated quantities: $\langle E/p \rangle$, the average of E/p for the
 1519 selected tracks, and the zero fraction, the fraction of tracks with no associated
 1520 energy in the calorimeter for those tracks.

1521 The calorimeter energy assigned to a track is defined using clusters. The clus-
 1522 ters are formed using a 4–2–0 algorithm [34] that begins with seeds requiring
 1523 at least 4 times the average calorimeter cell noise. The neighboring cells with
 1524 at least twice that noise threshold are then added to the cluster, and all bound-
 1525 ing cells are then added with no requirement. This algorithm minimizes noise
 1526 contributions through its seeding process, and including the bounding cells im-
 1527 proves the energy resolution [35]. The clusters are associated to a given track
 1528 if they fall within a cone of $\Delta R = 0.2$ of the extrapolated position of the track,
 1529 which includes about 90% of the energy on average [14]. This construction is
 1530 illustrated in Figure 35.

1531 8.2.1 E/P DISTRIBUTION

1532 The E/p distributions measured in both data and simulation are shown in Fig-
 1533 ure 36 for two example bins of track momentum and for tracks in the central
 1534 region of the detector. These distributions show several important features of
 1535 the E/p observable. The large content in the bin at $E = 0$ comes from tracks that
 1536 have no associated cluster, which occurs due to interactions with detector mate-
 1537 rial prior to reaching the calorimeter or the energy deposit being insufficiently
 1538 large to generate a seed, and are discussed in Section 8.2.2. The small negative
 1539 tail also comes from tracks that do not deposit any energy in the calorimeter but
 1540 are randomly associated to a cluster with an energy below the noise threshold.
 1541 The long positive tail above 1.0 comes from the contribution of neutral parti-
 1542 cles. Nearby neutral particles deposit (sometimes large) additional energy in the
 1543 calorimeter but do not produce tracks in the inner detector, so they cannot be

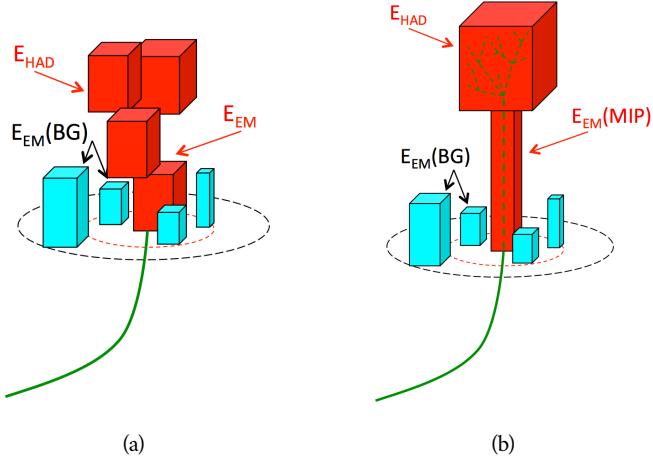


Figure 35: An illustration (a) of the E/p variable used throughout this paper. The red energy deposits come from the charged particle targeted for measurement, while the blue energy deposits are from nearby neutral particles and must be subtracted. The same diagram (b) for the neutral-background selection, described in Section 8.2.3.

1544 rejected by the track isolation requirement. Additionally the peak and mean of
1545 the distribution falls below 1.0 because of the loss of energy not found within
1546 the cone as well as the non-compensation of the calorimeter.

1547 The data and simulation share the same features, but the high and low tails
1548 are significantly different. The simulated events tend to overestimate the con-
1549 tribution of neutral particles to the long tail, an effect which can be isolated and
1550 removed as discussed in Section 8.2.3. Additionally, the simulated clusters have
1551 less noise on average, although this is a small effect on the overall response.

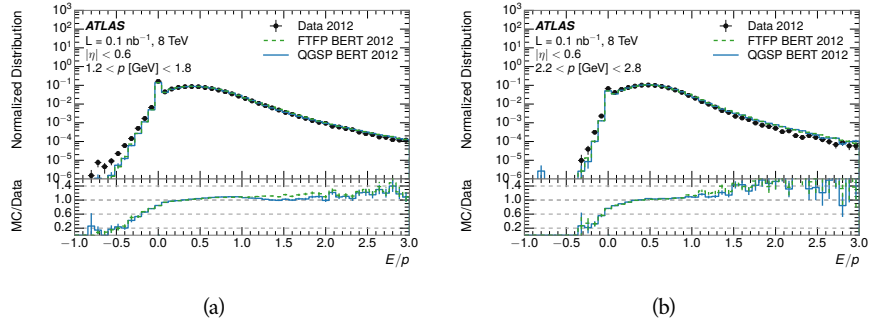


Figure 36: The E/p distribution and ratio of simulation to data for isolated tracks with (a) $|\eta| < 0.6$ and $1.2 < p/\text{GeV} < 1.8$ and (b) $|\eta| < 0.6$ and $2.2 < p/\text{GeV} < 2.8$.

1552 8.2.2 ZERO FRACTION

1553 The fraction of particles with no associated clusters, or similarly those with $E \leq$
1554 0, reflects the modeling of both the detector geometry and hadronic interactions.

1555 The zero fraction is expected to rise as the amount of material a particle traverses
 1556 increases, while it is expected to decrease as the particle energy increases. This
 1557 dependence can be seen in Figure 37, where the zero fraction in data and simulation
 1558 is shown as a function of momentum and the amount of material measured
 1559 in interaction lengths. The trends are similar between 2010 and 2012 and for
 1560 positively and negatively charged particles. The zero fraction decreases with
 1561 energy as expected. The absolute discrepancy in zero fraction decreases with
 1562 momentum from 5% to less than 1%, but this becomes more pronounced in the
 1563 ratio as the zero fraction shrinks quickly with increasing momentum. There is
 1564 a small constant difference between the data and simulation in both interaction
 1565 models that becomes more pronounced. The amount of material in the detector
 1566 increases with η , which is used to obtain results for interaction lengths ranging
 1567 between 0.1 and 0.65 λ . As the data and simulation have significant disagree-
 1568 ment in the zero fraction over a number of interaction lengths, the difference
 1569 must be primarily from the modeling of hadronic interactions with detector ma-
 1570 terial and not just the detector geometry. Although two different hadronic in-
 1571 teraction models are shown in the figure, they have very similar discrepancies to
 1572 data because both use the same description (the BERT model) at low momentum.

1573 8.2.3 NEUTRAL BACKGROUND SUBTRACTION

1574 The isolation requirement on hadrons is only effective in removing an energy
 1575 contribution from nearby charged particles. Nearby neutral particles, predomi-
 1576 nantly photons from π^0 decays, also add their energy to the calorimeter clusters,
 1577 but mostly in the electromagnetic calorimeter. It is possible to measure this con-
 1578 tribution, on average, using late-showering hadrons that minimally ionize in the
 1579 electromagnetic calorimeter. Such particles are selected by requiring that they
 1580 deposit less than 1.1 GeV in the EM calorimeter within a cone of $\Delta R < 0.1$
 1581 around the track. To ensure that these particles are well measured, they are addi-
 1582 tionally required to deposit between 40% and 90% of their energy in the hadronic
 1583 calorimeter within the same cone.

1584 These particles provide a clean sample to measure the nearby neutral back-
 1585 ground because they do not deposit energy in the area immediately surrounding
 1586 them in the EM calorimeter, as shown in Figure 35. So, the energy deposits in the
 1587 region $0.1 < \Delta R < 0.2$ can be attributed to neutral particles alone. To estimate
 1588 the contribution to the whole cone considered for the response measurement,
 1589 that energy is scaled by a geometric factor of 4/3. This quantity, $\langle E/p \rangle_{BG}$, mea-
 1590 sured in aggregate over a number of particles, gives the contribution to $\langle E/p \rangle$
 1591 from neutral particles in the EM calorimeter. Similar techniques were used in
 1592 the individual layers of the hadronic calorimeters to show that the background
 1593 from neutrals is negligible in those layers [14].

1594 The distribution of this background estimate is shown in Figure 38 for data
 1595 and simulation with the two different physics lists. The contribution from neu-
 1596 tral particles falls from 0.1 at low momentum to around 0.03 for particles above
 1597 7 GeV. Although the simulation captures the overall trend, it significantly over-
 1598 estimates the neutral contribution for tracks with momentum between 2 and 8

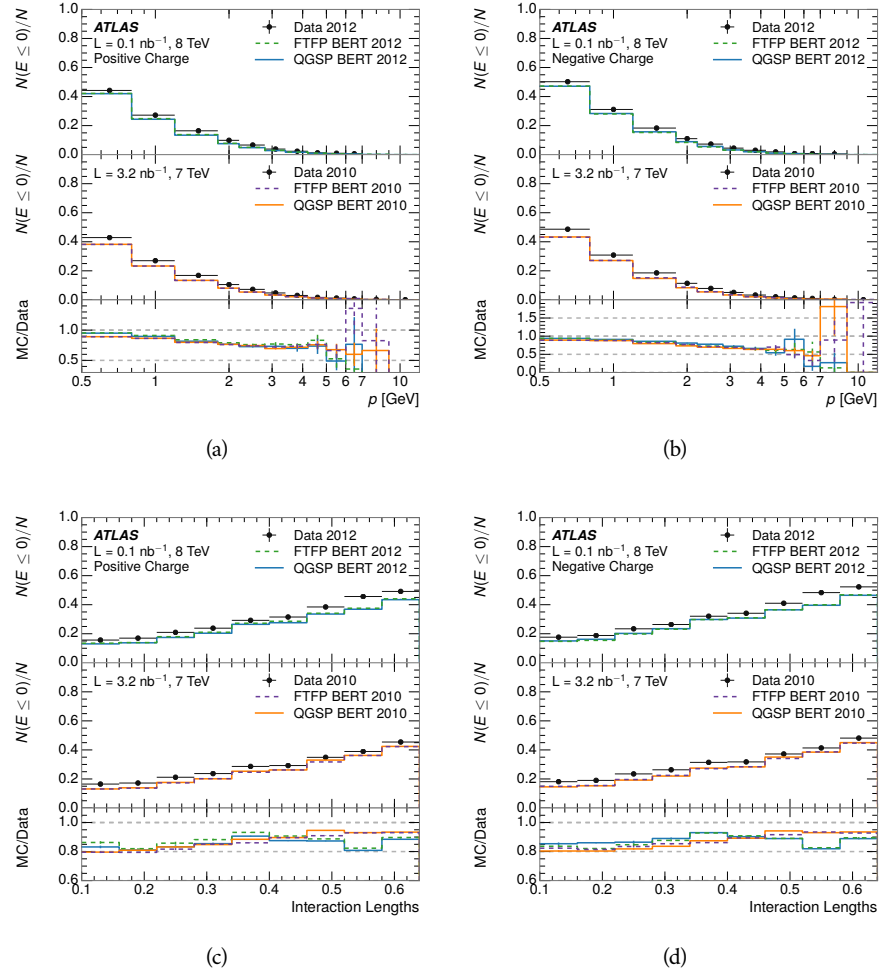


Figure 37: The fraction of tracks as a function (a, b) of momentum, (c, d) of interaction lengths with $E \leq 0$ for tracks with positive (on the left) and negative (on the right) charge.

1599 GeV. This effect was also seen in the tails of the E/p distributions in Figure 36.
 1600 This difference is likely due to modeling of coherent neutral particle radiation
 1601 in Pythia8 that overestimates the production of π^0 near the production of the
 1602 charged particles. The discrepancy does not depend on η and thus is unlikely to
 1603 be a mismodeling of the detector. This difference can be subtracted to form a
 1604 corrected average E/p , as in Section 8.2.4.

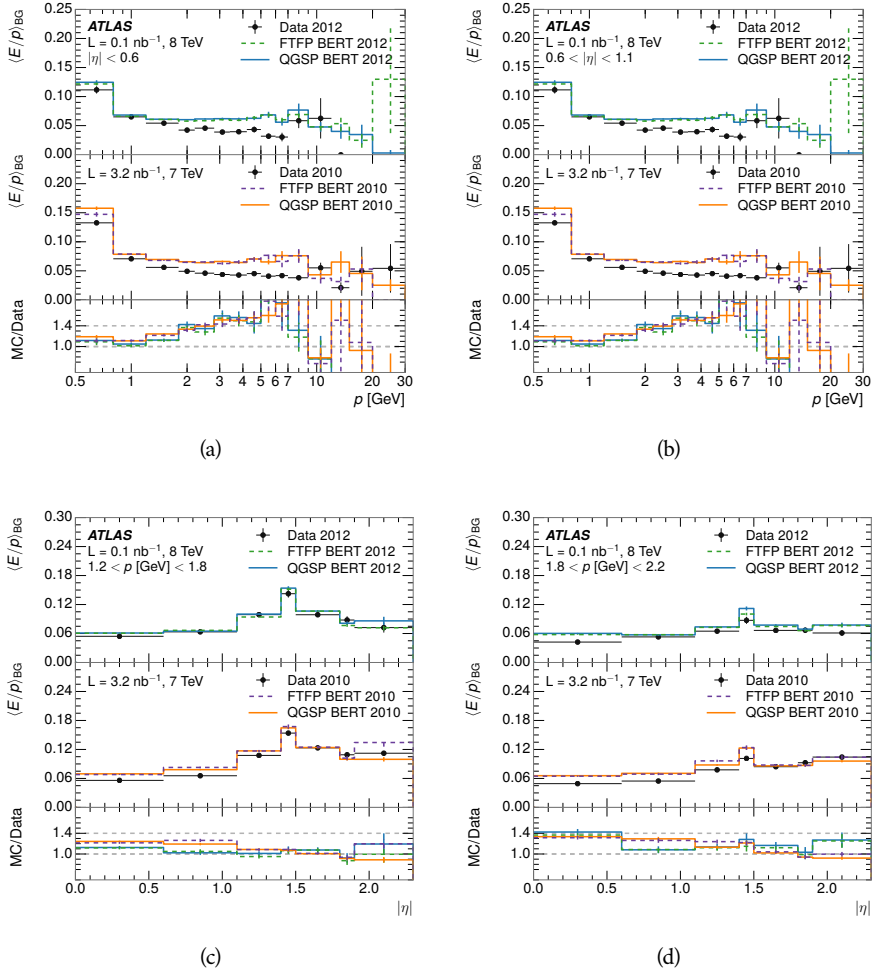


Figure 38: $\langle E/p \rangle_{BG}$ as a function of the track momentum for tracks with (a) $|\eta| < 0.6$,
 (b) $0.6 < |\eta| < 1.1$, and as a function of the track pseudorapidity for tracks
 with (c) $1.2 < p/\text{GeV} < 1.8$, (d) $1.8 < p/\text{GeV} < 2.2$.

1605 8.2.4 CORRECTED RESPONSE

1606 Figure 39 shows $\langle E/p \rangle_{COR}$ as a function of momentum for several bins of pseudo-
 1607 rapidity. This corrected $\langle E/p \rangle_{COR} \equiv \langle E/p \rangle - \langle E/p \rangle_{BG}$ measures the average
 1608 calorimeter response without the contamination of neutral particles. It is the
 1609 most direct measurement of calorimeter response in that it is the energy mea-
 1610 sured for fully isolated hadrons. The correction is performed separately in data
 1611 and simulation, so that the mismodeling of the neutral background in simulation

1612 is removed from the comparison of response. The simulation overestimates the
 1613 response at low momentum by about 5%, an effect that can be mostly attributed
 1614 to the underestimation of the zero fraction mentioned previously. For $|\eta| < 0.6$,
 1615 the data-simulation agreement has a larger discrepancy by about 5% for 2010
 1616 than 2012, although this is not reproduced in at higher pseudorapidity.

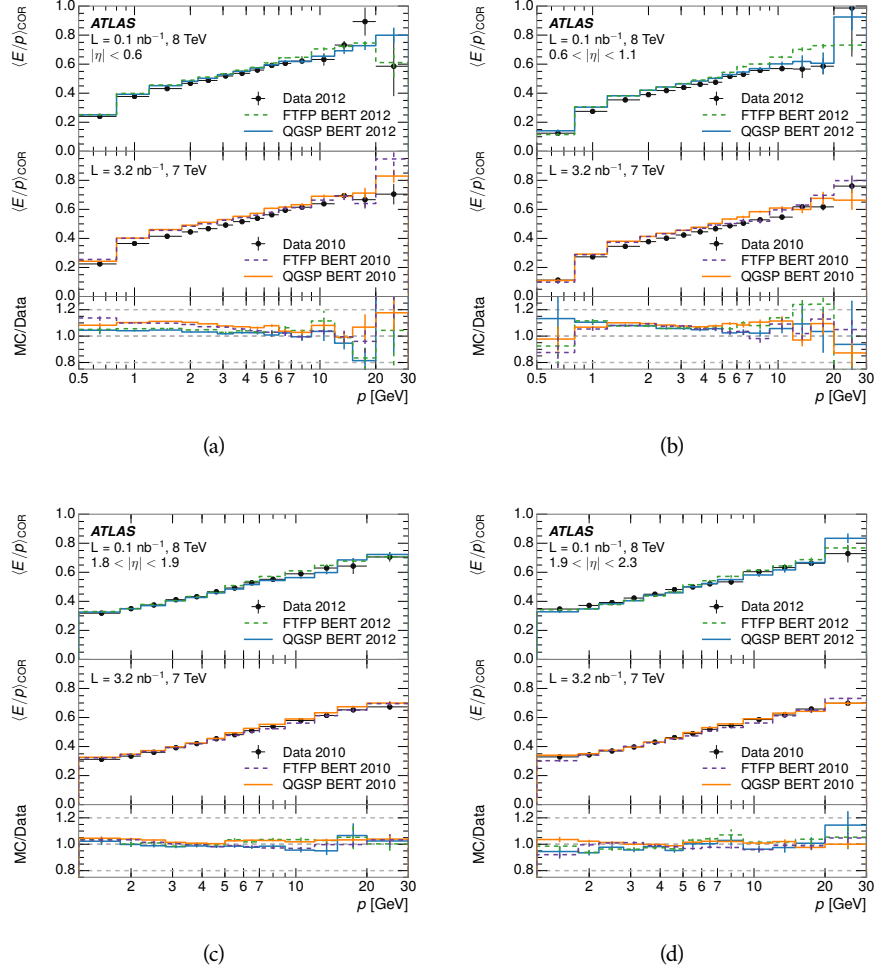


Figure 39: $\langle E/p \rangle_{\text{COR}}$ as a function of track momentum, for tracks with (a) $|\eta| < 0.6$, (b) $0.6 < |\eta| < 1.1$, (c) $1.8 < |\eta| < 1.9$, and (d) $1.9 < |\eta| < 2.3$.

1617 The response measurement above used topological clustering at the EM scale,
 1618 that is clusters were formed to measure energy but no corrections were applied
 1619 to correct for expected effects like energy lost outside of the cluster or in unin-
 1620 strumented material. It is also interesting to measure $\langle E/p \rangle_{\text{COR}}$ using local clus-
 1621 ter weighted (LCW) energies, which accounts for those effects by calibrating the
 1622 energy based on the properties of the cluster such as energy density and depth
 1623 in the calorimeter. Figure 40 shows these distributions for tracks with zero or
 1624 more clusters and separately for tracks with one or more clusters. The calibra-
 1625 tion moves the mean value of $\langle E/p \rangle_{\text{COR}}$ significantly closer to 1.0 as desired.
 1626 The agreement between data and simulation improves noticeably when at least
 1627 one cluster is required, as this removes the contribution from the mismodeling of

the zero fraction. The good agreement in that case again demonstrates that the difference in $\langle E/p \rangle_{\text{COR}}$ between data and simulation is caused predominantly by the difference in zero fraction.

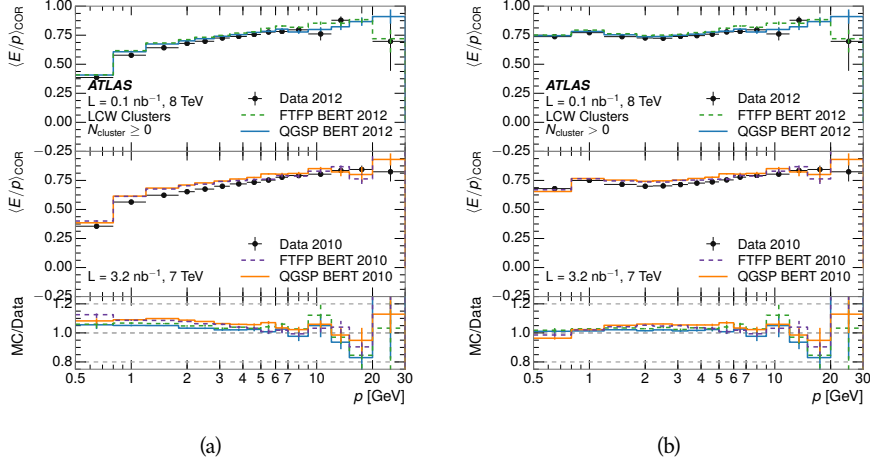


Figure 40: $\langle E/p \rangle_{\text{COR}}$ calculated using LCW-calibrated topological clusters as a function of track momentum for tracks with (a) zero or more associated topological clusters or (b) one or more associated topological clusters.

8.2.5 ADDITIONAL STUDIES

As has been seen in several measurements in previous sections, the simulation does not correctly model the chance of a low momentum hadron to reach the calorimeter. Because of the consistent discrepancy across pseudorapidity and interaction lengths, this can be best explained by incomplete understanding of hadronic interactions with the detector [13]. For example, a hadron that scatters off of a nucleus in the inner detector can be deflected through a significant angle and not reach the expected location in the calorimeter. In addition, these interactions can produce secondary particles that are difficult to model.

The requirement used throughout the previous sections on the number of hits in the TRT reduces these effects by preferentially selecting tracks that do not undergo nuclear interactions. It is interesting to check how well the simulation models tracks with low numbers of TRT hits, which selects tracks that are more likely to have undergone a hadronic interaction. Figure 41 compares the distributions with $N_{\text{TRT}} < 20$ to $N_{\text{TRT}} > 20$ for real and simulated particles. As expected, the tracks with fewer hits are poorly modeled in the simulation as $\langle E/p \rangle_{\text{COR}}$ differs by as much as 25% at low momentum.

Another interesting aspect of the simulation is the description of antiprotons at low momentum, where QGSP_BERT and FTFP_BERT have significant differences. This can be seen to have an effect in the inclusive response measurement when separated into positive and negative charge. The $\langle E/p \rangle_{\text{COR}}$ distributions for positive and negative particles are shown in Figure 42, where a small difference between QGSP_BERT and FTFP_BERT can be seen in the distribution for

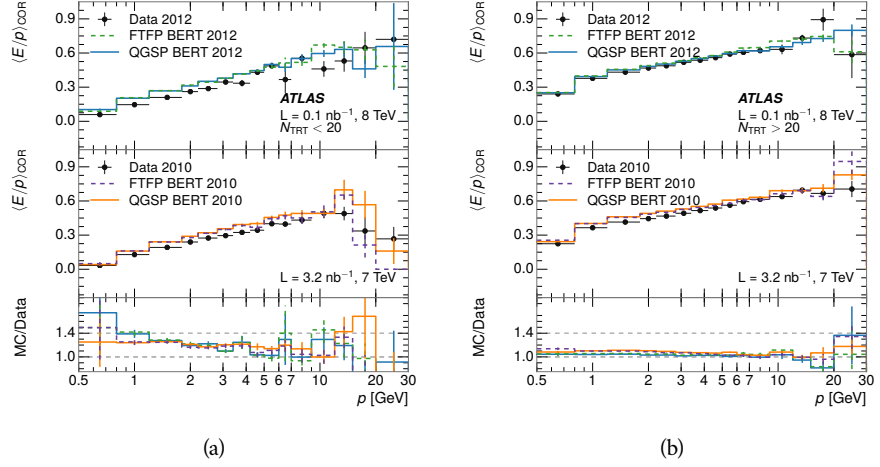


Figure 41: Comparison of the $\langle E/p \rangle_{\text{COR}}$ for tracks with (a) less than and (b) greater than 20 hits in the TRT.

negative tracks. This is demonstrated more clearly in Figure 43, which shows the E/p distribution in the two simulations separated by charge. There is a clear difference around $E/p > 1.0$, which can be explained by the additional energy deposited by the annihilation of the antiproton in the calorimeter that is modeled well only in FTFP_BERT. This is also explored with data using identified antiprotons in Section 8.3.

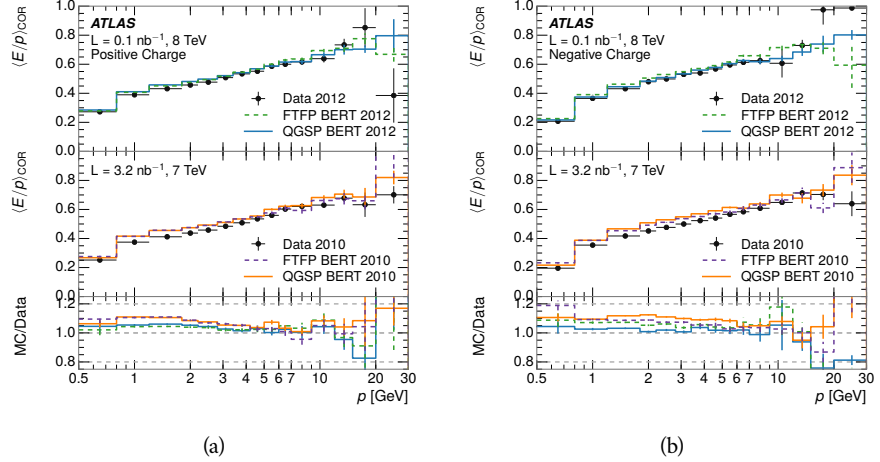


Figure 42: Comparison of the $\langle E/p \rangle_{\text{COR}}$ for (a) positive and (b) negative tracks as a function of track momentum for tracks with $|\eta| < 0.6$.

The $\langle E/p \rangle$ results in previous sections have considered the electromagnetic and hadronic calorimeters together as a single energy measurement, to emphasize the total energy deposited for a given particle. However, the deposits in each calorimeter are available separately and $\langle E/p \rangle$ can be constructed for each layer. As the layers are composed of different materials and are modeled separately in the detector geometry, confirmation that the simulation matches the data well

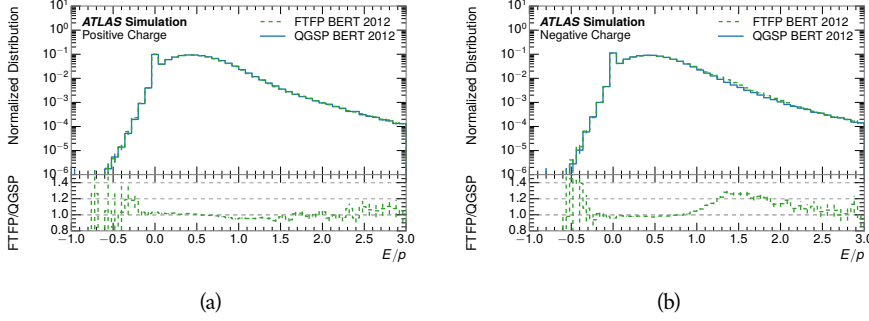


Figure 43: Comparison of the E/p distributions for (a) positive and (b) negative tracks with $0.8 < p/\text{GeV} < 1.2$ and $|\eta| < 0.6$, in simulation with the FTFP_BERT and QGSP_BERT physics lists.

in each layer adds confidence in both the description of hadronic interactions with the two different materials and also the geometric description of each.

The technique discussed in Section 8.2.3 for selecting MIPs in the electromagnetic calorimeter is also useful in studying deposits in the hadronic calorimeter. Those MIPs deposit almost all of their energy exclusively in the hadronic calorimeter. Figure 44 shows $\langle E/p \rangle_{\text{RAW}}^{\text{Had}}$, where RAW indicates that no correction has been applied for neutral backgrounds and Had indicates that only clusters for the hadronic calorimeter are included. The RAW and COR versions of $\langle E/p \rangle$ in this case are the same, as the neutral background is negligible in that calorimeter layer. The distributions are shown both for the original EM scale calibration and after LCW calibration. The data and simulation agree very well in this comparison, except in the lowest momentum bin which has 5% discrepancy that has already been seen in similar measurements.

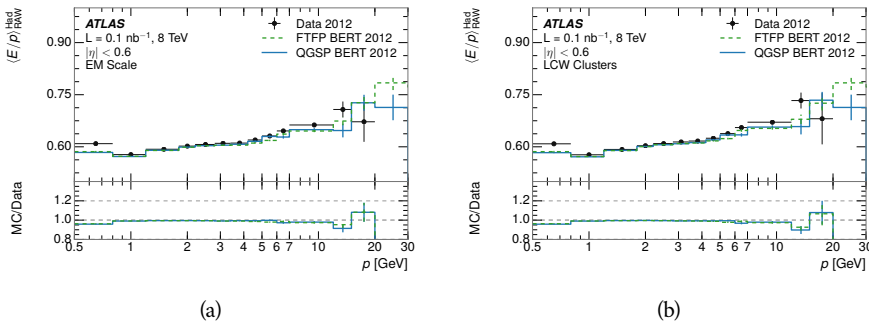


Figure 44: Comparison of the response of the hadronic calorimeter as a function of track momentum (a) at the EM-scale and (b) after the LCW calibration.

A similar comparison can be made in the electromagnetic calorimeter by selecting particles which have no associated energy in the hadronic calorimeter. These results are measured in terms of $\langle E/p \rangle_{\text{COR}}^{\text{EM}}$, where EM designates that only clusters in the electromagnetic calorimeter are included and COR designates that the neutral background is subtracted as the neutral background is present in this case. Figure 45 shows the analogous comparisons to Figure 44 in

1685 the electromagnetic calorimeter. In this case the disagreement between data and
 1686 simulation is more pronounced, with discrepancies as high as 5% over a larger
 1687 range of momenta. This level of discrepancy indicates that the description of
 1688 the electromagnetic calorimeter is actually the dominant source of discrepancy
 1689 in the combined distributions in Section 8.2.4.

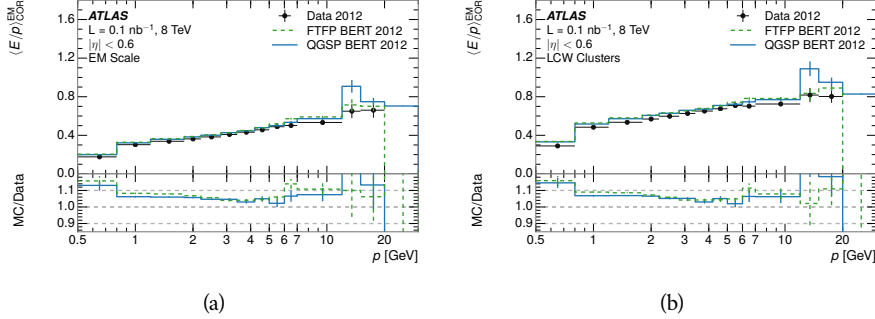


Figure 45: Comparison of the response of the EM calorimeter as a function of track momentum (a) at the EM-scale and (b) with the LCW calibration.

1690 **NOTE: There are more studies that I skipped for brevity that could be in-**
 1691 **cluded if interesting. E/p at different cluster threshold settings, E/p with**
 1692 **pileup, E/p with cells. I also left out a lot of eta bins that appear in the**
 1693 **paper so that this section didn't turn into 20 pages of plots.**

1694 8.3 IDENTIFIED PARTICLE RESPONSE

1695 The inclusive response measurement for hadrons can be augmented by measur-
 1696 ing the response for specific particle species. The simulation models each parti-
 1697 cle type separately, and understanding the properties of each is important in con-
 1698 straining the uncertainty on jets. In order to select and measure specific hadrons,
 1699 this section relies on the displaced decays of long-lived particles. Such decays
 1700 can be identified by reconstructing secondary vertices with a requirement on
 1701 mass. In particular, Λ , $\bar{\Lambda}$, and K_S^0 can be used to select a pure sample of protons,
 1702 antiprotons, and pions, respectively.

1703 8.3.1 DECAY RECONSTRUCTION

1704 The measurement of response for identified particles uses the same selection as
 1705 for inclusive particles (Section 8.1.3) with a few additions. Each event used is
 1706 required to have at least one secondary vertex, and the tracks are required to
 1707 match to that vertex rather than the primary vertex. Pions are selected from
 1708 decays of $K_S^0 \rightarrow \pi^+ \pi^-$, which is the dominant decay for K_S^0 to charged particles.
 1709 Protons are selected from decays of $\Lambda \rightarrow \pi^- p$ and antiprotons from $\bar{\Lambda} \rightarrow \pi^+ \bar{p}$,
 1710 which are similarly the dominant decays of Λ and $\bar{\Lambda}$ to charged particles. The
 1711 species of parent hadron in these decays is determined by reconstructing the
 1712 mass of the tracks associated to the secondary vertex. The sign of the higher

momentum decay particle can distinguish between Λ and $\bar{\Lambda}$, which of course have the same mass, as the proton or antiproton is kinematically favored to have higher momentum. Examples of the reconstructed masses used to select these decays are shown in Figure 46.

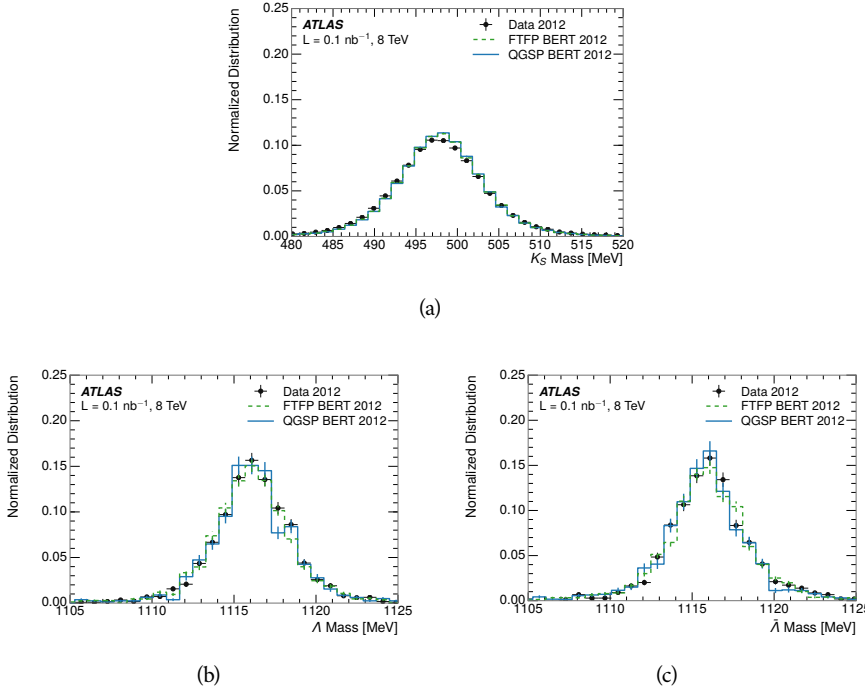


Figure 46: The reconstructed mass peaks of (a) K_S^0 , (b) Λ , and (c) $\bar{\Lambda}$ candidates.

The dominant backgrounds for the identified particle decays are nuclear interactions and combinatoric sources. These are suppressed by the kinematic requirements on the tracks as well as an additional veto which removes candidates that are consistent with both a Λ or $\bar{\Lambda}$ and a K_S^0 hypothesis, which is possible because of the different assumptions on particle mass in each case [14]. After these requirements, the backgrounds are found to be negligible compared to the statistical errors on these measurements.

8.3.2 IDENTIFIED RESPONSE

With these techniques the E/p distributions are extracted in data and simulation for each particle species and shown in Figure 47. These distributions are shown for a particular bin of E_a ($2.2 < E_a/\text{GeV} < 2.8$), rather than p . E_a is the energy available to be deposited in the calorimeter: for pions $E_a = \sqrt{p^2 + m^2}$, for protons $E_a = \sqrt{p^2 + m^2} - m$, and for antiprotons $E_a = \sqrt{p^2 + m^2} + m$. The features of the E/p distributions are similar to the inclusive case. There is a small negative tail from noise and a large fraction of tracks with zero energy from particles which do not reach the calorimeter. The long positive tail is noticeably more pronounced for antiprotons because of the additional energy generated by the annihilation in addition to the neutral background.

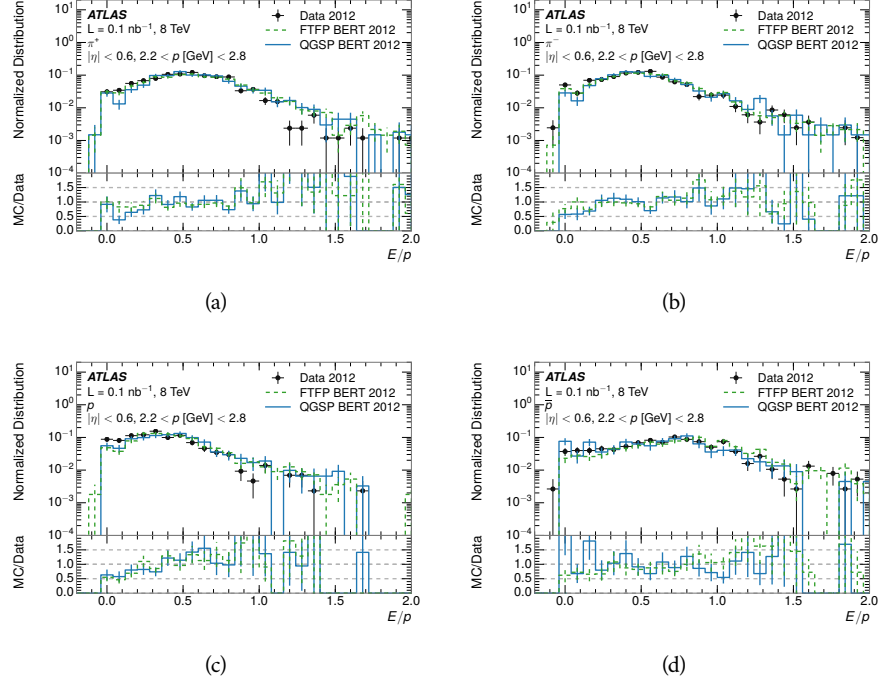


Figure 47: The E/p distribution for isolated (a) π^+ , (b) π^- , (c) proton, and (d) anti-proton tracks.

1735 The zero fraction is further explored in Figure 48 for pions and protons in data
 1736 and simulation. The simulation consistently underestimates the zero fraction
 1737 independent of particle species, which implies that this discrepancy is not caused
 1738 by the model of a particular species but rather a feature common to all.

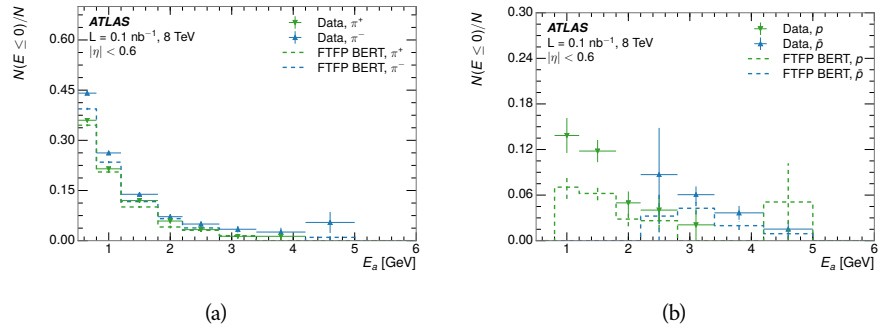


Figure 48: The fraction of tracks with $E \leq 0$ for identified (a) π^+ and π^- , and (b) proton and anti-proton tracks

1739 It is also interesting to compare the response between the different particle
 1740 species. One approach to do this is to measure the difference in $\langle E/p \rangle$ between
 1741 two types, which has the advantage of removing the neutral background. These
 1742 differences are shown in various combinations in Figure 49. The response for
 1743 π^+ is greater on average than the response to π^- because of a charge-exchange
 1744 effect which causes the production of additional neutral pions in the showers of

1745 π^+ [36]. The response for π^+ is also greater on average than the response to p ,
 1746 because a large fraction of the energy of π^+ hadrons is converted to an electro-
 1747 magnetic shower [37, 38]. However, the \bar{p} response is significantly higher than
 1748 the response to π^- because of the annihilation of the antiproton. FTFP_BERT
 1749 does a better job of modeling this effect than QGSP_BERT because of their differ-
 1750 ent descriptions of \bar{p} interactions with material.

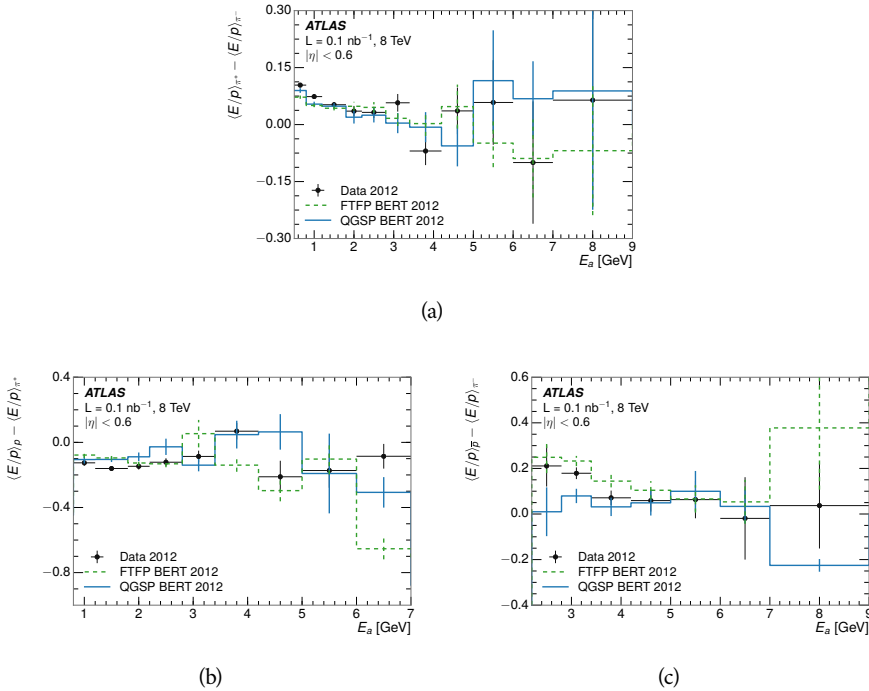


Figure 49: The difference in $\langle E/p \rangle$ between (a) π^+ and π^- (b) p and π^+ , and (c) \bar{p} and π^- .

1751 It is also possible to remove the neutral background from these response dis-
 1752 tributions using the same technique as in Section 8.2.3. The technique is largely
 1753 independent of the particle species and so can be directly applied to $\langle E/p \rangle$ for
 1754 pions. The $\langle E/p \rangle_{\text{COR}}$ distributions for pions are shown in Figure 50, which are
 1755 very similar to the inclusive results. The inclusive hadrons are comprised mostly
 1756 of pions, so this similarity is not surprising. It is also possible to see the small
 1757 differences between π^+ and π^- response here, where $\langle E/p \rangle_{\text{COR}}$ is higher on av-
 1758 erage for π^+ . The agreement between data and simulation is significantly worse
 1759 for the π^- distributions than for the π^+ , with a discrepancy greater than 10%
 1760 below 2-3 GeV.

1761 8.3.3 ADDITIONAL SPECIES IN SIMULATION

1762 The techniques above provide a method to measure the response separately for
 1763 only pions and protons. However the hadrons which forms jets include a num-
 1764 ber of additional species such as kaons and neutrons. The charged kaons are
 1765 an important component of the inclusive charged hadron distribution, which is
 1766 comprised of roughly 60-70% pions, 15-20% kaons, and 5-15% protons. These

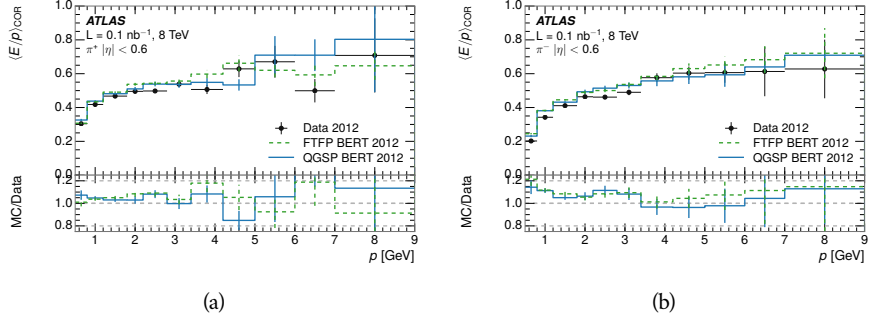


Figure 50: $\langle E/p \rangle_{\text{COR}}$ as a function of track momentum for (a) π^+ tracks and (b) π^- tracks.

1767 are difficult to measure in data at the ATLAS detector, although a template sub-
 1768 traction technique has been proposed which may be effective with larger sample sizes [13]. The simulation of these particles includes noticeable differences in
 1769 response at low energies, which are shown in Figure 51 for FTFP_BERT. The
 1770 significant differences in response between low energy protons and antiprotons
 1771 are accounted for above in the definitions of E_a .
 1772

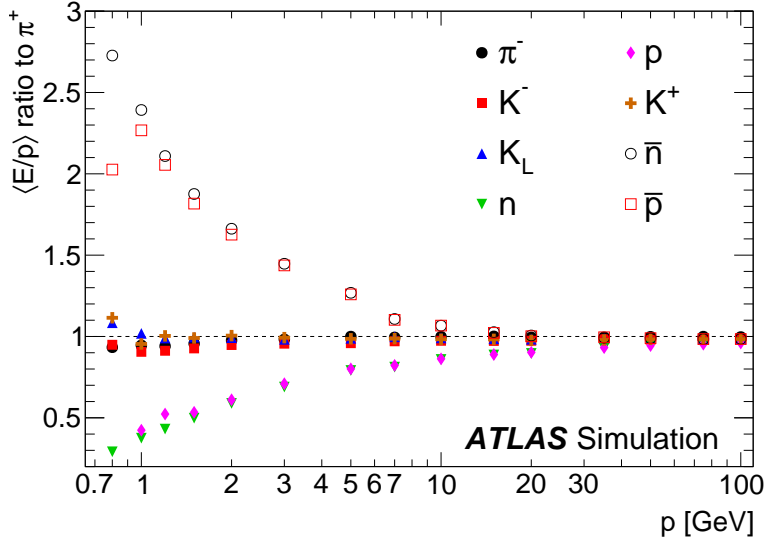


Figure 51: The ratio of the calorimeter response to single particles of various species to the calorimeter response to π^+ with the physics list FTFP_BERT.

1773 8.4 SUMMARY

1774 These various measurements of calorimeter response shown above for data and
 1775 simulation illuminate the accuracy of the simulation of hadronic interactions at
 1776 the ATLAS detector. The results were done using 2010 and 2012 data at 7 and 8
 1777 TeV, but reflect the most current understanding of the detector alignment and
 1778 geometry. A number of measurements focusing on a comparison between pro-

1779 tons and antiprotons suggest that FTFP_BERT models those interaction more
1780 accurately than QGSP_BERT. These measurements, among others, were the moti-
1781 vation to switch the default Geant4 simulation from FTFP_BERT to QGSP_BERT
1782 for all ATLAS samples.

1783 Even with these updates, there are a number of small, approximately 5%, dis-
1784 crepancies in response between the data and simulation at low energies. At
1785 higher energies the simulation of hadronic interactions is very consistent with
1786 data. Chapter 9 discusses how to use these observed differences to constrain the
1787 jet energy scale and its associated uncertainties.

1788

1789 JET ENERGY RESPONSE AND UNCERTAINTY

1790 9.1 MOTIVATION

1791 As jets form a major component of many physics analyses at ATLAS, it is crucial
 1792 to carefully calibrate the measurement of jet energies and to derive an uncer-
 1793 tainty on that measurement. These uncertainties have often been the dominant
 1794 systematic uncertainty in high-energy analyses at the LHC. Dijet and multijet
 1795 balance techniques provide a method to constrain the JES and its uncertainty in
 1796 data, and provide the default values used for ATLAS jet measurements at most
 1797 energies [39]. These techniques are limited by their reliance on measuring jets
 1798 in data, so they are statistically limited in estimating the jet energy scale at the
 1799 highest jet energies. This chapter presents another method for estimating the jet
 1800 energy scale and its uncertainty which builds up a jet from its components and
 1801 thus can be naturally extended to high jet momentum. Throughout this chapter
 1802 the jets studied are simulated using Pythia8 with the CT10 parton distribution
 1803 set [40] and the AU2 tune [17], and corrections are taken from the studies includ-
 1804 ing data and simulation in Chapter 8.

1805 As described in Section 7.2, jets are formed from topological clusters of energy
 1806 in the calorimeters using the anti- k_t algorithm. These clusters originate from a
 1807 diverse spectrum of particles, in terms of both species and momentum, leading to
 1808 significantly varied jet properties and response between jets of similar produced
 1809 momentum. Figure 52 shows the simulated distribution of particles within jets
 1810 at a few examples energies. The E/p measurements provide a thorough under-
 1811 standing of the dominant particle content of jets, the charged hadrons.

1812 9.2 UNCERTAINTY ESTIMATE

1813 Simulated jets are not necessarily expected to correctly model the energy de-
 1814 posits in the calorimeters, because of the various discrepancies discussed in Chap-
 1815 ter 8. To evaluate a jet energy response, the simulated jet energies are compared
 1816 to a corrected jet built up at the particle level. Each cluster in a jet is associated
 1817 to the truth particle which deposited it, and the energy in that cluster is then
 1818 corrected for a number of effects based on measurements in data. The primary
 1819 corrections come from the single hadron response measurements in addition to
 1820 response measured using the combined test beam which covers higher momen-
 1821 tum particles [41]. These corrections include both a shift (Δ), in order to make
 1822 the simulation match the average response in data, and an uncertainty (σ) asso-
 1823 ciated with the ability to constrain the difference between data and simulation.
 1824 Some of the dominant sources of uncertainty are itemized in Table 6 with typi-
 1825 cal values, and the full list considered is described in detail in the associated pa-

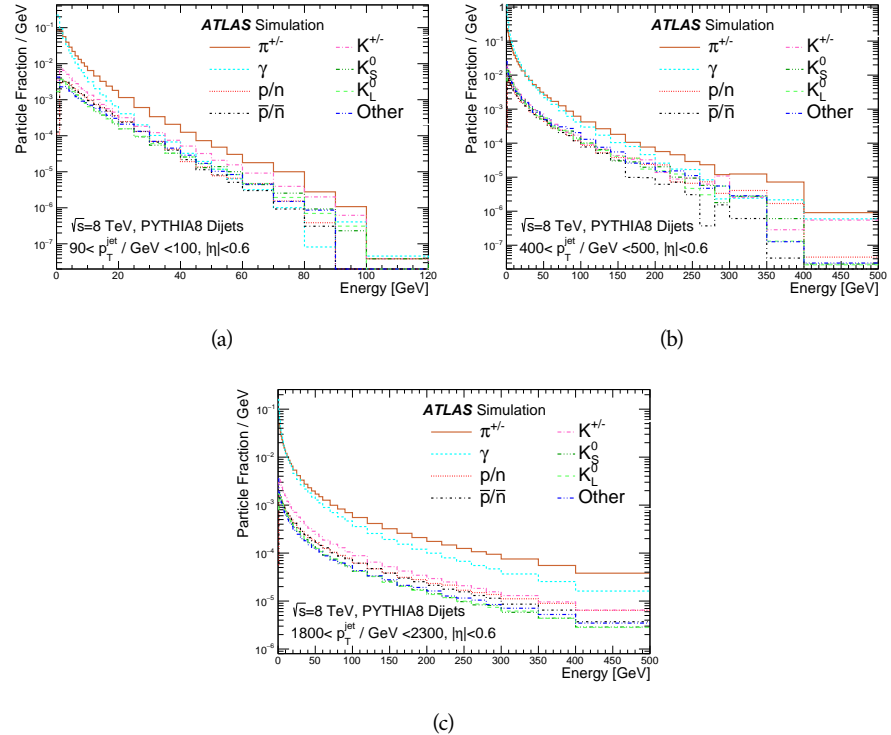


Figure 52: The spectra of true particles inside anti- k_t , $R = 0.4$ jets with (a) $90 < p_T/\text{GeV} < 100$, (b) $400 < p_T/\text{GeV} < 500$, and (c) $1800 < p_T/\text{GeV} < 2300$.

1826 per [13]. These uncertainties cover differences between the data and simulation
 1827 in the modeling of calorimeter response to a given particle. No uncertainties are
 1828 added for the difference between particle composition of jets in data and simu-
 1829 lation.

1830 From these terms, the jet energy scale and uncertainty is built up from indi-
 1831 vidual energy deposits in simulation. Each uncertainty term is treated indepen-
 1832 dently, and are taken to be gaussian distributed. The resulting scale and uncer-
 1833 tainty is shown in Figure 53, where the mean response is measured relative to
 1834 the calibrated energy reported by simulation. The dominant uncertainties come
 1835 from the statistical uncertainties on the E/p measurements at lower energies and
 1836 the additional uncertainty for out of range measurements at higher energies. The
 1837 total uncertainty from this method at intermediate jet energies is comparable to
 1838 other simulation-based methods [42] and is about twice as large as in-situ meth-
 1839 ods using data [39]. This method is the only one which provides an estimation
 1840 above 1.8 TeV, however, and so is still a crucial technique in analyses that search
 1841 for very energetic jets.

1842 These techniques can also be used to measure the correlation between bins of
 1843 average reconstructed jet momentum across a range of p_T and $|\eta|$, where cor-
 1844 relations are expected because of a similarity in particle composition at similar
 1845 energies. Figure 54 shows these correlations, where the uncertainties on jets in
 1846 neighboring bins are typically between 30% and 60% correlated. The uncertainty
 1847 on all jets becomes significantly correlated at high energies and larger pseudora-

Abbrev.	Description	Δ (%)	σ (%)
In situ E/p	The comparison of $\langle E/p \rangle_{\text{COR}}$ as described in Chapter 8 with statistical uncertainties from 500 MeV to 20 GeV.	0-3	1-5
CTB	The main $\langle E/p \rangle$ comparison uncertainties, binned in p and $ \eta $, as derived from the combined test beam results, from 20 to 350 GeV [41].	0-3	1-5
E/p Zero Fraction	The difference in the zero-fraction between data and MC simulation from 500 MeV to 20 GeV.	5-25	1-5
E/p Threshold	The uncertainty in the EM calorimeter response from the potential mismodeling of threshold effects in topological clustering.	0	0-10
Neutral	The uncertainty in the calorimeter response to neutral hadrons based on studies of physics model variations.	0	5-10
K_L	An additional uncertainty in the response to neutral K_L in the calorimeter based on studies of physics model variations.	0	20
E/p Misalignment	The uncertainty in the p measurement from misalignment of the ID.	0	1
Hadrons, $p > 350$ GeV	A flat uncertainty for all particles above the energy range or outside the longitudinal range probed with the combined test beam.	0	10

Table 6: The dominant sources of corrections and systematic uncertainties in the [JES](#) estimation technique, including typical values for the correcting shift (Δ) and the associated uncertainty (σ).

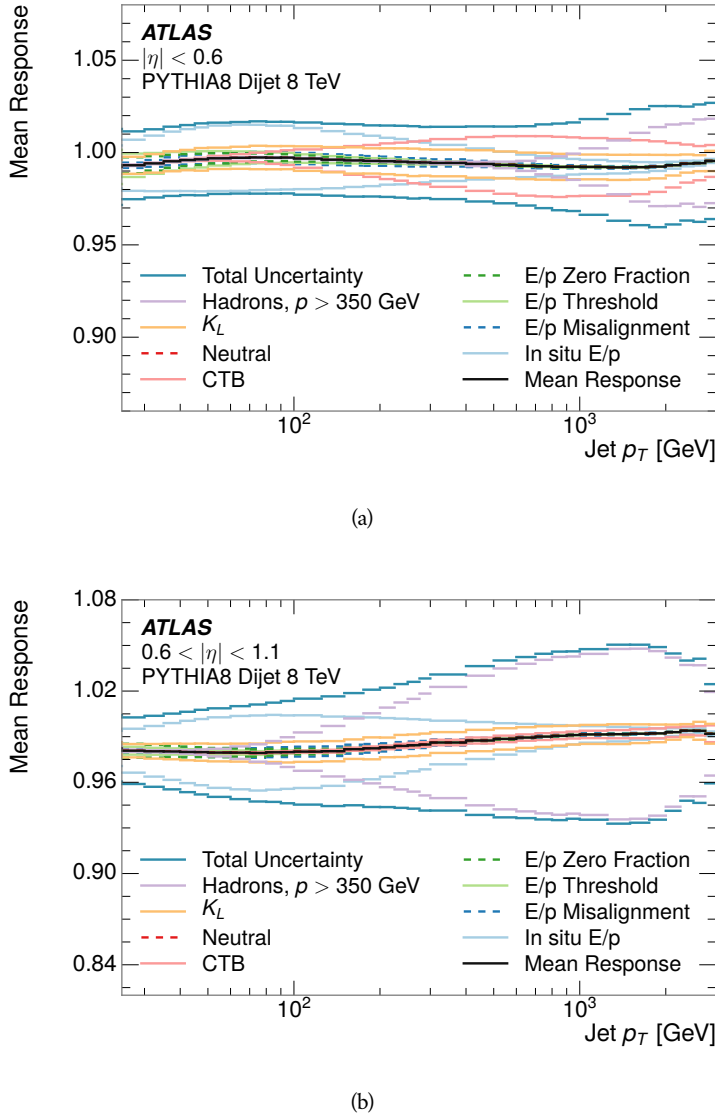


Figure 53: The [JES](#) uncertainty contributions, as well as the total [JES](#) uncertainty, as a function of jet p_T for (a) $|\eta| < 0.6$ and (b) $0.6 < |\eta| < 1.1$.

1848 pidities, when the uncertainty becomes dominated by the single term reflecting
 1849 out of range particles.

1850 9.3 SUMMARY

1851 The technique described above provides a jet energy scale and uncertainty by
 1852 building up jet corrections from the energy deposits of constituent particles. The
 1853 E/p measurements are crucial in providing corrections for the majority of parti-
 1854 cles in the jets. The uncertainty derived this way is between 2 and 5% and is about
 1855 twice as large at corresponding momentum than jet balance methods. However
 1856 this is the only uncertainty available for very energetic jets using 2012 data and
 1857 simulation, and repeating this method with Run 2 data and simulation will be

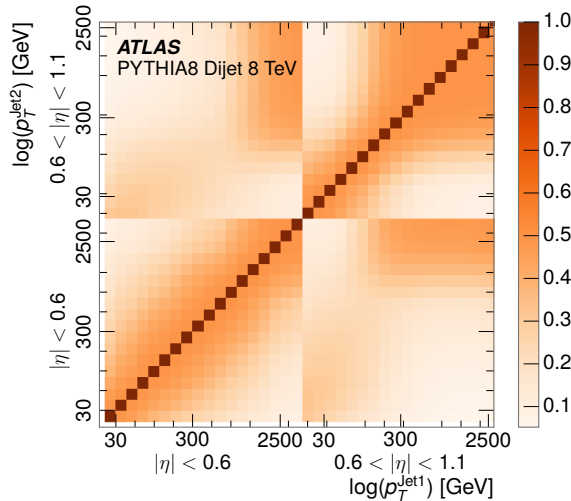


Figure 54: The JES correlations as a function of jet p_T and $|\eta|$ for jets in the central region of the detector.

1858 important in providing an uncertainty for the most energetic jets in 13 TeV col-
1859 lisions.

1860

PART V

1861

SEARCH FOR LONG-LIVED PARTICLES

1862

You can put some informational part preamble text here.

1863

1864 LONG-LIVED PARTICLES IN ATLAS

1865 As discussed in Section 2.3, various limitations in the SM suggest a need for new
 1866 particles at the TeV scale. A wide range of extensions to the Standard Model
 1867 predict that these new particles can have lifetimes greater than approximately
 1868 one-hundredth of a nanosecond. These include theories with universal extra-
 1869 dimensions [43, 44], with new fermions [45], and with leptoquarks [46]. Many
 1870 SUSY theories also produce these Long-Lived Particles (LLPs), in both R-Parity
 1871 violating [47–49] and R-Parity conserving [50–53] formulations. Split super-
 1872 symmetry [54, 55], for example, predicts long-lived gluinos with O(TeV) masses.
 1873 This search focuses specifically on the SUSY case, but many of the results are
 1874 generic to any model with LLPs.

1875 Long-lived gluinos or squarks carry color-charge and will thus hadronize into
 1876 color neutral bound states called R-Hadrons. These are composit particles like
 1877 the usual hadrons but with one supersymmetric constituent, for example $\tilde{g}q\bar{q}$
 1878 and $\tilde{q}\bar{q}$. Through this hadronization process, the neutral gluino can acquire a
 1879 charge. Gluino pair production, $pp \rightarrow \tilde{g}\tilde{g}$ has the largest cross sectional increase
 1880 with the increase in energy to 13 TeV, and so this search focuses on gluino R-
 1881 Hadrons. Planned future updates will extend the case to explicitly include squark
 1882 and chargino models, but the method covers any long-lived, charged, massive
 1883 particle.

1884 10.1 EVENT TOPOLOGY

1885 The majority of SUSY models predict that gluinos will be produced in pairs at
 1886 the LHC, through processes like $pp \rightarrow q\bar{q} \rightarrow \tilde{g}\tilde{g}$ and $pp \rightarrow gg \rightarrow \tilde{g}\tilde{g}$, where the
 1887 gluon mode dominates for the collision energy and gluino masses considered
 1888 for this search. During their production, the long-lived gluinos hadronize into
 1889 color singlet bound states including $\tilde{g}q\bar{q}$, $\tilde{g}qqq$, and even $\tilde{g}g$ [56]. The probability
 1890 to form the gluon-only bound states is a free parameter usually taken to be 0.1,
 1891 while the meson states are favored among the R-Hadrons [57]. The charged and
 1892 neutral states are approximately equally likely for mesons, so the R-Hadrons will
 1893 be charged roughly 50% of the time.

1894 These channels produce R-Hadrons with large p_T , comparable to their mass,
 1895 so that they typically propagate with $0.2 < \beta < 0.9$ [57]. The fragmentation that
 1896 produces these hadrons is very hard, so the jet structure around the R-Hadron
 1897 is minimal, with less than 5 GeV of summed particle momentum expected in a
 1898 cone of $\Delta R < 0.25$ around the R-Hadron [57]. After hadronization, depending
 1899 on the gluino lifetime, the R-Hadrons then decay into hadrons and a LSP [56].

1900 In summary, the expected event for pair-produced long-lived gluinos is very
 1901 simple: two isolated, high-momentum R-Hadrons that propagate through the
 1902 detector before decaying into jets. The observable features of such events depend

1903 strongly on the interaction of the R-Hadron with the material of the detector and
 1904 also its lifetime. Section 10.1.1 describes the interactions of R-Hadrons which
 1905 reach the various detector elements in ATLAS and Section 10.1.2 provides a sum-
 1906 mary of the observable event descriptions for R-Hadrons of various lifetimes.

1907 10.11 DETECTOR INTERACTIONS

1908 After approximately 0.2 ns, the R-Hadron reaches the pixel detector. If charged,
 1909 it deposits energy into the material through repeated single collisions that result
 1910 in ionization of the silicon substrate [7]. Because of its comparatively low β , the
 1911 ionization energy can be significantly greater than expected for SM particles be-
 1912 cause the most-probable energy loss grows significantly as β decreases [7]. This
 1913 large ionization can be measured through the time over threshold (ToT) read out
 1914 from the pixel detector as described in Section 7.1.1.2. Large ionization in the
 1915 inner detector is one of the major characteristic features of LLPs.

1916 Throughout the next few nanoseconds, the R-Hadron propagates through the
 1917 remainder of the inner detector. A charged R-Hadron will provide hits in each
 1918 of these systems as would any other charged particle, and can be reconstructed
 1919 as a track. The track reconstruction provides a measurement of its trajectory
 1920 and thus its momentum as described in Section 7.1. The large momentum is
 1921 another characteristic feature of massive particles produced at the LHC. **Note: At**
 1922 **this point I am failing to mention that the TRT provides a possible dE/dx**
 1923 **measurement, because no one uses it as far as I know.**

1924 As of roughly 20 ns, the R-Hadron enters the calorimeter where it interacts
 1925 hadronically with the material. Because of its large mass and momentum, the
 1926 R-Hadron does not typically stop in the calorimeter, but rather deposits a small
 1927 fraction of its energy through repeated interactions with nucleons. The proba-
 1928 bility of interaction between the gluino itself and a nucleon is low because the
 1929 cross section drops off with the inverse square of its mass, so the interactions are
 1930 primarily governed by the light constituents [58]. Each of these interactions can
 1931 potentially change that quark content and thus change the sign of the R-Hadron,
 1932 so that the charge at exit is typically uncorrelated with the charge at entry [57].
 1933 The total energy deposited in the calorimeters during the propagation is small
 1934 compared to the kinetic energy of the R-Hadron, around 20-40 GeV, so that
 1935 E/p is typically less than 0.1 [57].

1936 Then, 30 ns after the collision, it reaches the muon system, where it again
 1937 ionizes in the material if charged and can be reconstructed as a muon track. Be-
 1938 cause of the charge-flipping interactions in the calorimeter, this track may have
 1939 the opposite sign of the track reconstructed in the inner detector, or there may
 1940 be a track present when there was none in the inner detector and vice-versa. The
 1941 propagation time at the typically lower β results in a significant delay compared
 1942 to muons, and that delay can be assessed in terms of a time-of-flight measure-
 1943 ment. Because of the probability of charge-flip and late arrival, there is a signif-
 1944 icant chance that an R-Hadron which was produced with a charge will not be
 1945 identified as a muon. The long time-of-flight is another characteristic feature of
 1946 R-Hadrons which are reconstructed as muons.

1947 10.1.2 LIFETIME DEPENDENCE

1948 The above description assumed a lifetime long enough for the R-Hadron to exit
 1949 the detector, which through this search is referred to as “stable”, even though
 1950 the particle may decay after exiting the detector. There are several unique sig-
 1951 natures at shorter lifetimes where the R-Hadron decays in various parts of the
 1952 inner detector; these lifetimes are referred to as “metastable”.

1953 The shortest case where the R-Hadron is considered metastable is for life-
 1954 times around 0.01 ns, where the particle decays before reaching any of the de-
 1955 tector elements. Although the R-Hadrons are produced opposite each other in
 1956 the transverse plane, each R-Hadron decays to a jet and an LSP. The LSPs are not
 1957 measured, so the produced jets can be significantly imbalanced in the transverse
 1958 plane which results in large missing energy. That missing energy can be used
 1959 to trigger candidate events, and provides the most efficient trigger option for
 1960 shorter lifetimes. Additionally, the precision of the tracking system allows the
 1961 displaced vertex of the R-Hadron decay to be reconstructed from the charged
 1962 particles in the jet. The distance of that vertex from the interaction point can
 1963 be used to distinguish R-Hadron decays from other processes. Figure 55 shows
 1964 a schematic diagram of an example R-Hadron event with such a lifetime. The
 1965 diagram is not to scale, but instead illustrates the detector interactions in the
 1966 pixel detector, calorimeters, and muon system. It includes a representation of
 1967 the charged R-Hadron and the neutral R-Hadron, as well as the LSPs and jets
 1968 (shown as charged hadrons) produced in the decay. Neutral hadrons may also
 1969 be produced in the decay but are not depicted. Previous searches on ATLAS have
 1970 used the displaced vertex to target LLP decays [59].

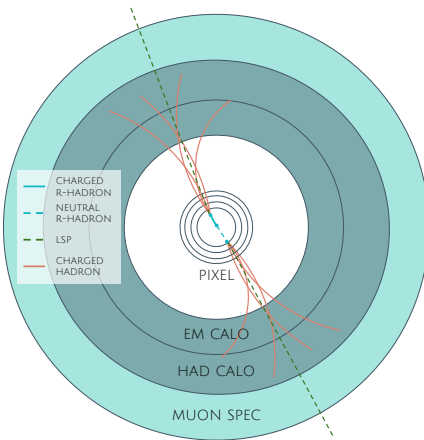


Figure 55: A schematic diagram of an R-Hadron event with a lifetime around 0.01 ns. The diagram includes one charged R-Hadron (solid blue), one neutral R-Hadron (dashed blue), LSPs (dashed green) and charged hadrons (solid orange). The pixel detector, calorimeters, and muon system are illustrated but not to scale.

1971 The next distinguishable case occurs at lifetimes greater than 0.1 ns, where
 1972 the R-Hadron forms a partial track in the inner detector. If the decay products
 1973 are sufficiently soft, they may not be reconstructed, and this forms a unique sig-

nature of a disappearing track. An example of such an event is illustrated in Figure 56, which shows the short track in the inner detector and the undetected soft charged hadron and LSP that are produced. A dedicated search on ATLAS used the disappearing track signature to search for LLP in Run 1 [60]. **zNote: might not be worth mentioning the disappearing track here since it is actually a chargino search, the soft pion is pretty unique to charginos.**

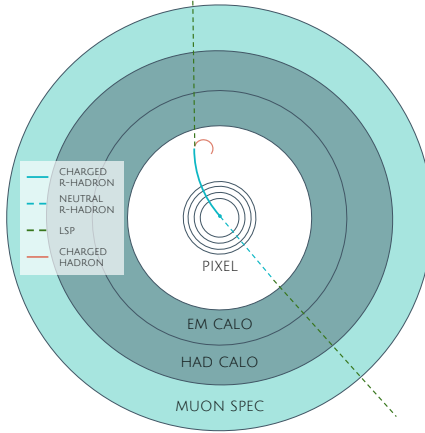


Figure 56: A schematic diagram of an R-Hadron event with a lifetime around 4 ns. The diagram includes one charged R-Hadron (solid blue), one neutral R-Hadron (dashed blue), LSPs (dashed green) and a charged hadron (solid orange). The pixel detector, calorimeters, and muon system are illustrated but not to scale.

If the decay products are not soft, the R-Hadron daughters form jets, resulting in an event-level signature of up to two high-momentum tracks, jets, and significant missing energy. The missing energy has the same origin as in the case of 0.01 ns lifetimes, from the decay to unmeasured particles, and again can be large. The high-momentum tracks will also have the characteristically high-ionization of massive, long-lived particles in the inner detector. Figure 57 illustrates an example event with one charged R-Hadron which decays after approximately 10 ns, and shows how the jets from the decay can still be reconstructed in the calorimeter. Several previous searches on ATLAS from Run 1 have used this signature to search for R-Hadrons [61, 62], including a dedicated search for metastable particles [63].

If the lifetime is longer than several nanoseconds, in the range of 15-30 ns, the R-Hadron decay can occur in or after the calorimeters, but prior to reaching the muon system. This case is similar to the above, although the jets may not be reconstructed, and is covered by many of the same search strategies. The events still often have large missing energy, although it is generated through different mechanisms. The R-Hadrons do not deposit much energy in the calorimeters, so a neutral R-Hadron will not enter into the missing energy calculation. A charged R-Hadron opposite a neutral R-Hadron will thus generate significant missing energy, and close to 50% of pair-produced R-Hadron events fall into this category. If both R-Hadrons are neutral then the missing energy will be low because neither is detected. Two charged R-Hadrons will also result in low missing energy because both are reconstructed as tracks and will balance each other in the trans-

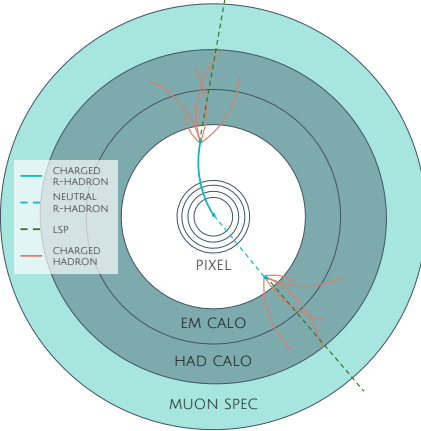


Figure 57: A schematic diagram of an R-Hadron event with a lifetime around 5 ns. The diagram includes one charged R-Hadron (solid blue), one neutral R-Hadron (dashed blue), LSPs (dashed green) and charged hadrons (solid orange). The pixel detector, calorimeters, and muon system are illustrated but not to scale.

verse plane. A small fraction of the time, one of the charged R-Hadron tracks may fail quality requirements and thus be excluded from the missing energy calculation and again result in significant missing energy. Figure 58 illustrates another example event with one charged R-Hadron which decays after approximately 20 ns, and shows how the jets from the decay might not be reconstructed.

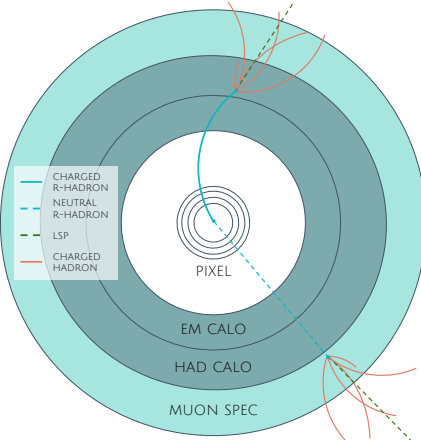


Figure 58: A schematic diagram of an R-Hadron event with a lifetime around 20 ns. The diagram includes one charged R-Hadron (solid blue), one neutral R-Hadron (dashed blue), LSPs (dashed green) and charged hadrons (solid orange). The pixel detector, calorimeters, and muon system are illustrated but not to scale.

The longest lifetimes, the stable case, has all of the features of the 30-50 ns case but with the addition of muon tracks for any R-Hadrons that exit the calorimeter with a charge. That muon track can provide additional information from time-of-flight measurements to help identify LSPs. An example of the event topology for one charged and one neutral stable R-Hadron is shown in Figure 59. Some searches on ATLAS have included this information to improve the search reach for stable particles [62, 64].

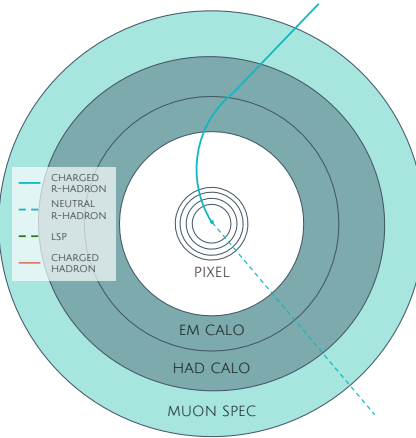


Figure 59: A schematic diagram of an R-Hadron event with a lifetime around 20 ns. The diagram includes one charged R-Hadron (solid blue) and one neutral R-Hadron (dashed blue). The pixel detector, calorimeters, and muon system are illustrated but not to scale.

2015 10.2 SIMULATION

2016 All of the event topologies discussed above are explored by simulations of R-
 2017 Hadron events in the [ATLAS](#) detector. A large number of such samples are gen-
 2018 erated to determine signal efficiencies, to measure expected yields, and to esti-
 2019 mate uncertainties. The primary interaction, pair production of gluinos with
 2020 masses between 400 and 3000 GeV, is simulated using [Pythia 6.4.27](#) [65]
 2021 with the AUET2B [66] set of tuned parameters for the underlying event and
 2022 the CTEQ6L1 [40] parton distribution function ([PDF](#)) set. The simulated inter-
 2023 actions include a modeling of pileup by adding secondary, minimum bias in-
 2024 teractions from both the same (in-time pileup) and nearby (out-of-time pileup)
 2025 bunch crossings. This event generation is then augmented with a dedicated
 2026 hadronization routine to hadronize the long-lived gluinos into final states with
 2027 R-Hadrons [67], with the probability to form a gluon-gluino bound set at 10% [68].

2028 The cross sections used for these processes are calculated at next-to-leading
 2029 order ([NLO](#)) in the strong coupling constant with a resummation of soft-gluon
 2030 emmission at next-to-leading logarithmic ([NLL](#)) [69–73]. The nominal predic-
 2031 tions and the uncertainties for each mass point are taken from an envelope of
 2032 cross-section predictions using different [PDF](#) sets and factorization and renor-
 2033 malization scales [74].

2034 The R-Hadrons then undergo a full detector simulation [], where the interac-
 2035 tions of the R-Hadrons with the material of the detector are described by dedi-
 2036 cated [Geant4](#) [10] routines. These routines model the interactions described in
 2037 Section 10.1.1, including the ionizing interactions in the silicon modules of the
 2038 inner detector and the R-Hadron-nucleon interactions in the calorimeters [75,
 2039 76]. The specific routine chosen to describe the interactions of the R-Hadrons
 2040 with nucleons, the “generic model”, uses a pragmatic approach where the scatter-
 2041 ing cross section is taken to be a constant 12 mb per light quark. In this model

2042 the gluino itself does not interact at all except through its role as a reservoir of
2043 kinetic energy.

2044 The lifetimes of these R-Hadrons are then simulated at several working points,
2045 $\tau = 0.1, 1.0, 3.0, 10, 30, 50$ and detector stable, where the particle is required to
2046 decay after propagating for a time compatible with its lifetime. Only one decay
2047 mode is simulated for these samples, $\tilde{g} \rightarrow q\bar{q}\tilde{\chi}_1^0$ with the neutralino mass set to
2048 100 GeV, which is chosen because it has the highest sensitivity among all of the
2049 modes studied in previous searches [63]. Heavier neutralinos have similar results
2050 but generate less missing energy which reduces the efficiency of triggering.

2051 All of the simulated events are then reconstructed using the same software
2052 used for collision data. The fully reconstructed events are then reweighted to
2053 match the distribution of initial state radiation in an alternative sample of events,
2054 generated with MG5_aMC@NLO [77], which has a more accurate description of ra-
2055 diate effects than Pythia6. This reweighting provides a more accurate descrip-
2056 tion of the momentum of the gluino-gluino system and is important in modeling
2057 the efficiency of triggering and offline event selection.

2058

2059 EVENT SELECTION

2060 The [LLPs](#) targeted by this search differ in their interactions with the detector from
 2061 [SM](#) particles primarily because of their large mass. When produced at the ener-
 2062 gies available at the [LHC](#), that large mass results in a low β (typically $0.2 < \beta <$
 2063 0.9). Such slow-moving particles heavily ionize in detector material. Each layer
 2064 of the pixel detector provides a measurement of that ionization, through [ToT](#), as
 2065 discussed in Section 7.1.1.2. The ionization in the pixel detector, quantified in
 2066 terms of dE/dx , provides the major focus for this search technique, along with
 2067 the momentum measured in the entire inner detector. It is effective both for its
 2068 discriminating power and its use in reconstructing a particle's mass, and it can
 2069 be used for a wide range of masses and lifetimes as discussed in Section 10.1.2.
 2070 However dE/dx needs to be augmented with a few additional selection require-
 2071 ments to provide a mechanism for triggering and to further reduce backgrounds.

2072 Ionization itself is not currently accessible for triggering, so this search in-
 2073 stead relies on E_T^{miss} to trigger signal events. Although triggering on E_T^{miss} can
 2074 be inefficient, E_T^{miss} is often large for many production mechanisms of [LLPs](#), as
 2075 discussed in Section 10.1.

2076 The use of ionization to reject [SM](#) backgrounds relies on well-measured, high-
 2077 momentum tracks, so some basic requirements on quality and kinematics are
 2078 placed on the tracks considered in this search. These quality requirements have
 2079 been significantly enhanced in Run 2 by a newly introduced tracking variable
 2080 that is very effective in removing highly-ionizing backgrounds caused by over-
 2081 lapping tracks. A few additional requirements are placed on the tracks consid-
 2082 ered for [LLP](#) candidates that increase background rejection by targeting specific
 2083 types of [SM](#) particles. These techniques provide a significant analysis improve-
 2084 ment over previous iterations of ionization-based searches on ATLAS by provid-
 2085 ing additional background rejection with minimal loss in signal efficiency.

2086 The ionization measurement with the Pixel detector can be calibrated to pro-
 2087 vide an estimator of $\beta\gamma$. That estimate, together with the momentum measure-
 2088 ment provided by tracking, can be used to reconstruct a mass for each track
 2089 which traverses the pixel detector. That mass variable will be peaked at the [LLP](#)
 2090 mass for any signal, and provides an additional tool to search for an excess. In
 2091 addition to an explicit requirement on ionization, this search constructs a mass-
 2092 window for each targeted signal mass in order to evaluate any excess of events
 2093 and to set limits.

2094 The strategy discussed here is optimized for lifetimes of $O(1) - O(10)$ ns.
 2095 Pixel ionization is especially useful in this regime as particles only need to prop-
 2096 agate through the first seven layers of the inner detector, about 37 cm from the
 2097 beam axis. The search is still competitive with other searches for [LLPs](#) at longer
 2098 lifetimes, because the primary discriminating variables are still applicable even
 2099 for particles that do not decay within the detector [64]. Although the majority of

2100 the requirements will be the same for all lifetimes, two signal regions are defined
 2101 to optimize separately for intermediate and long lifetime particles.

2102 11.1 TRIGGER

2103 Triggering remains a significant difficulty in defining an event selection with
 2104 high signal efficiency in a search for LLPs. There are no triggers available in
 2105 the current ATLAS system that can fire directly from a high momentum track
 2106 with large ionization (Section 6.6). Although in some configurations a charged
 2107 LLP can fire muon triggers, this requirement introduces significant model depen-
 2108 dence on both the allowed lifetimes and the interactions in the calorimeter [57],
 2109 as discussed in Section 10.1.1.

2110 For a search targeting particles which may decay prior to reaching the muon
 2111 system, the most efficient available trigger is based on missing energy [57]. As
 2112 discussed in Section 10.1, signal events can produce significant E_T^{miss} by a few
 2113 mechanisms. At the trigger level however, the missing energy is only calculated
 2114 using the calorimeters (Section 6.6) where the R-Hadrons deposit little energy.
 2115 So, at short lifetimes, E_T^{miss} measured in the calorimeter is generated by an im-
 2116 balance between the jets and undetected LSPs produced in R-Hadron decays. At
 2117 longer lifetimes, without the decay products, missing energy is only produced in
 2118 the calorimeters when the R-Hadrons recoil against an initial state radiation (ISR)
 2119 jet.

2120 These features are highlighted in Figure 60, which shows the E_T^{miss} distribu-
 2121 tions for simulated short lifetime (3 ns) and stable R-Hadron events. The figure
 2122 includes both the offline E_T^{miss} , the missing energy calculated with all available
 2123 information, and Calorimeter E_T^{miss} , the missing energy calculated using only
 2124 information available at the calorimeter which approximates the missing energy
 2125 available at the trigger. The short lifetime sample has significantly greater E_T^{miss}
 2126 and Calorimeter E_T^{miss} than the stable sample as expected. For the stable sam-
 2127 ple, a small fraction of events with very large E_T^{miss} (about 5%) migrate into the
 2128 bin with very small Calorimeter E_T^{miss} because the E_T^{miss} produced by a charged
 2129 R-Hadron track opposite a neutral R-Hadron track does not contribute any miss-
 2130 ing energy in the calorimeters.

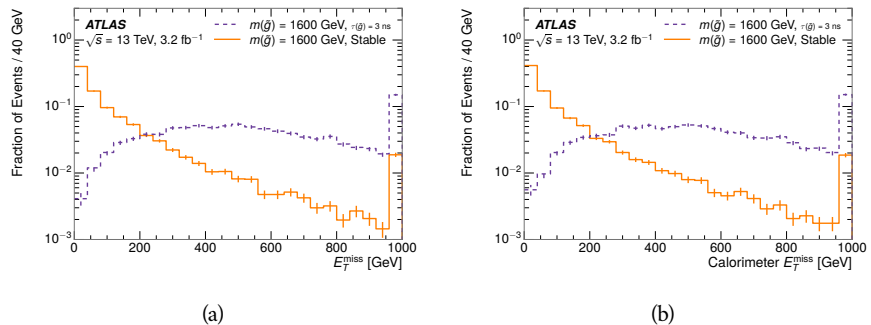


Figure 60: The distribution of (a) E_T^{miss} and (b) Calorimeter E_T^{miss} for simulated signal
 events before the trigger requirement.

2131 So, either case to some extent relies on kinematic degrees of freedom to pro-
 2132 duce missing energy, as the pair-produced LLPs tend to balance each other in
 2133 the transverse plain. That balance results in a relatively low efficiency for long-
 2134 lifetime particles, roughly 40%, and efficiencies between 65% and 95% for shorter
 2135 lifetimes depending on both the mass and the lifetime. For long lifetimes in par-
 2136 ticular, the presence of ISR is important in providing an imbalance in the trans-
 2137 verse plane, and is an important aspect of modeling the selection efficiency for
 2138 R-Hadron events.

2139 The missing energy trigger with the lowest threshold available is chosen for
 2140 this selection in order to maximize the trigger efficiency. During 2015 data col-
 2141 lection this was the HLT_xe70 trigger, which used a 50 GeV threshold on miss-
 2142 ing energy at LVL1 and a 70 GeV threshold on missing energy at the HLT. These
 2143 formation of the trigger decision for missing energy was discussed in more detail
 2144 in Section 6.6.

2145 11.2 KINEMATICS AND ISOLATION

2146 After the trigger requirement, each event is required to have a primary vertex
 2147 reconstructed from at least two well-measured tracks in the inner detector, each
 2148 with $p_T > 400$ MeV. If more than one such vertex exists, the primary vertex
 2149 is taken to be the one with the largest summed track momentum for all tracks
 2150 associated to that vertex. The offline reconstructed E_T^{miss} is required to be above
 2151 130 GeV to additionally reject SM backgrounds. The transverse missing energy
 2152 is calculated using fully reconstructed and calibrated offline objects, as described
 2153 in Section 7.5. In particular the E_T^{miss} definition in this selection uses jets recon-
 2154 structed with the anti- k_t algorithm with radius $R = 0.4$ from clusters of energy
 2155 in the calorimeter (Section 7.2) and with $p_T > 20$ GeV, as well as reconstructed
 2156 muons, electrons, and tracks not identified as another object type.

2157 The E_T^{miss} distributions are shown for data and a few simulated signals in Fig-
 2158 ure 61, after the trigger requirement. The cut placed at 130 GeV is 95% effi-
 2159 cient for metastable and 90% efficient for stable particles, after the trigger re-
 2160 quirement, because of the missing energy generating mechanisms discussed pre-
 2161 viously. The distribution of data in this figure and subsequent figures in this sec-
 2162 tion can be interpreted as the distribution of backgrounds, as any signal contam-
 2163 ination would be negligible if present at these early stages of the selection (prior
 2164 to the final requirement on ionization). The background falls rapidly with miss-
 2165 ing energy, motivating the direct requirement on E_T^{miss} for the signal region. Al-
 2166 though a tighter requirement than the specified value of 130 GeV would seem to
 2167 increase the search potential from these early distributions, other requirements
 2168 are more optimal when taken as a whole. The specific values for each require-
 2169 ment in signal region were optimized considering the increase in discovery reach
 2170 for tightening the requirement on each discriminating variable. **NOTE: If space**
 2171 **and time permit, I will add a whole section about signal region optimiza-**
 2172 **tion..**

2173 It is typically the practice for searches for new physics on ATLAS to place an
 2174 offline requirement on the triggering variable that is sufficiently tight to guar-

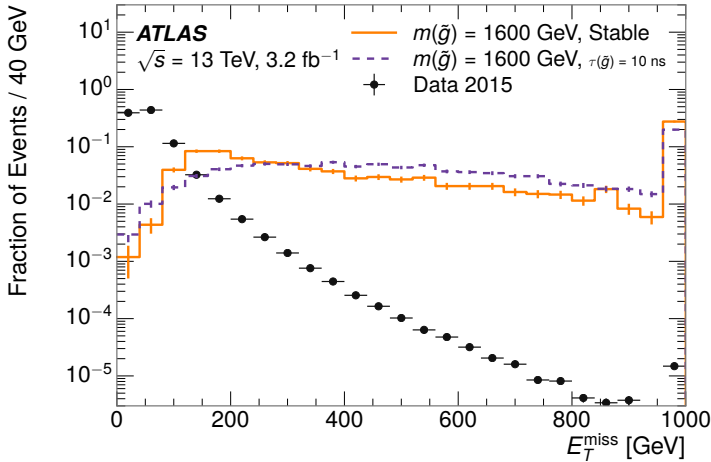


Figure 61: The distribution of E_T^{miss} for data and simulated signal events, after the trigger requirement.

2175 antee that the event would pass the trigger. Such a tight requirement makes the
 2176 uncertainty on the trigger efficiency of the simulation negligible, as modeling the
 2177 regime where the trigger is only partially efficient can be difficult. In this analy-
 2178 sis, however, because of the atypical interactions of R-Hadrons with the tracker
 2179 and the calorimeter, the offline requirement on E_T^{miss} is not sufficient to guar-
 2180 antee a 100% trigger efficiency even at large values, as can be seen in Figure 62.
 2181 This figure shows the efficiency for passing the HLT_xe70 trigger as a function
 2182 of the requirement on E_T^{miss} , which plateaus to roughly 85% even at large values.
 2183 This plateau does not reach 100% because events which have large offline miss-
 2184 ing energy from a neutral R-Hadron produced opposite of a charged R-Hadron
 2185 can have low missing energy in the calorimeters. The Calorimeter E_T^{miss} , on the
 2186 other hand, does not have this effect and reaches 100% efficiency at large values
 2187 because it is the quantity that directly corresponds to the trigger threshold. In
 2188 both cases the efficiency of triggering is greater for the short lifetime sample be-
 2189 cause the late decays to hadrons and LSPs produce an imbalance in the calorime-
 2190 ters even though they may not be reconstructed offline as tracks or jets. For this
 2191 reason, the requirement on E_T^{miss} is determined by optimizing the background
 2192 rejection even though it corresponds to a value of trigger efficiency significantly
 2193 below 1.0.

2194 Potential signal events are then required to have at least one candidate LLP
 2195 track. Although the LLPs are produced in pairs, many models do not consistently
 2196 yield two charged particles. For example, in the R-Hadron model highlighted
 2197 here, only 20% of events have two charged R-Hadrons while 47% of events have
 2198 just one. A signal region requiring two charged candidates could be a powerful
 2199 improvement in background rejection for a larger dataset, but it is not consid-
 2200 ered in this version of the analysis as it was found to be unnecessary to reject the
 2201 majority of backgrounds.

2202 For a track to be selected as a candidate, it must have $p_T > 50 \text{ GeV}$ and pass
 2203 basic quality requirements. The track must be associated to the primary vertex.

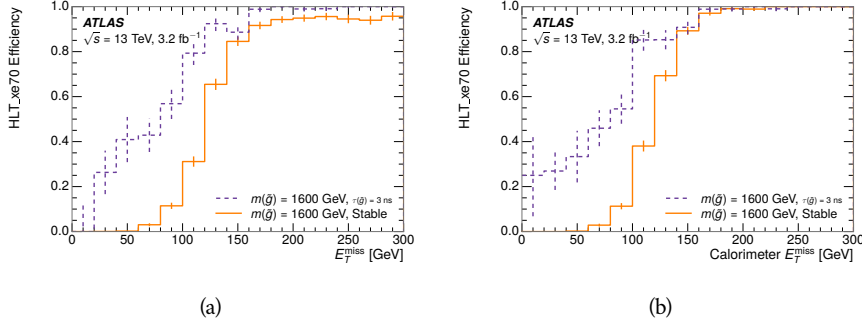


Figure 62: The trigger efficiency for the HLT_xe70 trigger requirement as a function of (a) E_T^{miss} and (b) Calorimeter E_T^{miss} for simulated signal events.

It must also have at least seven clusters in the silicon layers in the inner detector to ensure an accurate measurement of momentum. Those clusters must include one in the innermost layer if the extrapolated track is expected to pass through that layer. And to ensure a reliable measurement of ionization, the track is required to have at least two clusters in the pixel detector that provide a measurement of dE/dx .

At this point in the selection, there is a significant high-ionization background from multiple tracks that significantly overlap in the inner detector. Previous version of this analysis have rejected these overlaps by an explicit overlap rejection between pairs of fully reconstructed tracks, typically by requiring no additional tracks within a cone around the candidate. This technique, however, fails to remove the background from tracks that overlap so precisely that the tracks cannot be separately resolved, which can be produced in very collimated photon conversions or decays of pions.

A new method, added in Run 2, identifies cluster shapes that are likely formed by multiple particles based on a neural network classification algorithm. The number of clusters that are classified this way in the pixel detector for a given track is called N_{split} . As the shape of clusters requires significantly less spatial separation to identify overlaps than it does to reconstruct two fully resolved tracks, this variable is more effective at rejecting backgrounds from overlaps. Figure 63 shows the dependence of ionization on N_{split} ; as N_{split} increases the most probable value of dE/dx grows significantly up to twice the expected value when $N_{\text{split}} = 4$.

This requirement is very successful in reducing the long positive tail of the dE/dx distributions, as can be seen in Figure 64. Comparing the distribution for “baseline tracks”, tracks with only the above requirements on clusters applied and before the requirement on N_{split} , to the distribution with $N_{\text{split}} = 0$, it is clear that the fraction of tracks with large dE/dx is reduced by several orders of magnitude. The tracks without split hits are very close to the dE/dx distribution of identified muons, which are extremely well isolated on average. Figure 64 also includes the distribution of dE/dx in an example signal simulation to demonstrate how effective dE/dx is as a discriminating variable with this isolation applied. The background falls rapidly for $dE/dx > 1.8 \text{ MeVg}^{-1}\text{cm}^2$

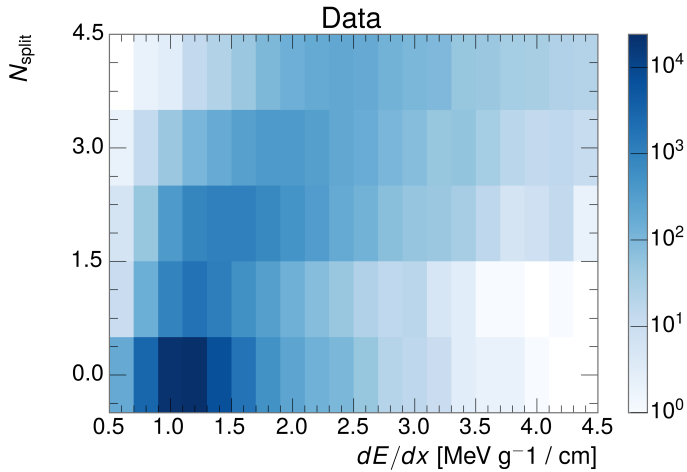


Figure 63: The dependence of dE/dx on N_{split} in data after basic track hit requirements have been applied.

while the majority of the signal, approximately 90% depending on the mass, falls above that threshold. Over 90% of LLP tracks in simulated signal events pass the N_{split} -based isolation requirement.

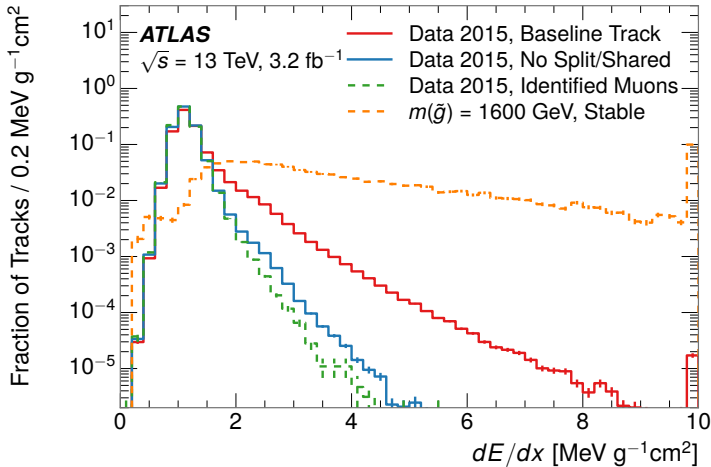


Figure 64: The distribution of dE/dx with various selections applied in data and simulated signal events.

A few additional kinematic requirements are imposed to help reduce SM backgrounds. The momentum of the candidate track must be at least 150 GeV, and the uncertainty on that measurement must be less than 50%. The distribution of momentum is shown in Figure 65 for tracks in data and simulated signal events after the previously discussed requirements on clusters, transverse momentum, and isolation have been imposed. The signal particles are much harder on aver-

age than their backgrounds because of the high energy interactions required to produce them. The transverse mass, M_T , defined as

$$M_T = \sqrt{2p_T E_T^{\text{miss}}(1 - \cos(\Delta\phi(E_T^{\text{miss}}, \text{track})))} \quad (6)$$

estimates the mass of a decay of to a single charged particle and an undetected particle and is required to be greater than 130 GeV to reject contributions from the decay of W bosons. Figure 66 shows the distribution of M_T for data and simulated signal events. The signal is distributed over a wide range of M_T , with about 90% above the threshold value of 130 GeV. The data shows a dual-peaked structure, where the first peak comes from W boson decays and the second peak is a kinematic shaping from the requirements on E_T^{miss} and the track p_T in dijet events.

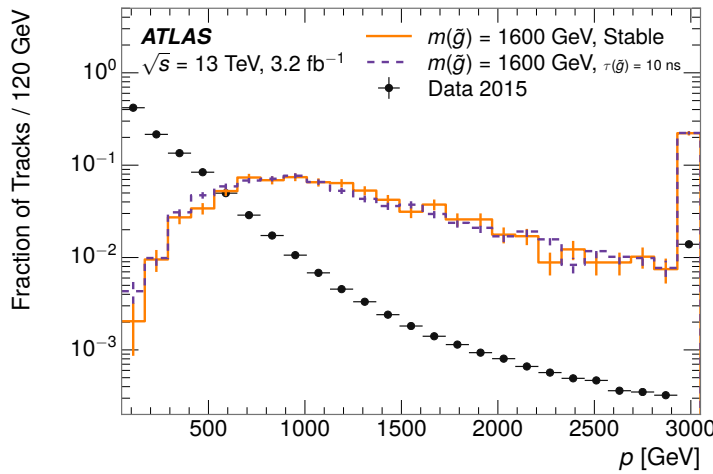


Figure 65: The distribution of track momentum for data and simulated signal events, after previous selection requirements have been applied.

11.3 PARTICLE SPECIES REJECTION

The amount of ionization deposited by particles with low mass and high momentum has a large positive tail [7], so backgrounds can be formed by a wide variety of SM processes when various charged particles have a few randomly large deposits of energy in the pixel detector. Those backgrounds can be additionally reduced by targeting other interactions with the detector where they are expected to have different behavior than R-Hadrons. The interactions with the detector depend on the types of particles produced rather than the processes which produce them, so this search forms a series of rejections to remove backgrounds from individual particle species. These rejections focus on using additional features of the event, other than the kinematics of the candidate track, as they can provide a powerful source of background rejection with very high signal efficiency. However, the lifetime of an R-Hadron can significantly change its

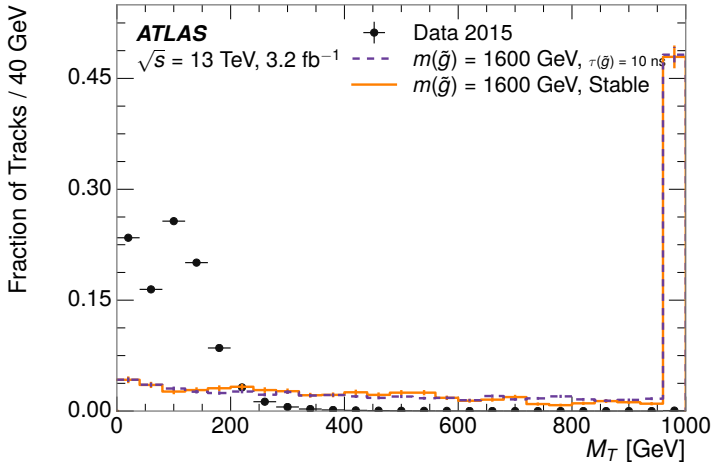


Figure 66: The distribution of M_T for data and simulated signal events, after previous selection requirements have been applied.

detector characteristics, as discussed in Section 10.1.2. To accommodate these differences, the SM rejections defined in this section are split to form two signal regions, one for long-lifetimes particles, the stable region ($50 \leq \tau[\text{ns}] < \infty \text{ ns}$), and one for intermediate lifetime particles, the metastable region ($0.4 < \tau[\text{ns}] < 50$).

Jets can be very effectively rejected by considering the larger-scale isolation of the candidate track. In this case the isolation focuses on the production of nearby particles as a jet-veto, rather than the isolation from overlapping tracks based on N_{split} that was used to reduce high-ionization backgrounds. As explained in Section 10.1, the fragmentation process which produces an R-Hadron is very hard and thus is not expected to produce additional particles with a summed momentum of more than 5 GeV. The jet-veto uses the summed momentum of tracks with a cone of $\Delta R < 0.25$, referred to as p_T^{Cone} , which is shown in Figure 67 for data and simulated signal events. In the data this value has a peak at zero from isolated tracks such as leptons, and a long tail from jets which contains as much as 80% of the background above 20 GeV at this stage of the selection. In signal events p_T^{Cone} is strongly peaked at zero and significantly less than 1% of signal events have p_T^{Cone} above 20 GeV. This makes a requirement of $p_T^{\text{Cone}} < 20 \text{ GeV}$ a very effective method to reject background without losing signal efficiency. For the stable signal region, this cut is further tightened to $p_T^{\text{Cone}} < 5 \text{ GeV}$ as it is the most effective variable remaining to extend the search reach for long lifetimes.

Even for fully isolated particles, there are additional methods to reject each type of particle using information in the muon system and calorimeters. Muons can be identified very reliably using the tracks in the muon system, as described in Section 7.4. For intermediate lifetimes the LLPs do not survive long enough to reach the muon system, and so muons are vetoed by rejecting tracks that associate to a muon with medium muon identification requirements (Section 7.4). For longer lifetimes, this rejection is not applied because LLPs which reach the

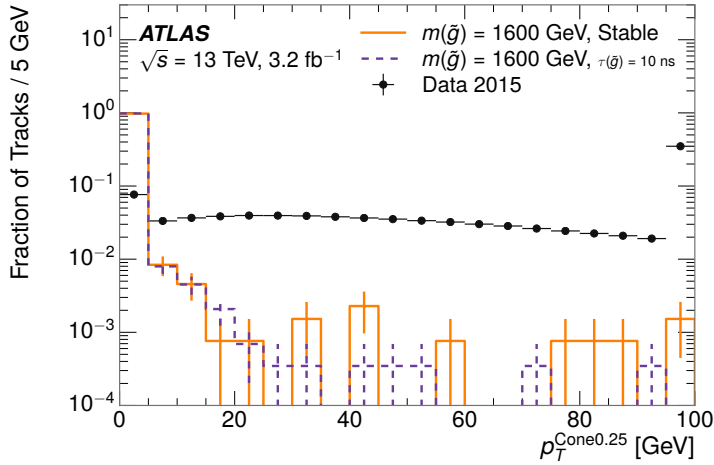


Figure 67: The distribution of summed tracked momentum within a cone of $\Delta R < 0.25$ around the candidate track for data and simulated signal events, after previous selection requirements have been applied.

2298 muon system can be identified as muons as often as 30% of the time in simulated
 2299 samples.

2300 Calorimeter-based particle rejection relies on the expected small deposits of
 2301 energy from LLPs. When the lifetime is long enough to reach the calorimeter, a
 2302 LLP deposits little of its energy as it traverses the material, as discussed in Sec-
 2303 tion 10.1. Even when the particle does decay before the calorimeter, the major-
 2304 ity of its energy is carried away by the LSP and not deposited in the calorimeter.
 2305 In both cases the energy is expected to be distributed across the layers of the
 2306 calorimeters and not peaked in just one layer. This can be quantified in terms
 2307 of E/p , the ratio of calorimeter energy of a nearby jet to the track momentum,
 2308 and f_{EM} , the fraction of energy in that jet within the electromagnetic calorime-
 2309 ter. When no jets fall within a cone of 0.05 of the particle, E/p and f_{EM} are both
 2310 defined as zero. E/p is expected to be above 1.0 for typical SM particles because
 2311 of calibration and the contributions from other nearby particles, as discussed in
 2312 Chapter ???. At these momenta there is no significant zero fraction due to inter-
 2313 actions with the detector or insufficient energy deposits (see Section 8.2.2). f_{EM}
 2314 is peaked close to 1.0 for electrons, and distributed between 10% and 90% for
 2315 hadrons.

2316 These trends can be seen in the two dimensional distribution for signal in
 2317 Figure 68 for stable and metastable (10 ns) events. The majority of R-Hadrons
 2318 in both samples fall into the bin for $E/p = 0$ and $f_{\text{EM}} = 0$ because the majority
 2319 of the time there is no associated jet. In the stable sample, when there often is
 2320 an associated jet, E/p is typically still below 0.1, and the f_{EM} is predominantly
 2321 under 0.8. In the metastable sample, on the other hand, E/p is larger but still
 2322 typically below 0.1 because of actual jets produced during the decay. The f_{EM} is
 2323 much lower on average in this case, below 0.1, because the 10 ns lifetime particles
 2324 rarely decay before passing through the electromagnetic calorimeter. Figure 68
 2325 also includes simulated Z decays to electrons or tau leptons. From the decays

2326 to electrons it is clear that the majority of electrons have f_{EM} above 0.9. The
 2327 tau decays include a variety of products. Muons can be seen in the bin where
 2328 $E/p = 0$ and $f_{\text{EM}} = 0$ because they do not have an associated jet. Electrons fall
 2329 into the range where $E/p > 1$ and $f_{\text{EM}} > 0.9$. Hadronic tau decays are the most
 2330 common, and fall in the range of $0.1 < f_{\text{EM}} < 0.9$ and $E/p > 1.0$.

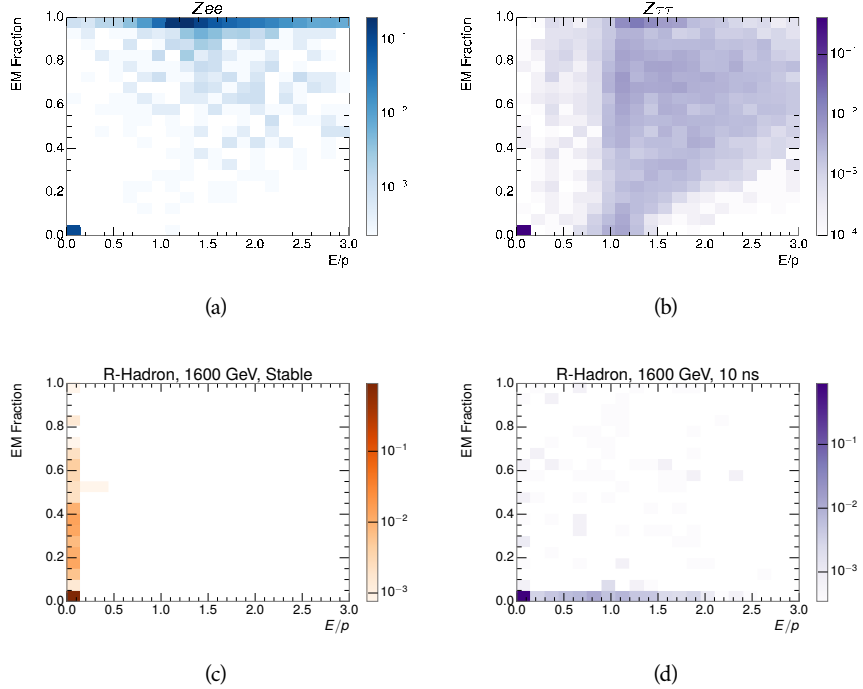


Figure 68: The normalized, two-dimensional distribution of E/p and f_{EM} for simulated
 (a) $Z \rightarrow ee$, (b) $Z \rightarrow \tau\tau$, (c) 1200 GeV Stable R-Hadron events, and (d) 1200
 GeV, 10 ns R-Hadron events.

2331 These differences motivate an electron rejection by requiring an f_{EM} below
 2332 0.9. Similarly, isolated hadrons are rejected by requiring $E/p < 1.0$. These re-
 2333 quirements combine to remove the majority of isolated electrons and hadrons
 2334 but retain over 95% of the simulated signal across a range of masses and lifetimes.

2335 11.4 IONIZATION

2336 The final requirement on the candidate track is the primary discriminating vari-
 2337 able, the ionization in the pixel detector. That ionization is measured in terms
 2338 of dE/dx , which was shown for data and simulated signal events in Figure 64.
 2339 dE/dx is dramatically greater for the high mass signal particles than the back-
 2340 grounds, which start to fall immediately after the minimally ionizing peak at 1.1
 2341 $\text{MeV g}^{-1} \text{cm}^2$. The dE/dx for candidate tracks must be greater than a pseudorapidity-
 2342 dependent threshold, specifically $1.80 - 0.11|\eta| + 0.17\eta^2 - 0.05\eta^3 \text{ MeV g}^{-1} \text{ cm}^{-2}$,
 2343 in order to correct for an approximately 5% dependence of the MIP peak on η .
 2344 The requirement was chosen as part of the signal region optimization, and man-

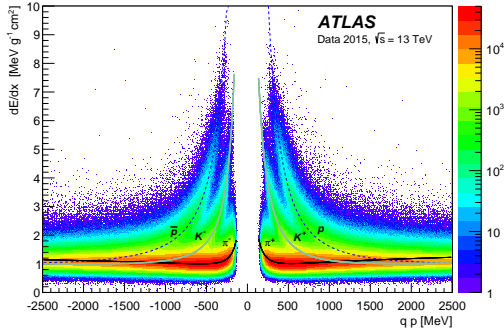


Figure 69: Two-dimensional distribution of dE/dx versus charge signed momentum (qp) for minimum-bias tracks. The fitted distributions of the most probable values for pions, kaons and protons are superimposed.

ages to reduce the backgrounds by a factor of 100 while remaining 70-90% efficient for simulated signal events depending on the mass.

11.4.1 MASS ESTIMATION

The mean value of ionization in silicon is governed by the Bethe equation and the most probable value follows a Landau-Vavilov distribution [7]. Those forms inspire a parametric description of dE/dx in terms of $\beta\gamma$,

$$(dE/dx)_{MPV}(\beta\gamma) = \frac{p_1}{\beta^{p_3}} \ln(1 + [p_2 \beta\gamma]^{p_5}) - p_4 \quad (7)$$

which performs well in the range $0.3 < \beta\gamma < 1.5$. This range includes the expected range of $\beta\gamma$ for the particles targeted for this search, with $\beta\gamma \approx 2.0$ for lower mass particles ($O(100 \text{ GeV})$) and up to $\beta\gamma \approx 0.5$ for higher mass particles ($O(1000 \text{ GeV})$). The parameters, p_i , are fit using a 2015 data sample of low-momentum pions, kaons, and protons as described in Ref. [78]. Figure 69 shows the two-dimensional distribution of dE/dx and momentum along with the above fitted values for $(dE/dx)_{MPV}$.

The above equation (7) is then numerically inverted to estimate $\beta\gamma$ and the mass for each candidate track. In simulated signal events, the mean of this mass value reproduces the generated mass up to around 1800 GeV to within 3%, and a 3% shift is applied to correct for this difference. The mass distributions prior to this correction are shown for a few stable mass points in Figure 70. The large widths of these distributions come from the high variability in energy deposits in the pixel detector as well as the uncertainty on momentum measurements at high momentum, but the means converge to the expected values.

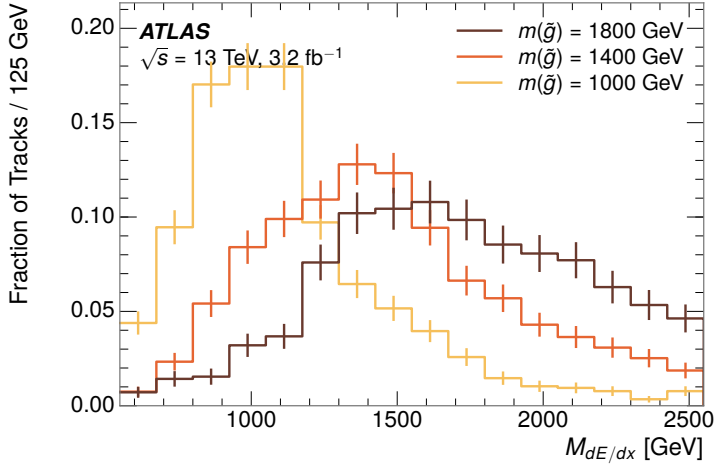


Figure 70: The distribution of mass estimated using dE/dx for simulated stable R-Hadrons with masses between 1000 and 1600 GeV.

2366 This analysis evaluates expected yields and the resulting cross sectional limits
 2367 using windows in this mass variable. The windows are formed by fitting mass
 2368 distributions in simulated signal events like those in Figure 70 to Gaussian distri-
 2369 butions and taking all events that fall within $\pm 1.4\sigma$ of the mean. As can be seen
 2370 in Figure 70, typical values for this width are $\sigma \approx 300 - 500$ GeV depending on
 2371 the generated mass.

2372 11.5 EFFICIENCY

2373 The numbers of events passing each requirement through ionization are shown
 2374 in Table 7 for the full 2015 dataset and a simulated 1600 GeV, 10 ns lifetime R-
 2375 Hadron sample. The table highlights the overall acceptance \times efficiency for sig-
 2376 nal events, which for this example is 19%. Between SM rejection and ionization,
 2377 this signal region reduces the background of tracks which pass the kinematic
 2378 requirements down by an additional factor of almost 2000.

2379 There is a strong dependence of this efficiency on lifetime and mass, with effi-
 2380 ciencies dropping to under 1% at low lifetimes. Figure 71 shows the dependence
 2381 on both mass and lifetime for all signal samples considered in this search. The
 2382 dependence on mass is relatively slight and comes predominantly from the in-
 2383 creasing fraction of R-Hadrons which pass the ionization cut with increasing
 2384 mass. The trigger and E_T^{miss} requirements are most efficient for particles that
 2385 decay before reaching the calorimeters. However, the chance of a particle to be
 2386 reconstructed as a high-quality track decreases significantly at low lifetimes as
 2387 the particle does not propagate sufficiently through the inner detector. These
 2388 effects lead to a maximum in the selection efficiency for lifetimes around 10-30
 2389 ns.

2390 The inefficiency of this signal region at short lifetimes comes almost exclu-
 2391 sively from an acceptance effect, in that the particles do not reach the necessary

Selection	Exp. Signal Events	Observed Events in 3.2 fb^{-1}
Generated	26.0 ± 0.3	
E_T^{miss} Trigger	24.8 ± 0.3 (95%)	
$E_T^{\text{miss}} > 130 \text{ GeV}$	23.9 ± 0.3 (92%)	
Track Quality and $p_T > 50$	10.7 ± 0.2 (41%)	368324
Isolation Requirement	9.0 ± 0.2 (35%)	108079
Track $p > 150 \text{ GeV}$	6.6 ± 0.2 (25%)	47463
$M_T > 130 \text{ GeV}$	5.8 ± 0.2 (22%)	18746
Electron and Hadron Veto	5.5 ± 0.2 (21%)	3612
Muon Veto	5.5 ± 0.2 (21%)	1668
Ionization Requirement	5.0 ± 0.1 (19%)	11

Table 7: The expected number of events at each level of the selection for metastable 1600 GeV , 10 ns R-Hadrons, along with the number of events observed in data, for 3.2 fb^{-1} . The simulated yields are shown with statistical uncertainties only. The total efficiency \times acceptance is also shown for the signal.

2392 layers of the SCT. This can be seen more clearly by defining a fiducial region
 2393 which includes events with at least one R-Hadron that is produced with non-
 2394 zero charge, $p_T > 50 \text{ GeV}$, $p > 150 \text{ GeV}$, $|\eta| < 2.5$, and a decay distance greater
 2395 than 37 cm in the transverse plane. At short (1 ns) lifetimes, the acceptance into
 2396 this region is as low as 4%. Once this acceptance is accounted for, the selection
 2397 efficiency ranges from 25% at lifetimes of 1 ns up to 45% at lifetimes of 10 ns.

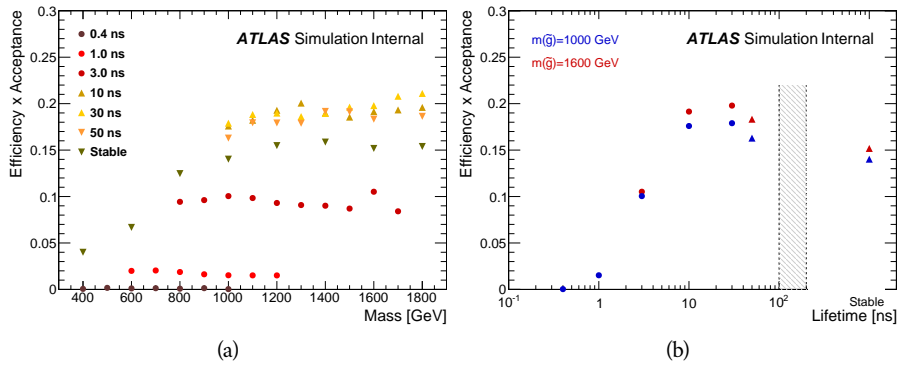


Figure 71: The acceptance \times efficiency as a function of R-Hadron (a) mass and (b) lifetime. (a) shows all of the combinations of mass and lifetime considered in this search, and (b) highlights the lifetime dependence for 1000 GeV and 1600 GeV R-Hadrons.

2398

2399 BACKGROUND ESTIMATION

2400 The event selection discussed in the previous section focuses on detector signa-
 2401 tures, emphasizing a single high-momentum, highly-ionizing track. That track
 2402 is then required to be in some way inconsistent with the expected properties
 2403 of SM particles, with various requirements designed to reject jets, hadrons,
 2404 electrons, and muons (Section 11.3). Therefore the background for this search comes
 2405 entirely from reducible backgrounds that are outliers of various distributions in-
 2406 cluding dE/dx , f_{EM} , and p_T^{Cone} . The simulation can be tuned in various ways to
 2407 do an excellent job of modeling the average properties of each particle type [79],
 2408 but it is not necessarily expected to accurately reproduce outliers. For this rea-
 2409 sons, the background estimation used for this search is estimated entirely using
 2410 data.

2411 12.1 BACKGROUND SOURCES

2412 SM charged particles with lifetimes long enough to form tracks in the inner de-
 2413 tector can be grouped into three major categories based on their detector inter-
 2414 actions: hadrons, electrons, and muons. Every particle that enters into the back-
 2415 ground for this search belongs to one of these types. Relatively pure samples of
 2416 tracks from each of these types can be formed in data by inverting the various
 2417 rejection techniques in Section 11.3. Specifically, muons are selected requiring
 2418 medium muon identification, electrons requiring $E/p > 1.0$ and $f_{\text{EM}} > 0.95$,
 2419 and hadrons requiring $E/p > 1.0$ and $f_{\text{EM}} < 0.95$.

2420 Figure 72 shows the distributions of momentum and dE/dx for these cate-
 2421 gories in data, after requiring the event level selection as well as the track re-
 2422 quirements on p_T , hits, and N_{split} , as discussed in Section 11.2. Simulated signal
 2423 events are included for reference. These distribution are only illustrative of the
 2424 differences between types, as the rejection requirements could alter their shape.
 2425 This is especially significant for momentum which enters directly into E/p and
 2426 can indirectly affect muon identification. However the various types show clear
 2427 differences in both distributions. The distributions of momentum are not nec-
 2428 cessarily expected to match between the various types because the production
 2429 mechanisms for each type result in different kinematic distributions. dE/dx is
 2430 also different between types because of incomplete isolation; although the re-
 2431 quirement on N_{split} helps to reduce the contribution of nearby particles it does
 2432 not completely remove the effect of overlaps. Muons are better isolated because
 2433 they do not have the additional particle from hadronization present for hadrons
 2434 and they are significantly less likely do interact with the detector and produce
 2435 secondary particles compared to hadrons and electrons. Thus muons have the
 2436 smallest fraction of dE/dx above the threshold of $1.8 \text{ MeVg}^{-1}\text{cm}^2$; hadrons and
 2437 electrons have a larger fraction above this threshold.

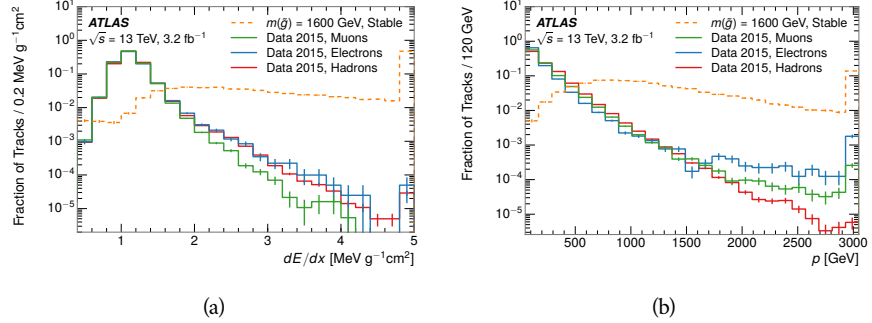


Figure 72: The distribution of (a) dE/dx and (b) momentum for tracks in data and simulated signal after requiring the event level selection and the track selection on p_T , hits, and N_{split} . Each sub-figure shows the normalized distributions for tracks classified as hadrons, electrons, and muons in data and R-Hadrons in the simulated signal.

2438 It is difficult to determine what fraction of each particle type enters into the fi-
 2439 nal signal region. The background method will not have significant dependence
 2440 on the relative contributions of each species, but it is useful to understand the
 2441 differences between each when considering the various tests of the method.

2442 12.2 PREDICTION METHOD

2443 The data-driven background estimation relies on the independence between ion-
 2444 ization and other kinematic variables in the event. For standard model particles
 2445 with momenta above 50 GeV, dE/dx is not correlated with momentum; though
 2446 there is a slight relativistic rise as momentum increases, the effect is small com-
 2447 pared to the width of the distribution of ionization energy deposits.. So, the
 2448 proposed method to estimate the mass distribution of the signal region is to use
 2449 momentum from a track with low dE/dx (below the threshold value) and to com-
 2450 bine it with a random dE/dx value from a dE/dx template. The resulting track is
 2451 just as likely as the original, so a number of such random generations provide the
 2452 expected distributions of momentum and ionization. These are then combined
 2453 using the parametrization described in Section 11.4.1 to form a distribution of
 2454 mass for the signal region.

2455 Algorithmically this method is implemented by forming two distinct Control
 2456 Regions (**CR**s). The first **CR**, CR1, is formed by applying the entire event selec-
 2457 tion from Chapter 11 up to the dE/dx and mass requirements. The dE/dx re-
 2458 quirement is instead inverted for this region. Because of the independence of
 2459 dE/dx , the tracks in this control region have the same kinematic distribution
 2460 as the tracks in the signal region, and are used to measure a two-dimensional
 2461 template of p and η . The second **CR**, CR2, is formed from the event selection
 2462 through the dE/dx requirement, but with an inverted E_T^{miss} requirement. The
 2463 tracks in this control region are expected to have similar dE/dx distributions to
 2464 the signal region before the ionization requirement, and so this region is used to
 2465 measure a two-dimensional template of dE/dx and η .

2466 The contribution of any signal to the control regions is minimized by the in-
 2467 verted selection requirements. Only less than 10% of simulated signal events
 2468 have either dE/dx or E_T^{miss} below the threshold values in the original signal re-
 2469 gion, while the backgrounds are significantly enhanced by inverting those re-
 2470 quirements. The signal contamination is less than 1% in both control regions
 2471 for all of the simulated masses and lifetimes considered in this analysis.

2472 With those measured templates, the shape of the mass estimation is generated
 2473 by first selecting a random (p , η) combination from CR1. This momentum
 2474 value is combined with a dE/dx value taken from the appropriate distribution
 2475 of dE/dx for the selected η from CR2. The use of η in both random samplings
 2476 controls for any correlation between p , dE/dx , and η . Those values are then
 2477 used to calculate a mass in the same way that is done for regular tracks in data,
 2478 see Section 11.4.1. As this procedure includes all dE/dx values, the cut at 1.8
 2479 MeVg $^{-1}$ cm 2 is then enforced to fully model the signal region. The generated
 2480 mass distribution is then normalized by scaling the background estimate to the
 2481 data in the region $M < 160$ GeV, where signals of this type have already been
 2482 excluded [63]. This normalization uses the distributions of mass generated with-
 2483 out the ionization requirement.

2484 The statistical uncertainties on these background distributions are calculated
 2485 by independently fluctuating each bin of the input templates according to their
 2486 Poisson uncertainties. These fluctuations are repeated a large number of times,
 2487 and the uncertainty on the resulting distribution is taken as the root mean square
 2488 (RMS) deviation of the fluctuations from the average. As the procedure uses one
 2489 million random combinations to generate the distributions, The statistical un-
 2490 certainty from the actual random generations is negligible compared to the un-
 2491 certainty from measuring the templates.

2492 12.3 VALIDATION

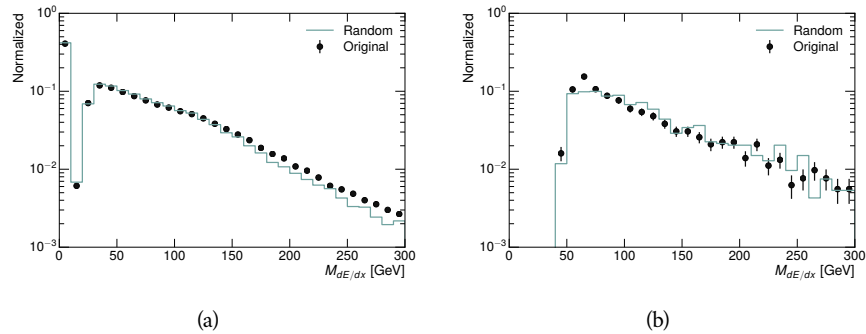
2493 The validity of the background estimation technique can be evaluated in both
 2494 data and simulation. The underlying assumption that random combinations of
 2495 dE/dx and momentum can predict a mass distribution in an orthogonal region
 2496 can be tested using simulated samples where concerns like multiple particle types
 2497 can be controlled. Using the same technique in another set of signal-depleted
 2498 regions in data then extends this confidence to the more complicated case where
 2499 several particle species are inherently included.

2500 12.3.1 CLOSURE IN SIMULATION

2501 The first test of the procedure is done using a simulated sample of $W \rightarrow \mu\nu$
 2502 decays. These types of events provide the ingredients required to test the back-
 2503 ground estimate, E_T^{miss} and isolated tracks, with high statistics. In this example
 2504 there is no signal, so simulated events in the orthogonal CRs are used to estimate
 2505 the shape of the mass distribution of the simulated events in the signal region. To
 2506 reflect the different topology for W boson decays, the CRs use slightly modified
 2507 definitions. In all CRs, the requirement of $p > 150$ GeV and the SM rejection

2508 requirements are removed. Additionally, for the signal region the requirement
 2509 on E_T^{miss} is relaxed to 30 GeV and the corresponding inverted requirement on
 2510 CR2 is also set at 30 GeV.

2511 With these modified selections, the simulated and randomly generated distri-
 2512 butions of $M_{dE/dx}$ are shown in Figure 73. This figure includes the mass distri-
 2513 butions before and after the requirement on dE/dx , which significantly shapes
 2514 the distributions. In both cases the background estimation technique repro-
 2515 duces the shape of $M_{dE/dx}$ in the signal region. There is a small difference in the pos-
 2516 itive tail of the mass distribution prior to the ionization cut, where the random
 2517 events underestimate the fraction of tracks with mass above 150 GeV by about
 2518 20%. After the ionization requirement, however, this discrepancy is not present
 2519 and the two distributions agree to within statistical uncertainties.



2520 Figure 73: The distribution of $M_{dE/dx}$ (a) before and (b) after the ionization requirement
 2521 for tracks in simulated W boson decays and for the randomly generated back-
 2522 ground estimate.

2523 This ability to reproduce the shape of the mass distribution in simulated events
 2524 shows that the technique works as expected. No significant biases are acquired
 2525 in using low dE/dx events to select kinematic templates or in using low E_T^{miss}
 2526 events to select ionization templates, as either would result in a mismodeling of
 the shape of the mass distribution. The simulated events contain only one par-
 ticle type, however, so this test only establishes that the technique works well
 when the the CRs are populated by exactly the same species.

2527 12.3.2 VALIDATION REGION IN DATA

2528 The second test of the background estimate is performed using data in an or-
 2529 thogonal validation region. The validation region, and the corresponding CRs,
 2530 are formed using the same selection requirements as in the nominal method but
 2531 with a modified requirement on momentum, $50 < p[\text{GeV}] < 150$. This allows
 2532 the technique to be checked in a region with very similar properties but where
 2533 the signal is depleted, as the majority of the signal has momentum above 150
 2534 GeV while the backgrounds are enhanced below that threshold. Any biases on
 2535 the particle composition of the CRs for the signal region will be reflected in the
 2536 CRs used to estimate the mass distribution in the validation region.

2537 Figure 74 shows the measured and randomly generated mass distributions for
 2538 data before and after the ionization requirement. The background estimate does
 2539 an excellent job of modeling the actual background before the ionization require-
 2540 ment, with good agreement to within the statistical uncertainties out to the limit
 2541 of the mass distribution. There are very few events in the validation region after
 2542 the ionization requirement, but the few observed events are consistent with the
 2543 background prediction. The good agreement in this validation region provides
 2544 a confirmation that the technique works even in the full-complexity case with
 2545 multiple particle types entering the distributions. Any bias from changes in par-
 2546 ticle composition between regions is small compared to statistical uncertainties.

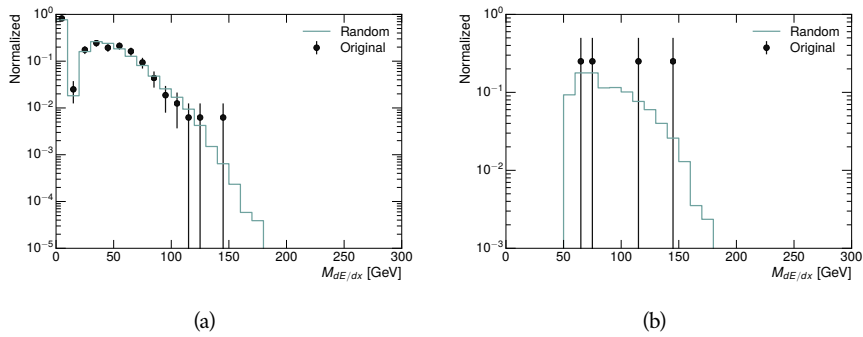


Figure 74: The distribution of $M_{dE/dx}$ (a) before and (b) after the ionization require-
 ment for tracks in the validation region and for the randomly generated back-
 ground estimate.

2547

2548 SYSTEMATIC UNCERTAINTIES AND RESULTS

2549 13.1 SYSTEMATIC UNCERTAINTIES

2550 A number of systematic uncertainties affect the interpretation of the results of
 2551 the search. These uncertainties can broken down into two major categories,
 2552 those which affect the estimate of the background using data and those which
 2553 affect the measurement of the signal yield estimated with simulated events. The
 2554 total measured systematic uncertainties are 7% for the background estimation
 2555 and approximately 32% for the signal yield depending on lifetime. These system-
 2556atic uncertainties are expected to be small compared to the statistical fluctuations
 2557 of the measured yields so that measured cross-sectional limits will be dominated
 2558 by statistical uncertainties. The following sections describe each source of sys-
 2559 tematic uncertainty for each of the two types.

2560 13.1.1 BACKGROUND ESTIMATE

2561 The systematic uncertainties on the background estimate come primarily from
 2562 considering alternative methods for generating the background distributions.
 2563 These uncertainties are small compared to the statistical uncertainties on the
 2564 background estimate which come from the limited statistics in measuring the
 2565 template distributions, as described in Section 12.2. They are summarized in
 2566 Table 8.

Source of Uncertainty:	Value [%]
Analytic Description of dE/dx	4.0
Muon Fraction (Stable Region only)	3.0
IBL Ionization Correction	3.8
Normalization	3.0
Total (Metastable Region):	6.3
Total (Stable Region):	7.0

Table 8: A summary of the sources of systematic uncertainty for the data-driven back-
 ground in the signal region. If the uncertainty depends on the mass, the maxi-
 mum values are reported.

2567 13.1.1.1 ANALYTIC DESCRIPTION OF DE/DX

2568 The background estimate uses a binned template distribution to estimate the
 2569 dE/dx of tracks in the signal region, as described in Section 12.2. It is also possi-

ble to fit that measured distribution to a functional form to help smooth the distribution in the tails of dE/dx where the template is driven by a small number of tracks. Both Landau convolved with a Gaussian and Crystal Ball functions are considered as the functional form and used to re-estimate the background distribution. The deviations compared to the nominal method are found to be 4%, and this is taken as a systematic uncertainty to cover the inability carefully predict the contribution from the long tail of dE/dx where there are few measurements available in data.

2578 13.1.1.2 MUON FRACTION

2579 The stable region of the analysis explicitly includes tracks identified as muons,
 2580 which have a known difference in their dE/dx distributions compared to non-
 2581 muon tracks (Section 12.1). To account for a difference in muon fraction be-
 2582 tween the background region and the signal region for this selection, the dE/dx
 2583 templates for muons and non-muons are measured separately and then the rel-
 2584 ative fraction of each is varied in the random generation. The muon fraction
 2585 is varied by its statistical uncertainty and the resulting difference of 3% in back-
 2586 ground yield is taken as the systematic uncertainty.

2587 13.1.1.3 IBL CORRECTIONS

2588 The IBL, described in Section 6.3.1, received a significant dose of radiation during
 2589 the data collection in 2015. The irradiation can cause a drift in the frontend
 2590 electronics and thus alter the dE/dx measurement which includes the ToT output
 2591 by the IBL. These effects are corrected for in the nominal analysis by scaling the
 2592 dE/dx measurements by a constant factor derived for each run to match the
 2593 average dE/dx value to a reference run where the IBL was known to be stable
 2594 to this effect. However, this corrective factor does not account for inter-run
 2595 variations. To account for this potential drift of dE/dx , the correction procedure
 2596 is repeated by varying the corrections up and down by the maximal run-to-run
 2597 variation from the full data-taking period, which results in an uncertainty of
 2598 3.8%.

2599 13.1.1.4 NORMALIZATION

2600 As described in Section 12.2, the generated distribution of masses is normalized
 2601 in a shoulder region ($M < 160$ GeV) where signals have been excluded by pre-
 2602 vious analyses. That normalization factor is varied by its statistical uncertainty
 2603 and the resulting fluctuation in the mass distribution of 3% is taken as a system-
 2604 atic uncertainty on the background estimate.

2605 13.1.2 SIGNAL YIELD

2606 The systematic uncertainties on the signal yield can be divided into three cate-
 2607 gories; those on the simulation process, those on the modeling of the detector
 2608 efficiency or calibration, and those affecting the overall signal yield. They are
 2609 summarized in Table 8. The largest uncertainty comes from the uncertainty on

2610 the production cross section for gluinos, which is the dominant systematic un-
 2611 certainty in this analysis.

Source of Uncertainty	-[%]	+[%]
ISR Modeling (Metastable Region)	1.5	1.5
ISR Modeling (Stable Region)	14	14
Pile-up Reweighting	1.1	1.1
Trigger Efficiency Reweighting	0.9	0.9
E_T^{miss} Scale	1.1	2.2
Ionization Parametrization	7.1	0
Momentum Parametrization	0.3	0.0
Electron Rejection	0.0	0.0
Hadron Rejection	0.0	0.0
μ Identification	4.3	4.3
Luminosity	5	5
Signal size uncertainty	28	28
Total (Metastable Region)	30	29
Total (Stable Region)	33	32

Table 9: A summary of the sources of systematic uncertainty for the simulated signal yield. The uncertainty depends on the mass and lifetime, and the maximum negative and positive values are reported in the table.

2612 13.1.2.1 ISR MODELING

2613 As discussed in Section 10.2, MadGraph is expected to reproduce the distribution
 2614 of ISR in signal events more accurately than the nominal Pythia samples. The
 2615 analysis reweights the distribution of ISR in the simulated signal events to match
 2616 the distribution found in generated MadGraph samples. This has an effect on the
 2617 selection efficiency in the signal samples, where ISR contributes to the generation
 2618 of E_T^{miss} . To account for the potential inaccuracy on the simulation of ISR at high
 2619 energies, half of the difference between the signal efficiency with the reweighted
 2620 distribution and the original distribution is taken as a systematic uncertainty.

2621 13.1.2.2 PILEUP REWEIGHTING

2622 The simulated events were generated prior to data collection with an estimate of
 2623 the average number of interactions per bunch crossing. This estimate does not
 2624 match the value of pileup during actual data collection, but a large fraction of the
 2625 simulated events would be discarded in order to match the distribution in data.
 2626 Therefore the simulated signal events are not reweighted for pileup by default
 2627 in the analysis. The effect of the pileup on signal efficiency is not expected to
 2628 depend on the mass or lifetime of the generated signal events, which allows all

of the generated signal events to be used together to assess the pileup dependence.
 To account for the potential effect of the difference in the number of interactions per bunch crossing between data and simulation, the difference in yield between the nominal signal events and the reweighted events averaged over all masses and lifetimes is taken as a systematic uncertainty on the yield for each mass and lifetime (1.1%).

13.1.2.3 TRIGGER EFFICIENCY REWEIGHTING

As described in Section 11.2, the selection for this analysis does not require a sufficiently large value of E_T^{miss} to be above the plateau of trigger efficiency. Therefore, some signal events which would otherwise pass the event selection can be excluded because of the trigger requirement. These effects can be difficult to estimate in simulation, and thus are constrained by comparing data and simulated events in an alternative W boson region which uses decays to muons to find a relatively pure sample of events with missing energy. The trigger efficiency for data and simulated W events are shown in Figure 75. The comparison between data and MC in this region constrains the simulation of the trigger efficiency. The simulated signal events are reweighted by the ratio of data to simulation in the W boson decays, while the difference between the data and simulation in those decays is taken as a systematic uncertainty. This results in an uncertainty of only 0.9% as the majority of events are well above the plateau and the disagreement between data and simulation is small even below that plateau.

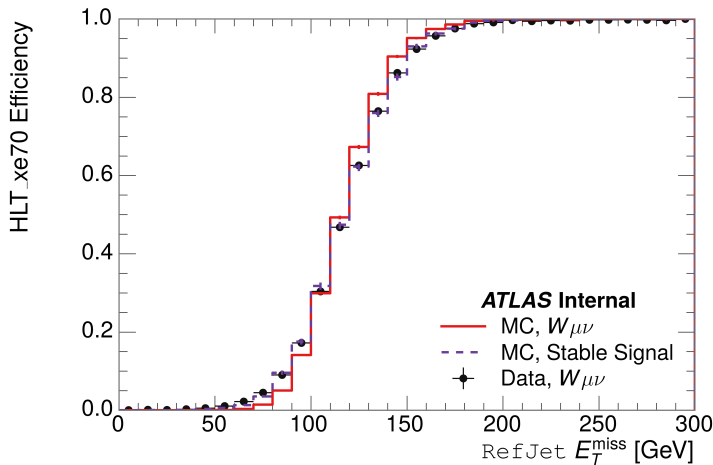


Figure 75: The trigger efficiency for the HLT_xe70 trigger requirement as a function of Calorimeter E_T^{miss} for simulated data events with a W boson selection. Simulated signal events and simulated W boson events are also included.

13.1.2.4 MISSING TRANSVERSE MOMENTUM SCALE

The ATLAS Combined Performance (CP) group provides a default recommendation for systematic variations of jets and missing energy (**note: I'm not quite sure what to cite for this - I don't see any papers from the jet/met group**

Systematic Variation	-[%]	+[%]
JET_GroupedNP_1	-0.7	1.3
JET_GroupedNP_2	-0.7	1.2
JET_GroupedNP_3	-0.5	1.3

Table 10: Example of the contributing systematic variations to the total systematic for the E_T^{miss} Scale, as measured in a 1200 GeV, Stable R-Hadron signal sample.

2654 **after this was implemented).** These variations enter into this analysis only in
 2655 the requirement on E_T^{miss} . The effect of the measured scale of E_T^{miss} is evaluated
 2656 by varying the E_T^{miss} scale according to the one sigma variations provided by all
 2657 **CP** recommendations on objects affecting event kinematics in simulated signal
 2658 events. Missing energy is reconstructed from fully reconstructed objects so any
 2659 systematic uncertainties affecting jets, muons, electrons, or the E_T^{miss} soft terms
 2660 are included. The only non-negligible contributions found using this method are
 2661 itemized in Table 10 for an example signal sample (1200 GeV, Stable R-Hadron),
 2662 where the systematic is measured as the relative difference in the final signal ef-
 2663 ficiency after applying the associated variation through the CP tools. The only
 2664 variations that are significant are the grouped jet systematic variations, which
 2665 combine recommended jet systematic uncertainties into linearly independent
 2666 variations.

2667 As the peak of the reconstructed E_T^{miss} distribution in the signal is significantly
 2668 above the current threshold for events which pass the trigger requirement, the
 2669 effect of scale variation is expected to be small, which is consistent with the mea-
 2670 sured systematic of approximately 2%. Events which do not pass the trigger re-
 2671 quirement usually fail because there are no ISR jets in the event to balance the
 2672 R -hadrons' transverse momentum, so the reconstructed E_T^{miss} is low and there-
 2673 fore also expected to be not very sensitive to scale changes.

2674 13.1.2.5 MOMENTUM PARAMETRIZATION

2675 The uncertainty on the signal efficiency from track momentum is calculated us-
 2676 ing the **CP** group recommendations for tracks. In particular, only one recom-
 2677 mended systematic variation affects track momentum, the sagitta bias for q/P .
 2678 This uncertainty is propagated to the final selection efficiency by varying the
 2679 track momentum by the recommended one sigma variation, and the associated
 2680 uncertainty is found to be negligible (0.3%).

2681 13.1.2.6 IONIZATION REQUIREMENT

2682 The dE/dx distributions in data and simulated events have different most prob-
 2683 able values, which is due in part to radiation effects in the detector that are not
 2684 fully accounted for in the simulation. The difference does not affect the mass
 2685 measurement used in this analysis, as independent calibrations are done in sim-
 2686 ulation and in data. However, it does affect the efficiency of the high dE/dx
 2687 selection requirement. To calculate the size of the effect on the signal efficiency,

2688 the dE/dx distribution in signal simulation is scaled by a scale factor obtained
 2689 from comparing the dE/dx distribution of inclusive tracks in data and in sim-
 2690 ulation. The difference in efficiency for this sample with a scaled dE/dx dis-
 2691 tribution, relative to the nominal case, is taken as a systematic uncertainty on
 2692 signal efficiency. The uncertainty is as large as 7% for low masses and falls to a
 2693 negligible effect for large masses.

2694 13.1.2.7 ELECTRON AND JET REJECTION

2695 The systematic uncertainty on the electron rejection is measured by varying the
 2696 EM fraction requirement significantly, from 0.95 to 0.9. This is found to have
 2697 a less than 0.04% effect on signal acceptance, on average, and so is completely
 2698 negligible. Similarly, the uncertainty on jet rejection is measured by tightening
 2699 the E/p requirement from 0.5 to 0.4. This is found to have no effect on signal
 2700 acceptance, so again the systematic is again negligible.

2701 13.1.2.8 MUON VETO

2702 The metastable signal region requires that the candidate tracks are not identi-
 2703 fied as medium muons because the majority of R-Hadrons in the lifetime range
 2704 included in that region do not reach the muon spectrometers before they de-
 2705 cay. However, the exponential tail of the R-Hadron lifetime distribution results
 2706 in some R-Hadrons traversing the muon spectrometer. These can still fail the
 2707 muon medium identification because they can fail on the requirement on the
 2708 number of precision hits required to pass the loose selection because they ar-
 2709 rive late to the muon spectrometer. This can be seen in Figure 76, which shows
 2710 the efficiency of the muon veto as a function of $1/\beta$, for two simulated stable
 2711 R-Hadron samples.

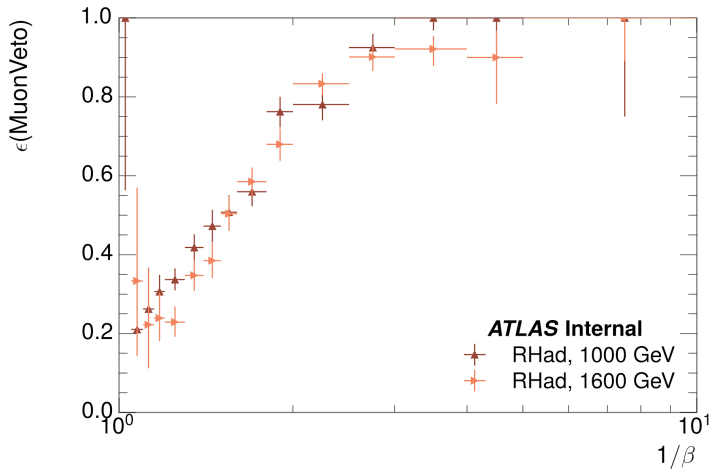


Figure 76: The efficiency of the muon veto for R -hadrons of two different masses, as a function of $\frac{1}{\beta}$ for simulated R-Hadron tracks.

2712 Thus, the efficiency of the muon veto depends on the timing resolution of
 2713 the spectrometer, so an uncertainty is applied to the signal efficiency to cover

2714 differences in timing resolution between data and simulation. First, a sample of
 2715 $Z \rightarrow \mu\mu$ events is selected in data in which one of the muons has a late arrival
 2716 time measured in the MDT. Then the reconstructed β distribution is compared
 2717 to the distribution in simulated $Z \rightarrow \mu\mu$ events; the difference between these
 2718 two distributions reflects the difference in timing resolution between data and
 2719 simulation. To emulate this difference in simulated signal events, the magnitude
 2720 of the difference is used to scale and shift the true β distribution of R-Hadrons in
 2721 simulation. Signal events are then reweighted based on this varied β distribution,
 2722 and the difference in the efficiency of the muon veto selection is compared with
 2723 the nominal and reweighted true β distributions. The difference in muon veto
 2724 efficiency is taken as a systematic uncertainty of the muon veto.

2725 The comparison of reconstructed β between data and simulation is performed
 2726 separately in the barrel, transition, and endcap regions of the spectrometer, and
 2727 the reweighting of the true β distribution in signal is done per region. The com-
 2728 parison of average reconstructed MDT β between data and simulation for the
 2729 barrel region is shown in Figure 77 for $Z \rightarrow \mu\mu$ events. As expected, The uncer-
 2730 tainty is found to be negligible for R-hadrons with short lifetimes, and is only
 2731 significant for lifetimes above 30 ns.

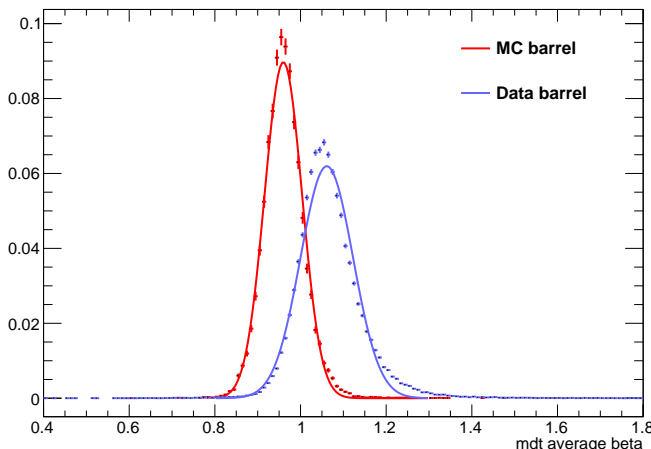


Figure 77: The average reconstructed MDT β distribution for $Z \rightarrow \mu\mu$ events in which
 one of the muons is reconstructed as a slow muon, for both data and simula-
 tion. A gaussian fit is superimposed.

2732 13.1.2.9 LUMINOSITY

2733 The luminosity uncertainty is provided by a luminosity measurement on ATLAS
 2734 and was measured to be 5% at the time of the publication of this analysis.

2735 13.1.2.10 SIGNAL SIZE

2736 As discussed in Section 10.2, the signal cross sections are calculated at NLO in the
 2737 strong coupling constant with a resummation of soft-gluon emission at NLL. The
 2738 uncertainties on those cross sections are between 14% to 28% for the R-Hadrons

Selection Region	Expected Background	Data
Stable	$17.2 \pm 2.6 \pm 1.2$	16
Metastable	$11.1 \pm 1.7 \pm 0.7$	11

Table 11: The estimated number of background events and the number of observed events in data for the specified selection regions prior to the requirement on mass. The background estimates show statistical and systematic uncertainties.

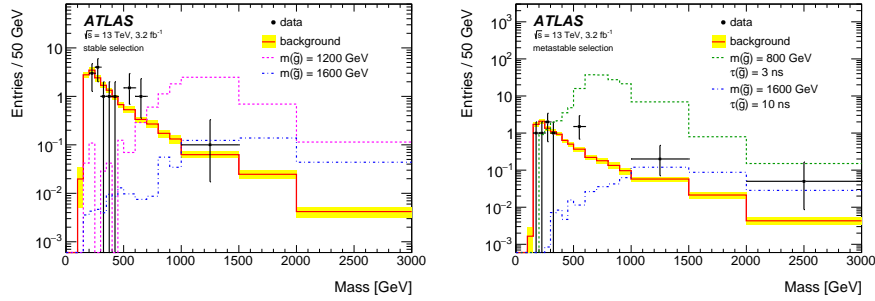


Figure 78: The observed mass distribution of events in data and the generated background distribution in (a) the stable and (b) the metastable signal region. A few example simulated signal distributions are superimposed.

in the range of 400 to 1800 GeV [75, 76], where the uncertainty increases with the mass.

13.2 FINAL YIELDS

This full analysis was performed using the 3.2 fb^{-1} from the 2015 data-taking. Using the selections discussed in Chapter 11, sixteen events were observed in the stable signal region and eleven events were observed in the metastable signal region, prior to requirements on the candidate track mass. The background estimate discussed in Chapter 12 predicts $17 \pm 2.6(\text{stat}) \pm 1.2(\text{syst})$ events for the stable region and $11.1 \pm 1.7(\text{stat}) \pm 0.7(\text{syst})$ events for the metastable region. These counts are summarized in Table 11.

The mass estimated using dE/dx (Section 11.4.1) provides the final discriminating variable, where the signal would be expected as an excess in the falling exponential tail of the expected background. The observed distribution of masses is shown in Figure 78, along with the predicted distribution from the background estimate for each signal region. Both include a few example simulated signal distributions, which show the scale of an excess were the R-Hadron signals present. There is no statistically significant evidence of an excess in the data over the background estimation. From this distribution it is clearly possible to rule out signals with lower masses, around 1200 GeV, which have larger cross sections.

2758 13.3 CROSS SECTIONAL LIMITS

2759 Because there is no observed significant excess of events in the signal region, this
 2760 analysis sets upper limits on the allowed cross section for R-Hadron production.
 2761 These limits are set for each mass point by counting the observed events in data,
 2762 along with the expected background and simulated signal events, in windows of
 2763 mass. The mass windows are formed by fitting the distribution of signal events to
 2764 a Gaussian distribution, and the window is then $\pm 1.4\sigma$ around the center of that
 2765 Gaussian. Two examples of the windows formed by this procedure are shown
 2766 in Tables 12-13, for the stable and 10 ns working points. The corresponding
 2767 counts of observed data, expected background, and simulated signal for those
 2768 same working points are shown in Tables 14-15. Appendix B includes the mass
 2769 windows and counts for all of the considered signal points.

$m(\tilde{g})$ [GeV]	Left Extremum [GeV]	Right Extremum [GeV]
1000	655	1349
1100	734	1455
1200	712	1631
1300	792	1737
1400	717	1926
1500	815	2117
1600	824	2122
1700	900	2274
1800	919	2344

Table 12: The left and right extremum of the mass window for each generated mass point with a 10 ns lifetime.

$m(\tilde{g})$ [GeV]	Left Extremum [GeV]	Right Extremum [GeV]
800	627	1053
1000	726	1277
1200	857	1584
1400	924	1937
1600	993	2308
1800	1004	2554

Table 13: The left and right extremum of the mass window used for each generated stable mass point.

2770 The 95% confidence level upper limits on the cross sections for a large grid of
 2771 masses (between 800 and 1800 GeV) and lifetimes (between 0.4 and stable) are
 2772 extracted from these counts with the CL_S method using the profile likelihood

$m(\tilde{g})$ [GeV]	Expected Signal	Expected Background	Observed Data
800	462.83 ± 14.86	1.764 ± 0.080	2.0
1000	108.73 ± 3.38	1.458 ± 0.070	1.0
1200	31.74 ± 0.95	1.137 ± 0.060	1.0
1400	10.22 ± 0.29	1.058 ± 0.058	1.0
1600	3.07 ± 0.09	0.947 ± 0.054	1.0
1800	1.08 ± 0.05	0.940 ± 0.054	1.0

Table 14: The expected number of signal events, the expected number of background events, and the observed number of events in data with their respective statistical errors within the respective mass window for each generated stable mass point

$m(\tilde{g})$ [GeV]	Expected Signal	Expected Background	Observed Data
1000	144.48 ± 5.14	1.499 ± 0.069	2.0
1100	73.19 ± 2.61	1.260 ± 0.060	2.0
1200	41.54 ± 1.41	1.456 ± 0.067	2.0
1300	22.58 ± 0.77	1.201 ± 0.058	2.0
1400	12.70 ± 0.42	1.558 ± 0.071	2.0
1500	6.73 ± 0.24	1.237 ± 0.060	2.0
1600	3.90 ± 0.13	1.201 ± 0.058	2.0
1700	2.27 ± 0.07	1.027 ± 0.052	2.0
1800	1.34 ± 0.04	1.019 ± 0.052	2.0

Table 15: The expected number of signal events, the expected number of background events, and the observed number of events in data with their respective statistical errors within the respective mass window for each generated mass point with a lifetime of 10 ns.

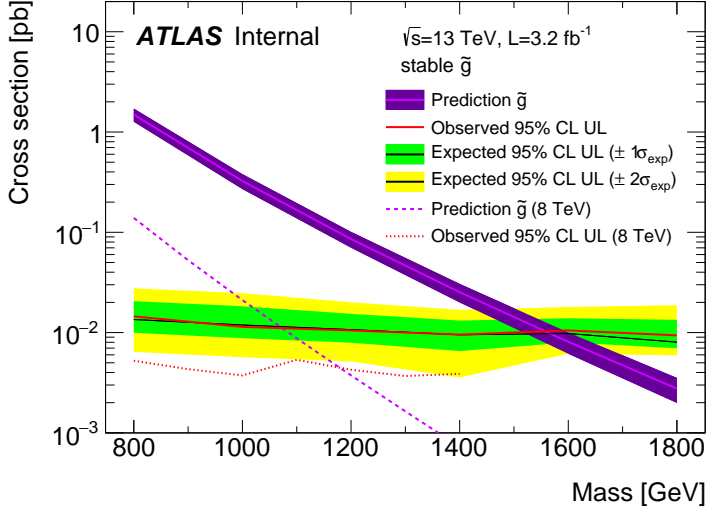


Figure 79: The observed and expected cross section limits as a function of mass for the stable simulated signal. The predicted cross section values for the corresponding signals are included.

ratio as a test statistic [80]. For this procedure, the systematic uncertainties estimated for the signal and background yields are treated as Gaussian-distributed nuisance parameters. The uncertainty on the normalization of the expected background distribution is included in the expected background events. At this point the expected cross section limit is calculated for both the metastable and stable signal region for each lifetime point, and the region with the best expected limit is selected for each lifetime. Using that procedure, the metastable region is used for lifetimes up to and including 30 ns, and the stable region for lifetimes above it.

The resulting cross-sectional upper limits are shown as a function of mass in Figure 79 and Figure 80 for each lifetime considered. The limits are interpolated linearly between each mass point, and the dependence of the limit on the mass is small as the efficiency is relatively constant for large R-Hadron masses. There is however a strong dependence on lifetime, as discussed in Section 11.5, where the probability to form a fully reconstructed track and the kinematic freedom to produce E_T^{miss} result in a local maximum in the limit at 10–30 ns. The figures also include the expected cross section for pair-produced gluino R-Hadrons for reference. For the 10 ns and stable cross section limits, both the observed limit and expected cross section for the Run 1, 8 TeV version of this analysis are included. There the cross sectional limits are lower because of the increased available luminosity, while the signal cross sections were also much lower because of the lower collision energy.

13.4 MASS LIMITS

The cross-sectional limits can then be used to derive a lower mass limit for gluino R-Hadrons by comparing them to the theoretically predicted production cross

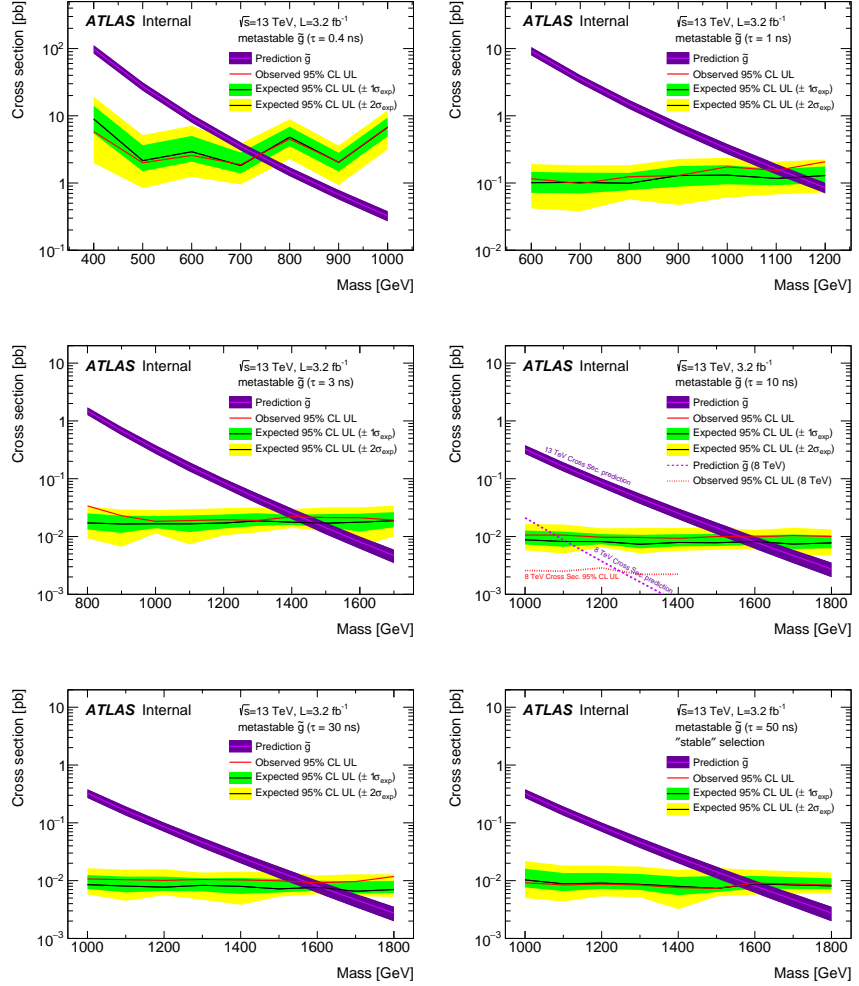


Figure 80: The observed and expected cross section limits as a function of mass for each generated lifetime. The predicted cross section values for the corresponding signals are included.

sections. These mass limits range from only 740 GeV at the lowest lifetimes considered, where the selection efficiency is very low, to up to 1580 GeV at 30 ns where the selection efficiency is maximized. The observed and expected mass limits for each lifetime point are detailed in Table 16, which also lists which selection region was used for each lifetime. These excluded range of masses as a function of lifetime is also shown in Figure 81. The Run 1 limits are included for comparison; the limits have increased by about 200 GeV on average. The search has also improved since the previous incarnation from Run 1 in optimizing the region between 30 GeV and detector-stable lifetimes by introducing the second signal region. The definition of the stable region prevents the significant drop in mass limit that occurred above 30 GeV in the Run 1 analysis.

Selection	τ [ns]	$M_{\text{obs}} > [\text{GeV}]$	$M_{\text{exp}} > [\text{GeV}]$
Metastable	0.4	740	730
"	1.0	1110	1150
"	3.0	1430	1470
"	10	1570	1600
"	30	1580	1620
Stable	50	1590	1590
"	stable	1570	1580

Table 16: The observed and expected 95% CL lower limit on mass for gluino R-Hadrons for each considered lifetime.

13.5 CONTEXT FOR LONG-LIVED SEARCHES

This search plays an important role in the current, combined ATLAS search for long lived particles. The mass limits provided by various ATLAS searches for long-lived gluino R-Hadrons can be seen in Figure 82. This search provides the most competitive limit for lifetimes between 3 ns up through very long lifetimes, where it is still competitive with dedicated searches for stable particles. The limits placed on gluino production are very similar to the limits on promptly decaying models.

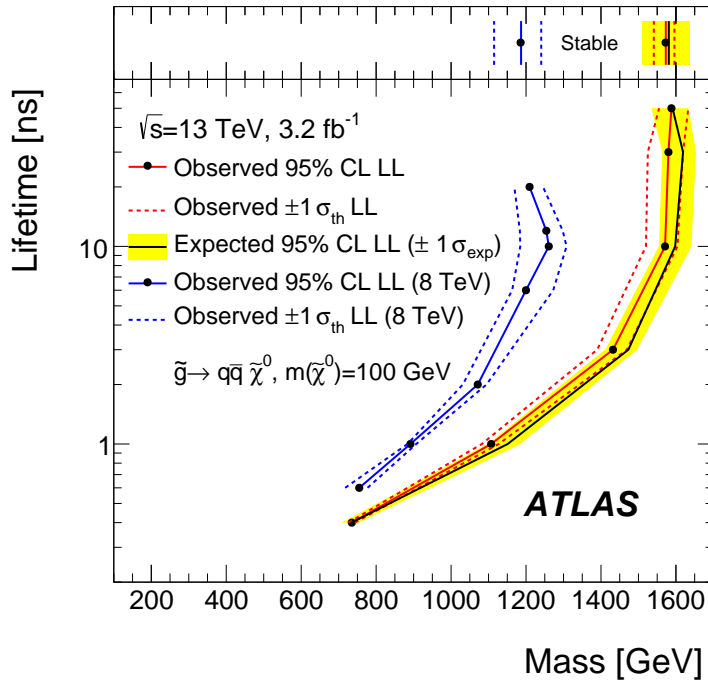


Figure 81: The excluded range of masses as a function of gluino lifetime. The expected lower limit (LL), with its experimental $\pm 1\sigma$ band, is given with respect to the nominal theoretical cross-section. The observed 95% LL obtained at $\sqrt{s} = 8 \text{ TeV}$ [63] is also shown for comparison.

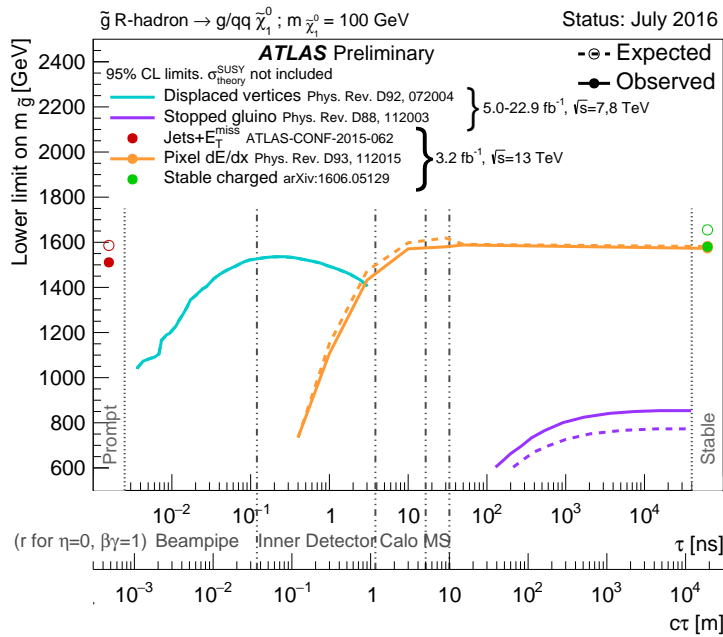


Figure 82: The constraints on the gluino mass as a function of lifetime for a split-supersymmetry model with the gluino R-Hadrons decaying into a gluon or light quarks and a neutralino with mass of 100 GeV. The solid lines indicate the observed limits, while the dashed lines indicate the expected limits. The area below the curves is excluded. The dots represent results for which the particle is assumed to be prompt or stable.

2817

PART VI

2818

CONCLUSIONS

2819

You can put some informational part preamble text here.

14

2820

2821 SUMMARY AND OUTLOOK

2822 14.1 SUMMARY

2823 14.2 OUTLOOK

2824

PART VII

2825

APPENDIX

2826

A

2827

2828 INELASTIC CROSS SECTION

B

2829

2830 EXPANDED R-HADRON YIELDS AND LIMITS

$m(\tilde{g})$ [GeV]	Left Extremum [GeV]	Right Extremum [GeV]
1000	682	1387
1100	763	1478
1200	801	1606
1300	809	1841
1400	861	2011
1500	920	2032
1600	952	2173
1800	1017	2422

Table 17: The left and right extremum of the mass window for each generated mass point with a 50 ns lifetime.

$m(\tilde{g})$ [GeV]	Left Extremum [GeV]	Right Extremum [GeV]
1000	689	1321
1100	746	1513
1200	788	1670
1300	860	1734
1400	833	1925
1500	852	2048
1600	833	2283
1700	946	2379
1800	869	2505

Table 18: The left and right extremum of the mass window for each generated mass point with a 30 ns lifetime.

$m(\tilde{g})$ [GeV]	Left Extremum [GeV]	Right Extremum [GeV]
1000	655	1349
1100	734	1455
1200	712	1631
1300	792	1737
1400	717	1926
1500	815	2117
1600	824	2122
1700	900	2274
1800	919	2344

Table 19: The left and right extremum of the mass window for each generated mass point with a 10 ns lifetime.

$m(\tilde{g})$ [GeV]	Left Extremum [GeV]	Right Extremum [GeV]
800	531	1065
900	576	1165
1000	610	1345
1100	635	1432
1200	663	1563
1300	620	1667
1400	742	1727
1500	761	1937
1600	573	2000
1700	621	2182

Table 20: The left and right extremum of the mass window used for each generated mass point with a lifetime of 3 ns.

$m(\tilde{g})$ [GeV]	Left Extremum [GeV]	Right Extremum [GeV]
600	411	758
700	385	876
800	486	970
900	406	987
1000	408	1136
1100	555	1196
1200	516	1378

Table 21: The left and right extremum of the mass window used for each mass point with a lifetime of 1 ns.

$m(\tilde{g})$ [GeV]	Left Extremum [GeV]	Right Extremum [GeV]
400	204	510
500	295	639
600	288	702
700	323	701
800	190	771
900	277	677
1000	249	688

Table 22: The left and right extremum of the mass window for each generated mass point with a lifetime of 0.4 ns.

$m(\tilde{g})$ [GeV]	Left Extremum [GeV]	Right Extremum [GeV]
800	627	1053
1000	726	1277
1200	857	1584
1400	924	1937
1600	993	2308
1800	1004	2554

Table 23: The left and right extremum of the mass window used for each generated stable mass point.

$m(\tilde{g})$ [GeV]	Expected Signal	Expected Background	Observed Data
1000	131.18 ± 6.35	1.803 ± 0.081	1.0 ± 1.0
1100	71.11 ± 3.35	1.409 ± 0.069	1.0 ± 1.0
1200	37.18 ± 1.75	1.310 ± 0.066	1.0 ± 1.0
1300	20.76 ± 0.95	1.431 ± 0.069	1.0 ± 1.0
1400	12.63 ± 0.57	1.273 ± 0.065	1.0 ± 1.0
1500	6.57 ± 0.29	1.115 ± 0.059	1.0 ± 1.0
1600	3.56 ± 0.16	1.041 ± 0.057	1.0 ± 1.0
1800	1.27 ± 0.05	0.918 ± 0.053	1.0 ± 1.0

Table 24: The expected number of signal events, the expected number of background events, and the observed number of events in data with their respective statistical errors within the respective mass window for each generated mass point with a lifetime of 50 ns.

$m(\tilde{g})$ [GeV]	Expected Signal	Expected Background	Observed Data
1000	144.65 ± 6.34	1.328 ± 0.063	2.0 ± 1.4
1100	75.28 ± 3.27	1.255 ± 0.060	2.0 ± 1.4
1200	40.51 ± 1.75	1.193 ± 0.058	2.0 ± 1.4
1300	20.91 ± 0.93	0.997 ± 0.051	2.0 ± 1.4
1400	11.97 ± 0.51	1.131 ± 0.056	2.0 ± 1.4
1500	6.81 ± 0.28	1.111 ± 0.055	2.0 ± 1.4
1600	4.19 ± 0.16	1.193 ± 0.058	2.0 ± 1.4
1700	2.42 ± 0.09	0.963 ± 0.050	2.0 ± 1.4
1800	1.46 ± 0.05	1.138 ± 0.056	3.0 ± 1.7

Table 25: The expected number of signal events, the expected number of background events, and the observed number of events in data with their respective statistical errors within the respective mass window for each generated mass point with a lifetime of 30 ns.

$m(\tilde{g})$ [GeV]	Expected Signal	Expected Background	Observed Data
1000	144.48 ± 5.14	1.499 ± 0.069	2.0 ± 1.4
1100	73.19 ± 2.61	1.260 ± 0.060	2.0 ± 1.4
1200	41.54 ± 1.41	1.456 ± 0.067	2.0 ± 1.4
1300	22.58 ± 0.77	1.201 ± 0.058	2.0 ± 1.4
1400	12.70 ± 0.42	1.558 ± 0.071	2.0 ± 1.4
1500	6.73 ± 0.24	1.237 ± 0.060	2.0 ± 1.4
1600	3.90 ± 0.13	1.201 ± 0.058	2.0 ± 1.4
1700	2.27 ± 0.07	1.027 ± 0.052	2.0 ± 1.4
1800	1.34 ± 0.04	1.019 ± 0.052	2.0 ± 1.4

Table 26: The expected number of signal events, the expected number of background events, and the observed number of events in data with their respective statistical errors within the respective mass window for each generated mass point with a lifetime of 10 ns.

$m(\tilde{g})$ [GeV]	Expected Signal	Expected Background	Observed Data
800	362.97 ± 14.68	1.841 ± 0.080	5.0 ± 2.2
900	169.20 ± 6.69	1.710 ± 0.076	3.0 ± 1.7
1000	84.78 ± 3.23	1.727 ± 0.076	2.0 ± 1.4
1100	40.06 ± 1.60	1.679 ± 0.075	2.0 ± 1.4
1200	20.06 ± 0.81	1.598 ± 0.072	2.0 ± 1.4
1300	10.76 ± 0.43	1.851 ± 0.080	2.0 ± 1.4
1400	5.52 ± 0.22	1.374 ± 0.064	2.0 ± 1.4
1500	3.16 ± 0.13	1.355 ± 0.064	2.0 ± 1.4
1600	2.13 ± 0.11	2.235 ± 0.093	3.0 ± 1.7
1700	1.10 ± 0.06	1.995 ± 0.085	2.0 ± 1.4

Table 27: The expected number of signal events, the expected number of background events, and the observed number of events in data with their respective statistical errors within the respective mass window for each generated mass point with a lifetime of 3 ns.

$m(\tilde{g})$ [GeV]	Expected Signal	Expected Background	Observed Data
600	431.80 ± 36.60	2.418 ± 0.099	3.0 ± 1.7
700	192.77 ± 15.28	3.267 ± 0.126	3.0 ± 1.7
800	69.63 ± 5.90	2.125 ± 0.089	3.0 ± 1.7
900	28.91 ± 2.59	3.114 ± 0.121	3.0 ± 1.7
1000	13.64 ± 1.22	3.359 ± 0.129	5.0 ± 2.2
1100	6.13 ± 0.57	1.879 ± 0.081	3.0 ± 1.7
1200	3.24 ± 0.30	2.387 ± 0.098	5.0 ± 2.2

Table 28: The expected number of signal events, the expected number of background events, and the observed number of events in data with their respective statistical errors within the respective mass window for each generated mass point with a lifetime of 1 ns.

$m(\tilde{g})$ [GeV]	Expected Signal	Expected Background	Observed Data
400	181.71 ± 75.59	6.780 ± 0.238	4.0 ± 2.0
500	103.88 ± 30.05	4.310 ± 0.160	4.0 ± 2.0
600	28.34 ± 9.34	4.868 ± 0.177	4.0 ± 2.0
700	13.62 ± 4.00	3.908 ± 0.147	4.0 ± 2.0
800	2.75 ± 1.15	9.001 ± 0.308	8.0 ± 2.8
900	2.25 ± 0.71	5.045 ± 0.183	5.0 ± 2.2
1000	0.34 ± 0.19	6.026 ± 0.214	6.0 ± 2.4

Table 29: The expected number of signal events, the expected number of background events, and the observed number of events in data with their respective statistical errors within the respective mass window for each generated mass point with a lifetime of p4 ns.

$m(\tilde{g})$ [GeV]	Expected Signal	Expected Background	Observed Data
800	462.83 ± 14.86	1.764 ± 0.080	2.0 ± 1.4
1000	108.73 ± 3.38	1.458 ± 0.070	1.0 ± 1.0
1200	31.74 ± 0.95	1.137 ± 0.060	1.0 ± 1.0
1400	10.22 ± 0.29	1.058 ± 0.058	1.0 ± 1.0
1600	3.07 ± 0.09	0.947 ± 0.054	1.0 ± 1.0
1800	1.08 ± 0.05	0.940 ± 0.054	1.0 ± 1.0

Table 30: The expected number of signal events, the expected number of background events, and the observed number of events in data with their respective statistical errors within the respective mass window for each generated stable mass point

2831 BIBLIOGRAPHY

- 2832 [1] Lyndon Evans and Philip Bryant. "LHC Machine". In: *JINST* 3 (2008), S08001.
2833 doi: [10.1088/1748-0221/3/08/S08001](https://doi.org/10.1088/1748-0221/3/08/S08001).
- 2834 [2] C Lefevre. "LHC: the guide (English version). Guide du LHC (version anglaise)".
2835 2009. URL: <https://cds.cern.ch/record/1165534>.
- 2836 [3] ATLAS Collaboration. "The ATLAS Experiment at the CERN Large Hadron
2837 Collider". In: *JINST* 3 (2008), S08003. doi: [10.1088/1748-0221/3/08/S08003](https://doi.org/10.1088/1748-0221/3/08/S08003).
- 2838 [4] S. Chatrchyan et al. "The CMS experiment at the CERN LHC". In: *JINST*
2839 3 (2008), S08004. doi: [10.1088/1748-0221/3/08/S08004](https://doi.org/10.1088/1748-0221/3/08/S08004).
- 2840 [5] A. Augusto Alves Jr. et al. "The LHCb Detector at the LHC". In: *JINST* 3
2841 (2008), S08005. doi: [10.1088/1748-0221/3/08/S08005](https://doi.org/10.1088/1748-0221/3/08/S08005).
- 2842 [6] K. Aamodt et al. "The ALICE experiment at the CERN LHC". In: *JINST* 3
2843 (2008), S08002. doi: [10.1088/1748-0221/3/08/S08002](https://doi.org/10.1088/1748-0221/3/08/S08002).
- 2844 [7] K. A. Olive et al. "Review of Particle Physics". In: *Chin. Phys. C* 38 (2014),
2845 p. 090001. doi: [10.1088/1674-1137/38/9/090001](https://doi.org/10.1088/1674-1137/38/9/090001).
- 2846 [8] Daniel Froidevaux and Paris Sphicas. "General-Purpose Detectors for the
2847 Large Hadron Collider". In: *Annual Review of Nuclear and Particle Science*
2848 56.1 (2006), pp. 375–440. doi: [10.1146/annurev.nucl.54.070103.181209](https://doi.org/10.1146/annurev.nucl.54.070103.181209). URL: <http://dx.doi.org/10.1146/annurev.nucl.54.070103.181209>.
- 2849 [9] M Capeans, G Darbo, K Einsweiller, M Elsing, T Flick, M Garcia-Sciveres,
2850 C Gemme, H Pernegger, O Rohne, and R Vuillermet. *ATLAS Insertable B-*
2851 *Layer Technical Design Report*. Tech. rep. CERN-LHCC-2010-013. ATLAS-
2852 TDR-19. 2010. URL: <https://cds.cern.ch/record/1291633>.
- 2853 [10] S Agostinelli et al. "GEANT4: A simulation toolkit". In: *Nucl. Instrum. Meth.*
2854 A 506 (2003), pp. 250–303. doi: [10.1016/S0168-9002\(03\)01368-8](https://doi.org/10.1016/S0168-9002(03)01368-8).
- 2855 [11] ATLAS Collaboration. "A study of the material in the ATLAS inner de-
2856 tector using secondary hadronic interactions". In: *JINST* 7 (2012), P01013.
2857 doi: [10.1088/1748-0221/7/01/P01013](https://doi.org/10.1088/1748-0221/7/01/P01013). arXiv: [1110.6191 \[hep-ex\]](https://arxiv.org/abs/1110.6191).
2858 PERF-2011-08.
- 2859 [12] ATLAS Collaboration. "Electron and photon energy calibration with the
2860 ATLAS detector using LHC Run 1 data". In: *Eur. Phys. J. C* 74 (2014), p. 3071.
2861 doi: [10.1140/epjc/s10052-014-3071-4](https://doi.org/10.1140/epjc/s10052-014-3071-4). arXiv: [1407.5063](https://arxiv.org/abs/1407.5063)
2862 [hep-ex]. PERF-2013-05.
- 2863 [13] ATLAS Collaboration. "A measurement of the calorimeter response to sin-
2864 gle hadrons and determination of the jet energy scale uncertainty using
2865 LHC Run-1 pp -collision data with the ATLAS detector". In: (2016). arXiv:
2866 [1607.08842 \[hep-ex\]](https://arxiv.org/abs/1607.08842). PERF-2015-05.
- 2867
- 2868
- 2869

- 2870 [14] ATLAS Collaboration. “Single hadron response measurement and calorimeter jet energy scale uncertainty with the ATLAS detector at the LHC”. In: *Eur. Phys. J. C* 73 (2013), p. 2305. doi: [10.1140/epjc/s10052-013-2305-1](https://doi.org/10.1140/epjc/s10052-013-2305-1). arXiv: [1203.1302 \[hep-ex\]](https://arxiv.org/abs/1203.1302). PERF-2011-05.
- 2871
2872
2873
- 2874 [15] ATLAS Collaboration. “The ATLAS Simulation Infrastructure”. In: *Eur. Phys. J. C* 70 (2010), p. 823. doi: [10.1140/epjc/s10052-010-1429-9](https://doi.org/10.1140/epjc/s10052-010-1429-9). arXiv: [1005.4568 \[hep-ex\]](https://arxiv.org/abs/1005.4568). SOFT-2010-01.
- 2875
2876
- 2877 [16] T. Sjöstrand, S. Mrenna, and P. Skands. “A Brief Introduction to PYTHIA 8.1”. In: *Comput. Phys. Commun.* 178 (2008), pp. 852–867. doi: [10.1016/j.cpc.2008.01.036](https://doi.org/10.1016/j.cpc.2008.01.036). arXiv: [0710.3820](https://arxiv.org/abs/0710.3820).
- 2878
2879
- 2880 [17] ATLAS Collaboration. *Summary of ATLAS Pythia 8 tunes*. ATL-PHYS-PUB-2012-003. 2012. URL: <http://cds.cern.ch/record/1474107>.
- 2881
- 2882 [18] A.D. Martin, W.J. Stirling, R.S. Thorne, and G. Watt. “Parton distributions for the LHC”. In: *Eur. Phys. J. C* 63 (2009). Figures from the [MSTW Website](#), pp. 189–285. doi: [10.1140/epjc/s10052-009-1072-5](https://doi.org/10.1140/epjc/s10052-009-1072-5). arXiv: [0901.0002](https://arxiv.org/abs/0901.0002).
- 2883
2884
2885
- 2886 [19] A. Sherstnev and R.S. Thorne. “Parton Distributions for LO Generators”. In: *Eur. Phys. J. C* 55 (2008), pp. 553–575. doi: [10.1140/epjc/s10052-008-0610-x](https://doi.org/10.1140/epjc/s10052-008-0610-x). arXiv: [0711.2473](https://arxiv.org/abs/0711.2473).
- 2887
2888
- 2889 [20] A. Ribon et al. *Status of Geant4 hadronic physics for the simulation of LHC experiments at the start of LHC physics program*. CERN-LCGAPP-2010-02. 2010. URL: <http://lcgapp.cern.ch/project/docs/noteStatusHadronic2010.pdf>.
- 2890
2891
2892
- 2893 [21] M. P. Guthrie, R. G. Alsmiller, and H. W. Bertini. “Calculation of the capture of negative pions in light elements and comparison with experiments pertaining to cancer radiotherapy”. In: *Nucl. Instrum. Meth.* 66 (1968), pp. 29–36. doi: [10.1016/0029-554X\(68\)90054-2](https://doi.org/10.1016/0029-554X(68)90054-2).
- 2894
2895
2896
- 2897 [22] H. W. Bertini and P. Guthrie. “News item results from medium-energy intranuclear-cascade calculation”. In: *Nucl. Instr. and Meth. A* 169 (1971), p. 670. doi: [10.1016/0375-9474\(71\)90710-X](https://doi.org/10.1016/0375-9474(71)90710-X).
- 2898
2899
- 2900 [23] V.A. Karmanov. “Light Front Wave Function of Relativistic Composite System in Explicitly Solvable Model”. In: *Nucl. Phys. B* 166 (1980), p. 378. doi: [10.1016/0550-3213\(80\)90204-7](https://doi.org/10.1016/0550-3213(80)90204-7).
- 2901
2902
- 2903 [24] H. S. Fesefeldt. *GHEISHA program*. Pitha-85-02, Aachen. 1985.
- 2904
2905
- 2906 [25] G. Folger and J.P. Wellisch. “String parton models in Geant4”. In: (2003). arXiv: [nucl-th/0306007](https://arxiv.org/abs/nucl-th/0306007).
- 2907
2908
- 2909 [26] N. S. Amelin et al. “Transverse flow and collectivity in ultrarelativistic heavy-ion collisions”. In: *Phys. Rev. Lett.* 67 (1991), p. 1523. doi: [10.1103/PhysRevLett.67.1523](https://doi.org/10.1103/PhysRevLett.67.1523).
- 2910
2911
- 2909 [27] N. S. Amelin et al. “Collectivity in ultrarelativistic heavy ion collisions”. In: *Nucl. Phys. A* 544 (1992), p. 463. doi: [10.1016/0375-9474\(92\)90598-E](https://doi.org/10.1016/0375-9474(92)90598-E).

- 2912 [28] L. V. Bravina et al. “Fluid dynamics and Quark Gluon string model - What
2913 we can expect for Au+Au collisions at 11.6 AGeV/c”. In: *Nucl. Phys. A* 566
2914 (1994), p. 461. doi: [10.1016/0375-9474\(94\)90669-6](https://doi.org/10.1016/0375-9474(94)90669-6).
- 2915 [29] L. V. Bravin et al. “Scaling violation of transverse flow in heavy ion colli-
2916 sions at AGS energies”. In: *Phys. Lett. B* 344 (1995), p. 49. doi: [10.1016/0370-2693\(94\)01560-Y](https://doi.org/10.1016/0370-2693(94)01560-Y).
- 2918 [30] B. Andersson et al. “A model for low-pT hadronic reactions with general-
2919 izations to hadron-nucleus and nucleus-nucleus collisions”. In: *Nucl. Phys.*
2920 *B* 281 (1987), p. 289. doi: [10.1016/0550-3213\(87\)90257-4](https://doi.org/10.1016/0550-3213(87)90257-4).
- 2921 [31] B. Andersson, A. Tai, and B.-H. Sa. “Final state interactions in the (nuclear)
2922 FRITIOF string interaction scenario”. In: *Z. Phys. C* 70 (1996), pp. 499–
2923 506. doi: [10.1007/s002880050127](https://doi.org/10.1007/s002880050127).
- 2924 [32] B. Nilsson-Almqvist and E. Stenlund. “Interactions Between Hadrons and
2925 Nuclei: The Lund Monte Carlo, Fritiof Version 1.6”. In: *Comput. Phys. Com-*
2926 *mun.* 43 (1987), p. 387. doi: [10.1016/0010-4655\(87\)90056-7](https://doi.org/10.1016/0010-4655(87)90056-7).
- 2927 [33] B. Ganhuyag and V. Uzhinsky. “Modified FRITIOF code: Negative charged
2928 particle production in high energy nucleus nucleus interactions”. In: *Czech.*
2929 *J. Phys.* 47 (1997), pp. 913–918. doi: [10.1023/A:1021296114786](https://doi.org/10.1023/A:1021296114786).
- 2930 [34] ATLAS Collaboration. “Topological cell clustering in the ATLAS calorime-
2931 ters and its performance in LHC Run 1”. In: (2016). arXiv: [1603.02934](https://arxiv.org/abs/1603.02934)
[hep-ex].
- 2933 [35] Peter Speckmayer. “Energy Measurement of Hadrons with the CERN AT-
2934 LAS Calorimeter”. Presented on 18 Jun 2008. PhD thesis. Vienna: Vienna,
2935 Tech. U., 2008. URL: <http://cds.cern.ch/record/1112036>.
- 2936 [36] CMS Collaboration. “The CMS barrel calorimeter response to particle
2937 beams from 2 to 350 GeV/c”. In: *Eur. Phys. J. C* 60.3 (2009). doi: [10.1140/epjc/s10052-009-0959-5](https://doi.org/10.1140/epjc/s10052-009-0959-5).
- 2939 [37] J. Beringer et al. (Particle Data Group). “Review of Particle Physics”. In:
2940 *Chin. Phys. C* 38 (2014), p. 090001. URL: <http://pdg.lbl.gov>.
- 2941 [38] P. Adragna et al. “Measurement of Pion and Proton Response and Lon-
2942 gitudinal Shower Profiles up to 20 Nuclear Interaction Lengths with the
2943 ATLAS Tile Calorimeter”. In: *Nucl. Instrum. Meth. A* 615 (2010), pp. 158–
2944 181. doi: [10.1016/j.nima.2010.01.037](https://doi.org/10.1016/j.nima.2010.01.037).
- 2945 [39] ATLAS Collaboration. “Jet energy measurement and its systematic uncer-
2946 tainty in proton–proton collisions at $\sqrt{s} = 7$ TeV with the ATLAS detec-
2947 tor”. In: *Eur. Phys. J. C* 75 (2015), p. 17. doi: [10.1140/epjc/s10052-014-3190-y](https://doi.org/10.1140/epjc/s10052-014-3190-y). arXiv: [1406.0076](https://arxiv.org/abs/1406.0076) [hep-ex]. PERF-2012-01.
- 2949 [40] Hung-Liang Lai, Marco Guzzi, Joey Huston, Zhao Li, Pavel M. Nadolsky,
2950 et al. “New parton distributions for collider physics”. In: *Phys. Rev. D* 82
2951 (2010), p. 074024. doi: [10.1103/PhysRevD.82.074024](https://doi.org/10.1103/PhysRevD.82.074024). arXiv: [1007.2241](https://arxiv.org/abs/1007.2241) [hep-ph].

- 2953 [41] E. Abat et al. “Study of energy response and resolution of the ATLAS barrel
 2954 calorimeter to hadrons of energies from 20 to 350 GeV”. In: *Nucl. Instrum.*
 2955 *Meth. A* 621.1-3 (2010), pp. 134 – 150. doi: <http://dx.doi.org/10.1016/j.nima.2010.04.054>.
- 2957 [42] ATLAS Collaboration. “Jet energy measurement with the ATLAS detector
 2958 in proton–proton collisions at $\sqrt{s} = 7$ TeV”. In: *Eur. Phys. J. C* 73 (2013),
 2959 p. 2304. doi: <10.1140/epjc/s10052-013-2304-2>. arXiv: [1112.6426 \[hep-ex\]](1112.6426). PERF-2011-03.
- 2961 [43] Naushen R. Shah and Carlos E. M. Wagner. “Gravitons and dark matter in
 2962 universal extra dimensions”. In: *Phys. Rev. D* 74 (2006), p. 104008. doi: <10.1103/PhysRevD.74.104008>. arXiv: [hep-ph/0608140 \[hep-ph\]](hep-ph/0608140).
- 2964 [44] Jonathan L. Feng, Arvind Rajaraman, and Fumihiro Takayama. “Graviton
 2965 cosmology in universal extra dimensions”. In: *Phys. Rev. D* 68 (2003), p. 085018.
 2966 doi: <10.1103/PhysRevD.68.085018>. arXiv: [hep-ph/0307375 \[hep-ph\]](hep-ph/0307375).
- 2968 [45] Paul H. Frampton and Pham Quang Hung. “Long-lived quarks?” In: *Phys.*
 2969 *Rev. D* 58 (5 1998), p. 057704. doi: <10.1103/PhysRevD.58.057704>.
 2970 URL: <http://link.aps.org/doi/10.1103/PhysRevD.58.057704>.
- 2972 [46] C. Friberg, E. Norrbin, and T. Sjostrand. “QCD aspects of leptoquark pro-
 2973 duction at HERA”. In: *Phys. Lett. B* 403 (1997), pp. 329–334. doi: [10.1016/S0370-2693\(97\)00543-1](10.1016/S0370-2693(97)00543-1). arXiv: [hep-ph/9704214 \[hep-ph\]](hep-ph/9704214).
- 2975 [47] Herbert K. Dreiner. “An introduction to explicit R-parity violation”. In:
 2976 (1997). arXiv: <hep-ph/9707435>.
- 2977 [48] Edmond L. Berger and Zack Sullivan. “Lower limits on R-parity-violating
 2978 couplings in supersymmetry”. In: *Phys. Rev. Lett.* 92 (2004), p. 201801. doi:
 2979 <10.1103/PhysRevLett.92.201801>. arXiv: <hep-ph/0310001>.
- 2980 [49] R. Barbieri, C. Berat, M. Besancon, M. Chemtob, A. Deandrea, et al. “R-
 2981 parity violating supersymmetry”. In: *Phys. Rept.* 420 (2005), p. 1. doi: <10.1016/j.physrep.2005.08.006>. arXiv: <hep-ph/0406039>.
- 2983 [50] M. Fairbairn et al. “Stable massive particles at colliders”. In: *Phys. Rept.* 438
 2984 (2007), p. 1. doi: <10.1016/j.physrep.2006.10.002>. arXiv: <hep-ph/0611040>.
- 2986 [51] Christopher F. Kolda. “Gauge-mediated supersymmetry breaking: Intro-
 2987 duction, review and update”. In: *Nucl. Phys. Proc. Suppl.* 62 (1998), p. 266.
 2988 doi: [10.1016/S0920-5632\(97\)00667-1](10.1016/S0920-5632(97)00667-1). arXiv: <hep-ph/9707450>.
- 2989 [52] Howard Baer, Kingman Cheung, and John F. Gunion. “A Heavy gluino as
 2990 the lightest supersymmetric particle”. In: *Phys. Rev. D* 59 (1999), p. 075002.
 2991 doi: <10.1103/PhysRevD.59.075002>. arXiv: <hep-ph/9806361>.
- 2992 [53] S. James Gates Jr. and Oleg Lebedev. “Searching for supersymmetry in
 2993 hadrons”. In: *Phys. Lett. B* 477 (2000), p. 216. doi: [10.1016/S0370-2693\(00\)00172-6](10.1016/S0370-2693(00)00172-6). arXiv: <hep-ph/9912362>.

- 2995 [54] G. F. Giudice and A. Romanino. "Split supersymmetry". In: *Nucl. Phys. B*
 2996 699 (2004), p. 65. doi: [10.1016/j.nuclphysb.2004.11.048](https://doi.org/10.1016/j.nuclphysb.2004.11.048). arXiv:
 2997 [hep-ph/0406088](https://arxiv.org/abs/hep-ph/0406088).
- 2998 [55] N. Arkani-Hamed, S. Dimopoulos, G. F. Giudice, and A. Romanino. "As-
 2999 pects of split supersymmetry". In: *Nucl. Phys. B* 709 (2005), p. 3. doi: [10.1016/j.nuclphysb.2004.12.026](https://doi.org/10.1016/j.nuclphysb.2004.12.026). arXiv: [hep-ph/0409232](https://arxiv.org/abs/hep-ph/0409232).
- 3000 [56] Glennys R. Farrar and Pierre Fayet. "Phenomenology of the Production,
 3001 Decay, and Detection of New Hadronic States Associated with Supersym-
 3002 metry". In: *Phys. Lett.* B76 (1978), pp. 575–579. doi: [10.1016/0370-2693\(78\)90858-4](https://doi.org/10.1016/0370-2693(78)90858-4).
- 3003 [57] A. C. Kraan, J. B. Hansen, and P. Nevski. "Discovery potential of R-hadrons
 3004 with the ATLAS detector". In: *Eur. Phys. J.* C49 (2007), pp. 623–640. doi:
 3005 [10.1140/epjc/s10052-006-0162-x](https://doi.org/10.1140/epjc/s10052-006-0162-x). arXiv: [hep-ex/0511014](https://arxiv.org/abs/hep-ex/0511014)
 3006 [[hep-ex](#)].
- 3007 [58] Rasmus Mackeprang and David Milstead. "An Updated Description of
 3008 Heavy-Hadron Interactions in GEANT-4". In: *Eur. Phys. J.* C66 (2010), pp. 493–
 3009 501. doi: [10.1140/epjc/s10052-010-1262-1](https://doi.org/10.1140/epjc/s10052-010-1262-1). arXiv: [0908.1868](https://arxiv.org/abs/0908.1868)
 3010 [[hep-ph](#)].
- 3011 [59] ATLAS Collaboration. "Search for massive, long-lived particles using mul-
 3012 titrack displaced vertices or displaced lepton pairs in pp collisions at $\sqrt{s} =$
 3013 8 TeV with the ATLAS detector". In: *Phys. Rev. D* 92 (2015), p. 072004.
 3014 doi: [10.1103/PhysRevD.92.072004](https://doi.org/10.1103/PhysRevD.92.072004). arXiv: [1504.05162](https://arxiv.org/abs/1504.05162) [[hep-ex](#)].
 3015 SUSY-2014-02.
- 3016 [60] ATLAS Collaboration. "Search for charginos nearly mass degenerate with
 3017 the lightest neutralino based on a disappearing-track signature in pp col-
 3018 lisions at $\sqrt{s} = 8$ TeV with the ATLAS detector". In: *Phys. Rev. D* 88 (2013),
 3019 p. 112006. doi: [10.1103/PhysRevD.88.112006](https://doi.org/10.1103/PhysRevD.88.112006). arXiv: [1310.3675](https://arxiv.org/abs/1310.3675)
 3020 [[hep-ex](#)]. SUSY-2013-01.
- 3021 [61] ATLAS Collaboration. "Searches for heavy long-lived sleptons and R-Hadrons
 3022 with the ATLAS detector in pp collisions at $\sqrt{s} = 7$ TeV". In: *Phys. Lett. B*
 3023 720 (2013), p. 277. doi: [10.1016/j.physletb.2013.02.015](https://doi.org/10.1016/j.physletb.2013.02.015). arXiv:
 3024 [1211.1597](https://arxiv.org/abs/1211.1597) [[hep-ex](#)]. SUSY-2012-01.
- 3025 [62] ATLAS Collaboration. "Searches for heavy long-lived charged particles
 3026 with the ATLAS detector in proton–proton collisions at $\sqrt{s} = 8$ TeV".
 3027 In: *JHEP* 01 (2015), p. 068. doi: [10.1007/JHEP01\(2015\)068](https://doi.org/10.1007/JHEP01(2015)068). arXiv:
 3028 [1411.6795](https://arxiv.org/abs/1411.6795) [[hep-ex](#)]. SUSY-2013-22.
- 3029 [63] ATLAS Collaboration. "Search for metastable heavy charged particles with
 3030 large ionisation energy loss in pp collisions at $\sqrt{s} = 8$ TeV using the AT-
 3031 LAS experiment". In: *Eur. Phys. J.* C 75 (2015), p. 407. doi: [10.1140/epjc/s10052-015-3609-0](https://doi.org/10.1140/epjc/s10052-015-3609-0). arXiv: [1506.05332](https://arxiv.org/abs/1506.05332) [[hep-ex](#)]. SUSY-
 3032 2014-09.
- 3033
- 3034
- 3035

- 3036 [64] ATLAS Collaboration. “Search for heavy long-lived charged R -hadrons
 3037 with the ATLAS detector in 3.2 fb^{-1} of proton–proton collision data at
 3038 $\sqrt{s} = 13 \text{ TeV}$ ”. In: *Phys. Lett.* B760 (2016), pp. 647–665. doi: [10.1016/j.physletb.2016.07.042](https://doi.org/10.1016/j.physletb.2016.07.042). arXiv: [1606.05129](https://arxiv.org/abs/1606.05129) [hep-ex].
- 3040 [65] Torbjorn Sjöstrand, Stephen Mrenna, and Peter Skands. “PYTHIA 6.4 Physics
 3041 and Manual”. In: *JHEP* 0605 (2006), p. 026. doi: [10.1088/1126-6708/2006/05/026](https://doi.org/10.1088/1126-6708/2006/05/026). arXiv: [hep-ph/0603175](https://arxiv.org/abs/hep-ph/0603175).
- 3043 [66] *Further ATLAS tunes of PYTHIA6 and Pythia 8*. Tech. rep. ATL-PHYS-PUB-
 3044 2011-014. Geneva: CERN, 2011. url: <https://cds.cern.ch/record/1400677>.
- 3046 [67] Aafke Christine Kraan. “Interactions of heavy stable hadronizing parti-
 3047 cles”. In: *Eur. Phys. J.* C37 (2004), pp. 91–104. doi: [10.1140/epjc/s2004-01946-6](https://doi.org/10.1140/epjc/s2004-01946-6). arXiv: [hep-ex/0404001](https://arxiv.org/abs/hep-ex/0404001) [hep-ex].
- 3049 [68] M. Fairbairn et al. “Stable massive particles at colliders”. In: *Phys. Rept.* 438
 3050 (2007), p. 1. doi: [10.1016/j.physrep.2006.10.002](https://doi.org/10.1016/j.physrep.2006.10.002). arXiv: [hep-ph/0611040](https://arxiv.org/abs/hep-ph/0611040).
- 3052 [69] W. Beenakker, R. Hopker, M. Spira, and P. M. Zerwas. “Squark and gluino
 3053 production at hadron colliders”. In: *Nucl. Phys. B* 492 (1997), p. 51. doi:
 3054 [10.1016/S0550-3213\(97\)00084-9](https://doi.org/10.1016/S0550-3213(97)00084-9). arXiv: [hep-ph/9610490](https://arxiv.org/abs/hep-ph/9610490).
- 3055 [70] A. Kulesza and L. Motyka. “Threshold resummation for squark-antisquark
 3056 and gluino-pair production at the LHC”. In: *Phys. Rev. Lett.* 102 (2009),
 3057 p. 111802. doi: [10.1103/PhysRevLett.102.111802](https://doi.org/10.1103/PhysRevLett.102.111802). arXiv: [0807.2405](https://arxiv.org/abs/0807.2405) [hep-ph].
- 3059 [71] A. Kulesza and L. Motyka. “Soft gluon resummation for the production
 3060 of gluino-gluino and squark-antisquark pairs at the LHC”. In: *Phys. Rev.*
 3061 D 80 (2009), p. 095004. doi: [10.1103/PhysRevD.80.095004](https://doi.org/10.1103/PhysRevD.80.095004). arXiv:
 3062 [0905.4749](https://arxiv.org/abs/0905.4749) [hep-ph].
- 3063 [72] Wim Beenakker, Silja Brening, Michael Kramer, Anna Kulesza, Eric Lae-
 3064 nen, et al. “Soft-gluon resummation for squark and gluino hadroprodu-
 3065 tion”. In: *JHEP* 0912 (2009), p. 041. doi: [10.1088/1126-6708/2009/12/041](https://doi.org/10.1088/1126-6708/2009/12/041). arXiv: [0909.4418](https://arxiv.org/abs/0909.4418) [hep-ph].
- 3067 [73] W. Beenakker, S. Brening, M.n Kramer, A. Kulesza, E. Laenen, et al. “Squark
 3068 and Gluino Hadroproduction”. In: *Int. J. Mod. Phys. A* 26 (2011), p. 2637.
 3069 doi: [10.1142/S0217751X11053560](https://doi.org/10.1142/S0217751X11053560). arXiv: [1105.1110](https://arxiv.org/abs/1105.1110) [hep-ph].
- 3070 [74] Michael Krämer et al. *Supersymmetry production cross sections in pp collisions*
 3071 at $\sqrt{s} = 7 \text{ TeV}$. 2012. arXiv: [1206.2892](https://arxiv.org/abs/1206.2892) [hep-ph].
- 3072 [75] Rasmus Mackeprang and Andrea Rizzi. “Interactions of Coloured Heavy
 3073 Stable Particles in Matter”. In: *Eur. Phys. J.* C50 (2007), pp. 353–362. doi:
 3074 [10.1140/epjc/s10052-007-0252-4](https://doi.org/10.1140/epjc/s10052-007-0252-4). arXiv: [hep-ph/0612161](https://arxiv.org/abs/hep-ph/0612161)
 3075 [hep-ph].

- 3076 [76] Rasmus Mackeprang and David Milstead. “An Updated Description of
3077 Heavy-Hadron Interactions in GEANT-4”. In: *Eur. Phys. J.* C66 (2010), pp. 493–
3078 501. doi: [10.1140/epjc/s10052-010-1262-1](https://doi.org/10.1140/epjc/s10052-010-1262-1). arXiv: [0908.1868](https://arxiv.org/abs/0908.1868)
3079 [[hep-ph](#)].
- 3080 [77] J. Alwall, R. Frederix, S. Frixione, V. Hirschi, F. Maltoni, O. Mattelaer, H. S.
3081 Shao, T. Stelzer, P. Torrielli, and M. Zaro. “The automated computation of
3082 tree-level and next-to-leading order differential cross sections, and their
3083 matching to parton shower simulations”. In: *JHEP* 07 (2014), p. 079. doi:
3084 [10.1007/JHEP07\(2014\)079](https://doi.org/10.1007/JHEP07(2014)079). arXiv: [1405.0301](https://arxiv.org/abs/1405.0301) [[hep-ph](#)].
- 3085 [78] “dE/dx measurement in the ATLAS Pixel Detector and its use for particle
3086 identification”. In: (2011).
- 3087 [79] ATLAS Collaboration. “The ATLAS Simulation Infrastructure”. In: *Eur.*
3088 *Phys. J.* C70 (2010), pp. 823–874. doi: [10.1140/epjc/s10052-010-1429-9](https://doi.org/10.1140/epjc/s10052-010-1429-9). arXiv: [1005.4568](https://arxiv.org/abs/1005.4568) [[physics.ins-det](#)].
- 3090 [80] Alexander L. Read. “Presentation of search results: The CL(s) technique”.
3091 In: *J. Phys.* G28 (2002). [,11(2002)], pp. 2693–2704. doi: [10.1088/0954-3899/28/10/313](https://doi.org/10.1088/0954-3899/28/10/313).
- 3092

3093 DECLARATION

3094 Put your declaration here.

3095 *Berkeley, CA, September 2016*

3096

Bradley Axen

3097

3098 COLOPHON

3099

Not sure that this is necessary.